

**Structure changes of $\text{Ce}_{1-x}\text{Ln}_x\text{O}_{2-\delta}$ (Ln = La, Gd) and
 $\text{Ba}_{1-x}\text{Zr}_{1-y}\text{Y}_y\text{O}_{3-\delta}$ solid electrolytes**
(La 及び Gd ドープ酸化セリウム及び Y ドープジルコニウム酸バリウムの構造変化)

March, 2020

Author: LIU XUE

Abstract

As entering in the 21st century, energy and the environment issues are putting more and more pressure on human beings, and the call for improving the living environment of human beings is getting higher and higher. As a new, efficient and clean energy source, fuel cell power generation technology has attracted widespread attention of the world.

Minimum assembly of fuel cells are composed of three major parts; a cathode, an anode and an electrolyte. Air is supplied to the cathode and fuel is supplied to the anode (in this case H_2) which is oxidized releasing electrons. Electrons pass through to the cathode where they reduce the oxygen at the electrode/electrolyte interface. According to the different types of electrolytes, the fuel cells can be divided into five categories: alkaline fuel cells (AFC), phosphoric acid fuel cells (PAFCs), molten carbonate fuel cells (MCFC), solid oxide fuel cell (SOFC), and proton exchange membrane fuel cell (PEM FC). Among them, high-temperature solid oxide fuel cells (SOFC) have all-solid structure and higher energy. The outstanding characteristics such as efficiency, and wide adaptability to various fuel gases such as gas, natural gas and mixed gas are the fastest, and the above characteristics are also the basis for its wide applications.

According to a previous report, the electrical conductivity is related with the calcined temperature. Otherwise, the electrical conductivity of $Ce_{1-x}La_xO_{2-\delta}$ (LDC) shows a specific behavior at $x = 0.3$. Thus, we suspect that a local structural change also occurred in our target materials. $BaCeO_3$ has low chemical stability under CO_2 and H_2O atmospheres. In contrast, $BaZrO_3$ has excellent chemical stability. However, high sintering temperature and long sintering duration are required to obtain a high density $BaZrO_3$ material. Therefore, in order to obtain the sample with high density, a sintering aid ZnO would be required.

In the first part of work, we synthesized the $Ce_{1-x}La_xO_{2-\delta}$ ($x=0.1-0.5$) samples with the co-precipitation method. We researched about the starting conditions as the ratios between metal ion

and precipitating reagent were 1:20, 1:15 and 1:5, respectively. We could conclude from the measurement results that the particle size of the calcined particles was related with the starting material concentration and the best condition was 1:15 about the ratio of metal ion and precipitating reagent. Then we synthesized the $Ce_{1-x}La_xO_{2-\delta}$ ($x = 0.1-0.5$) samples under this condition. When we calculated the lattice parameters of each sample, the experimental data curve was not fit with the theoretical one. From this, we suspected that there was a structure change occurred in $Ce_{1-x}La_xO_{2-\delta}$ ($x = 0.1-0.5$) samples.

In the second part of work, the changes in local structures of $Ce_{1-x}Ln_xO_{2-\delta}$ with Ln (La, Gd) doping were investigated. XAFS was successfully used to clarify the coordination environments around Ce and the dopant La and Gd. For LDC, La coordination was maintained at 7, and Ce coordination decreased from 8 to 6 on average. It was speculated that a superstructure would be formed which was more like a pyrochlore structure in LDC at $x > 0.3$. For GDC, the coordination numbers for Gd and Ce decreased from 8 to 6 on average. And oxygen vacancies had no preference for Ce or Gd coordination. We also combined XRD results and EXAFS results together. These results explained the changes in the lattice parameters for both LDC and GDC. The local structure change model was designed and the electric conductivity changing at each stage of Ln (La, Gd) doping was explained. In future studies, these results could be applied to other materials.

In the third part of work, we synthesized the $Ba_{1-x}Zr_{1-y}Y_yO_{3-\delta}$ ($x = 0.02, 0.04$) and ($y = 0.1, 0.2, 0.3$) samples successfully and research about the experiment conditions with XRD measurement. It was confirmed that the $Ba_{0.96}Zr_{0.9}Y_{0.1}O_{3-\delta}$ was the best condition. Then we added the ZnO as the sintering aid to obtain the $Ba_{0.96}Zr_{0.9}Y_{0.1}O_{3-\delta} + ZnO$ (0-3wt%) samples sintered at 1500 °C for 5h. As a result, the relative density could reach to 99.6% of $Ba_{0.96}Zr_{0.9}Y_{0.1}O_{3-\delta} + ZnO$ 3wt%. And the electrical conductivity of $Ba_{0.96}Zr_{0.9}Y_{0.1}O_{3-\delta} + ZnO$ 1wt% sample was the highest. It was considered that the perovskite structure was destroyed so that the grain boundary resistance increased. Then we researched to prevent BaO pellet sublimation and surface decomposition with powder bed method. It was thought that ZnO was amorphous or existed between lattices. From EDS result, it was found that Y precipitation on the pellet surface could be suppressed by the PB

method. It is hoped that powder bed method could prevent the BaO pellet sublimation and surface decomposition in the future work.

Content

Chapter 1 Introduction	8
1.1 The brief history of Fuel Cells	8
1.2 The working mechanism of fuel cells	9
1.3 Classification.....	11
1.4 The advantage of fuel cells.....	13
1.5 Solid Oxide Fuel Cells (SOFC).....	15
1.6 The working mechanism and advantages of SOFC	16
1.7 The applications of SOFC.....	19
1.8 The materials of SOFC.....	22
1.9 Research aims.....	31
Reference.....	33
Chapter 2 Preparation and characterization of $\text{Ce}_{1-x}\text{La}_x\text{O}_{2-\delta}$ powder and sintered samples.....	39
2.1. Overview of the preparation method.....	39
2.2 Experiment	41
2.3 Synthesis of high density sintered compact of $\text{Ce}_{0.9}\text{La}_{0.1}\text{O}_{2-\delta}$	42
2.4 Conclusion.....	50
Reference.....	51
Chapter 3: Local structure changes of $\text{Ce}_{1-x}\text{Ln}_x\text{O}_{2-\delta}$ (Ln = La, Gd) solid electrolytes.....	53
3.1 Introduction	53
3.2 XAFS measurement and analysis.....	55
3.3 Results and discussion.....	58
3.4 Conclusion.....	70

Reference.....	71
Chapter 4: Structure changes of $Ba_{1-x}Zr_{1-y}Y_yO_{3-\delta}$ electrolyte materials	73
4.1 Introduction	73
4.2 Experiment	75
4.3 Results and discussions	76
4.3 Conclusion.....	89
Reference.....	90
Chapter 5. Summary	92
Acknowledgement	94
Publications.....	96

Chapter 1 Introduction

Energy is the foundation of socio-economic development. There would be no modern civilization without the development of the energy industry. The rapid progress of science and technology, coupled with the development of the global economy, social progress and rapid population growth, have resulted in an increasing demand for energy in the past hundred years. As entering in the 21st century, energy and the environment issues are putting more and more pressure on human beings. The call is getting higher and higher for improving the living environment of human beings as soon as possible. Nowadays we have been making unremitting efforts to use energy more efficiently. It has become to the goals pursued for sustainable use and development of new energy technologies which are environmentally friendly and efficient in energy conversion by the industrial and academic communities of all the countries. Among the development of new energy technologies, fuel cells technology has become the most attractive new energy supply technology in recent years. It has attracted much attention by its excellent properties, such as low pollution, low noise, high conversion efficiency, long-life and wide application range. As a new, efficient and clean energy source, fuel cell power generation technology has been widespread hot topic of the world.

1.1 The brief history of Fuel Cells

Fuel cells, which were first discovered in 1838 by William Grove, were referred to as wet cell battery or Grove cell^[1]. They were operated using the concept of reverse electrolysis of water. 100 years later, British engineer Francis Thomas Bacon developed a practical 5kW fuel cell in 1939. In 1955, General Electric chemist Thomas Grubb T. (Thomas Grubb) from USA, made an ion exchange membrane which was used as an electrolyte in fuel cells. Proton exchange membrane fuel cells were used in NASA's Gemini project V (Gemini) manned spaceflight neutral fuel cells in 1965, the life and performance of the fuel cell are greatly improved. In the mid-1970s, phosphoric acid fuel cells began to be installed and used commercially. Since the late 1980s, the

application of proton exchange membrane fuel cells has attracted attention in the automotive field. In the early 1990s, several automotive companies have successively introduced fuel cell prototypes. In 2011, Mercedes-Benz B-class fuel cell cars completed the world journey^[2].

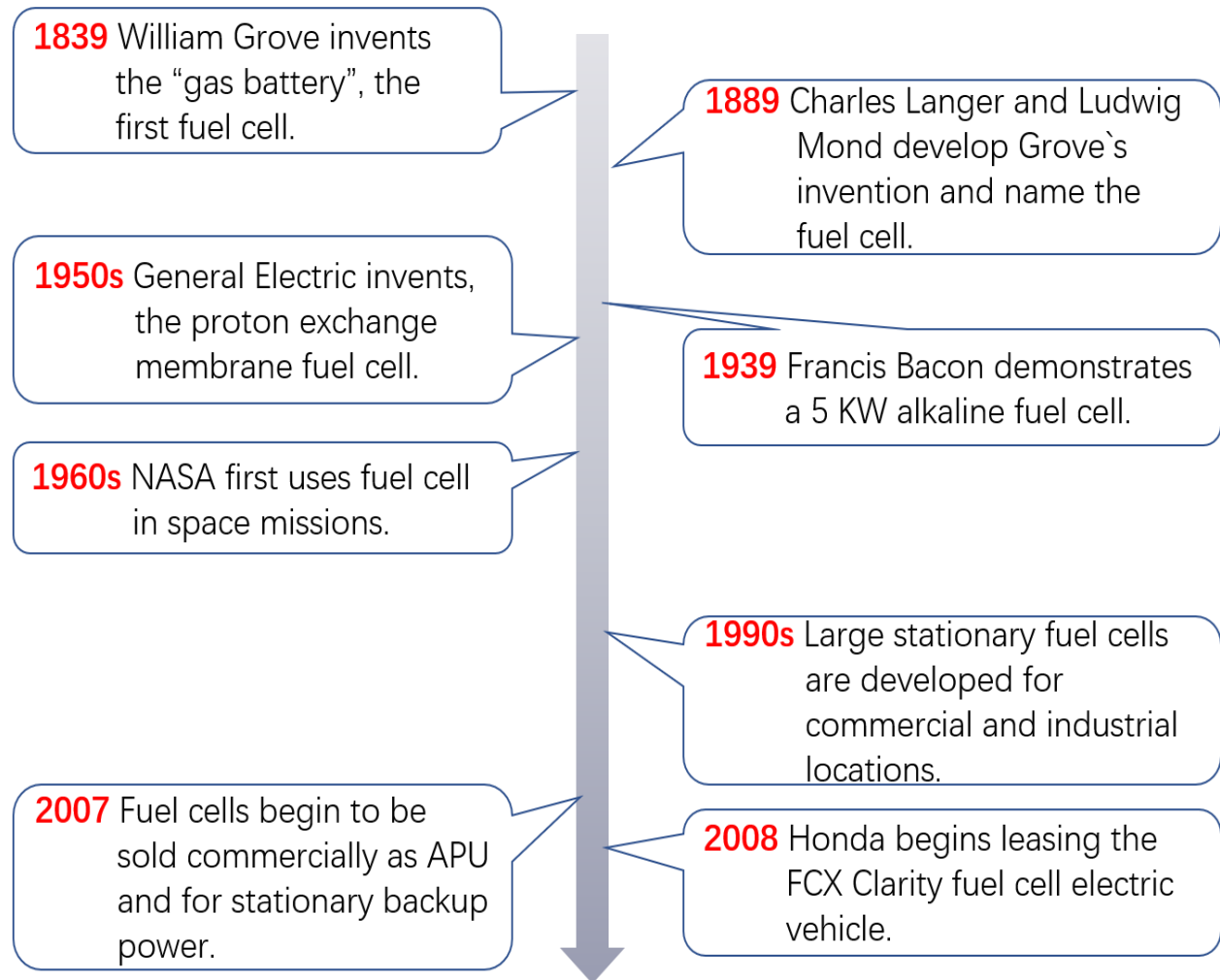


Figure 1.1 The brief history of Fuel Cells.

1.2 The working mechanism of fuel cells

Fuel cell is a kind of energy conversion device. It is based on the principle of electrochemistry which is the principle of primary battery. It converts the chemical energy stored in fuel and oxidant into electrical energy directly, so the actual process is redox reaction. Fuel cell is mainly composed of four parts, namely anode, cathode, electrolyte and external circuit. Fuel gas and oxidant gas are

introduced from the anode and cathode of the fuel cell, respectively. The fuel gas emits electrons on the anode, and the electrons are conducted to the cathode through an external circuit and combined with the oxidizing gas to generate ions. Under the action of an electric field, ions migrate to the anode through the electrolyte, react with the fuel gas. At there, they form a loop, and generate electric current. At the same time, the fuel cell also generates a certain amount of heat due to its own electrochemical reaction and the internal resistance of the battery. In addition to conducting electrons, the cathode and anode of the battery also act as catalysts for the redox reaction. When the fuel is a hydrocarbon, the anode requires higher catalytic activity. The cathodes and anodes are usually porous to facilitate the introduction of reaction gases and the discharge of products. The electrolyte plays a role of transferring ions and separating fuel gas and oxidizing gas. In order to prevent the short circuit in the battery caused by the mixture of two gases, the electrolyte is usually a dense structure^[3-8].

The principle of a fuel cell is an electrochemical device with the same composition as a general battery. Its single cell is composed of two electrodes (a negative electrode is a fuel electrode and a positive electrode is an oxidant electrode) and an electrolyte. The difference is that the active material of a general battery is stored inside the battery, thus limiting the battery capacity. The positive and negative electrodes of a fuel cell do not contain active materials, but are only catalytic conversion elements. Therefore, fuel cells are truly energy conversion machines that convert chemical energy into electrical energy. When the battery is operating, fuel and oxidant are supplied from the outside and react. In principle, as long as the reactants are continuously input and the reaction products are continuously eliminated, the fuel cell can continuously generate electricity.

A fuel cell is generally composed of an electrolyte plate forming an ion conductor, a fuel electrode (anode) and an air electrode (cathode) arranged on both sides, and a gas flow path on both sides. The gas flow path is used to make fuel gas and air (oxidant). Gas can pass through the flow path. In the fuel electrode, H_2 in the supplied fuel gas is decomposed into H^+ and e^- , and H^+ moves to the electrolyte to react with O_2 supplied from the air electrode. e^- Via the external load circuit, return to the air pole side and participate in the reaction of the air pole side. The response of a

series of cases led to e^- through uninterrupted passage through the external circuit, thus constituting power generation.

1.3 Classification

There are many types of fuel cells classification. According to the working temperature, it can be divided into low temperature, medium temperature and high temperature generally. The operating temperature is between room temperature and 500 °C, which is called low temperature fuel cell; the operating temperature is between 500 and 800 °C, which is called medium temperature fuel cell; the operating temperature is above of 800 °C, which is called high temperature fuel cell. According to the different types of electrolytes, the fuel cells can be divided into five categories: alkaline fuel cells (AFC), phosphoric acid fuel cells (PAFCs), and molten carbonate fuel cells (MCFC), solid oxide fuel cell (SOFC), proton exchange membrane fuel cell (PEMFC).

(1) Alkaline fuel cells (AFC)^[9,10]

The alkaline fuel cell (AFC), also known as the Bacon fuel cell after its British inventor, Francis Thomas Bacon, is one of the most developed fuel cell technologies. Alkaline fuel cells must be operated at a low temperature of 80 °C, with fast start-up, high efficiency and high power density, and do not require precious platinum. They are among the most efficient fuel cells, having the potential to reach 70%. The two electrodes are separated by a porous matrix saturated with an aqueous alkaline solution, such as potassium hydroxide (KOH). Aqueous alkaline solutions do not reject carbon dioxide (CO_2) so the fuel cell can become "poisoned" through the conversion of KOH to potassium carbonate (K_2CO_3). Although this type of fuel cell has developed early, it is limited to pure hydrogen and pure oxygen as raw materials and is used in special places such as space shuttles and submarines.

(2) Phosphoric acid fuel cells (PAFCs)^[11-14]

Phosphoric acid fuel cells are currently the fastest growing fuel cell in the market. They have many advantages such as simple structure, stability, low electrolyte volatility. Carbonated fuel cell devices range in capacity from 1kW to 1100kW. The operating temperature is around 200 degrees. To improve electrode reactivity, platinum must be used as a catalyst. Phosphoric acid batteries have a heat rejection temperature of 60 to 190 °C, which can be recycled for air conditioning or hot water use. It is very suitable for combined heat and power systems.

(3) Molten carbonate fuel cells (MCFC)^[15-18]

Molten carbonic acid fuel cells use alkali metal (lithium, potassium, sodium) carbonate as the electrolyte. Therefore, the alkali metal carbonate can only exert ion conduction function in the molten state. So the operating temperature needs to be above the melting point, between 550 and 700 degrees. It is a medium temperature fuel cell. After the carbon dioxide is recovered by the anode, it can be recycled to the cathode for use. Since the molten carbonic acid fuel cell is easy to react, no precious metal is required as a catalyst, and nickel and nickel oxide can be used as the electrode material.

(4) Solid oxide fuel cells (SOFC)^[19-21]

For solid oxide fuel cells, the electrolyte is a solid, non-porous metal oxide. Ions are transported by the oxygen ions shuttle through the crystal. Stable zirconia is usually used as the electrolyte. Due to the high operating temperature, the battery body material is limited to ceramics or metal oxides.

(5) Proton exchange membrane fuel cell (PEMFC)^[22-24]

Proton exchange membrane fuel cells use a cation exchange membrane as the electrolyte. Because of its excellent chemical stability, it can reduce the problems of electrolyte dilution and atomization. It is also an ideal material for fixed and mobile devices.

The five fuel cells are each at different stages of development. Among them, the research and development of SOFC is still in its infancy and has not yet been commercialized. The main

problem with SOFC is the higher manufacturing cost. At the same time, the high temperature required for the reaction brings many technical difficulties. With the development of SOFC materials and assembly technologies in recent years, once the cost problem is solved, SOFC is very promising to become a new technology for centralized or decentralized power generation in the future. Figure 1.2 shows the classification of fuel cells.

Fuel Cell Type	Common Electrolyte	Operating Temperature	Typical Stack Size	Efficiency	Applications	Advantages	Disadvantages
Polymer Electrolyte Membrane (PEM)	Perfluoro sulfonic acid	50-100°C 122-212° typically 80°C	< 1kW-100kW	60% transportation 35% stationary	<ul style="list-style-type: none"> Backup power Portable power Distributed generation Transportation Specialty vehicles 	<ul style="list-style-type: none"> Solid electrolyte reduces corrosion & electrolyte management problems Low temperature Quick start-up 	<ul style="list-style-type: none"> Expensive catalysts Sensitive to fuel impurities Low temperature waste heat
Alkaline (AFC)	Aqueous solution of potassium hydroxide soaked in a matrix	90-100°C 194-212°F	10-100 kW	60%	<ul style="list-style-type: none"> Military Space 	<ul style="list-style-type: none"> Cathode reaction faster in alkaline electrolyte, leads to high performance Low cost components 	<ul style="list-style-type: none"> Sensitive to CO₂ in fuel and air Electrolyte management
Phosphoric Acid (PAFC)	Phosphoric acid soaked in a matrix	150-200°C 302-392°F	400 kW 100 kW module	40%	<ul style="list-style-type: none"> Distributed generation 	<ul style="list-style-type: none"> Higher temperature enables CHP Increased tolerance to fuel impurities 	<ul style="list-style-type: none"> Pt catalyst Long start up time Low current and power
Molten Carbonate (MCFC)	Solution of lithium, sodium, and/or potassium carbonates, soaked in a matrix	600-700°C 1112-1292°F	300 kW-3 MW 300 kW module	45-50%	<ul style="list-style-type: none"> Electric utility Distributed generation 	<ul style="list-style-type: none"> High efficiency Fuel flexibility Can use a variety of catalysts Suitable for CHP 	<ul style="list-style-type: none"> High temperature corrosion and breakdown of cell components Long start up time Low power density
Solid Oxide (SOFC)	Yttria stabilized zirconia	700-1000°C 1202-1832°F	1 kW-2 MW	60%	<ul style="list-style-type: none"> Auxiliary power Electric utility Distributed generation 	<ul style="list-style-type: none"> High efficiency Fuel flexibility Can use a variety of catalysts Solid electrolyte Suitable for CHP & CHHP Hybrid/GT cycle 	<ul style="list-style-type: none"> High temperature corrosion and breakdown of cell components High temperature operation requires long start up time and limits

Figure 1.2 The brief introduction of different types of fuel cells^[15].

1.4 The advantage of fuel cells

A fuel cell is a device that directly converts the chemical energy of a fuel into electrical energy. In theory, as long as the fuel is continuously supplied, the fuel cell can continuously generate electricity, which has been hailed as the fourth generation power generation technology after hydropower, thermal power, and nuclear power^[25-27].

(1) High power generation efficiency

Fuel cell power generation is not limited by the Carnot cycle. Theoretically, its power generation efficiency can reach 85% to 90%, but due to the limitations of various polarizations at work, the

current energy conversion efficiency of fuel cells is about 40% to 60%. If combined heat and power is realized, the total fuel utilization rate can reach over 80%.

(2) Low environmental pollution

When a fuel cell uses hydrogen-rich gas such as natural gas as a fuel, carbon dioxide emissions are reduced by more than 40% compared to the heat engine process, which is very important to alleviate the greenhouse effect of the planet. In addition, because the fuel gas of the fuel cell must be desulfurized before the reaction, and the electricity is generated according to the electrochemical principle, there is no high temperature combustion process, so almost no nitrogen and sulfur oxides are emitted, which reduces the pollution to the atmosphere.

(3) High specific energy

The specific energy of a liquid hydrogen fuel cell is 800 times that of a nickel-cadmium battery, and the specific energy of a direct methanol fuel cell is more than 10 times higher than that of a lithium ion battery (a rechargeable battery with the highest energy density). At present, although the actual specific energy of a fuel cell is only 10% of the theoretical value, it is still much higher than the actual specific energy of a general battery.

(4) Low noise

The fuel cell has a simple structure, few moving parts, and low noise during operation. Even near an 11MW-class fuel cell power plant, the measured noise was less than 55dB.

(5) Wide fuel range

For fuel cells, as long as substances containing hydrogen atoms can be used as fuel, such as natural gas, petroleum, coal and other fossil products, or biogas, alcohol, methanol, etc., fuel cells are very suitable for the needs of energy diversification and can slow down the mainstream depletion of energy.

(6) High reliability

When the load of the fuel cell changes, it will respond quickly. Whether it is above the rated power overload operation or below the rated power operation, it can still work and the efficiency changes little. Due to the highly reliable operation of the fuel cell, it can be used as various emergency

power sources and uninterruptible power sources.

(7) Easy to be founded

The fuel cell has an assembled structure, which is convenient to install and maintain, and does not require many auxiliary facilities. The design and manufacture of fuel cell power plants is quite convenient.

1.5 Solid Oxide Fuel Cells (SOFC)

In nowadays society, hydrogen energy has gradually gained attention as an effective energy solution in the future. As an important technical support in the field of hydrogen energy, hydrogen fuel cells have experienced the first-generation phosphoric acid fuel cell (PAFC), and the second-generation molten carbonate fuel cell (MCFC) has developed to a third-generation solid with an operating temperature of 500 to 1,000 °C. It is the fuel cell system with the highest energy conversion efficiency after PAFC and MCFC. Especially as a distributed power station, it has attracted widespread interest from scientists in various countries. SOFC is an all-solid-state energy conversion device that uses fuel and oxidant gas to generate electricity through an ion-conducting ceramic. So it is also called ceramic fuel cell.

Compared with traditional power generation methods, SOFC has no combustion process and mechanical movement. It reduces the energy loss of fossil fuels greatly during energy conversion and the damage to the ecological environment. Therefore, it has the characteristics of stable operation, high efficiency (40% -85%), zero pollution, and no noise. The output voltage(V) under load conditions, that is, when a current is passes through the cell is given by Ref.^[28].

$$V = E^{\circ} - IR - \eta_c - \eta_a \quad (1)$$

where, I is the current passing through the cell, E° is the open circuit potential of the cell, R is the cell's electrical resistance, η_c and η_a are the polarization losses associated with the cathode and anode respectively.

Compared with PEMFC, SOFC has a very high energy conversion efficiency and avoids the limitations (such as Pt) that can only use precious metal electrode materials. Eliminates the

poisoning of the CO to the electrode, reduces the fuel requirements, and enriches the types of optional fuels (such as natural gas, gas, etc.). Compared with MCFC, SOFC has no liquid molten salt corrosion medium, which avoids thermal corrosion of fuel cells. Therefore, SOFC has gradually become one of the hotspots in research and application.

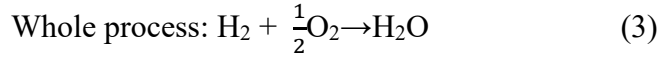
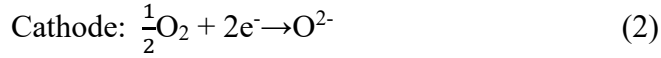
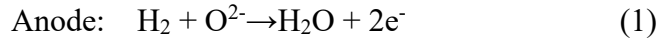
1.6 The working mechanism and advantages of SOFC

SOFC is made up of porous cathode, dense electrolyte and a porous anode. The electrodes must have the property of porous, for passing through of the fuel gas and oxidant (air, oxygen, etc.) during the operation. The SOFC can be divided into two types by their ion carriers: one is oxygen ion conducting (O-SOFC), while the other is hydrogen ion conducting (H-SOFC), which is also decided the types of electrolytes used. The electrolyte must have the properties as a dense structure, low electronic conductivity, high ionic conductivity, excellent chemical stability with the fuel and oxidant, a non-reaction with the electrode materials, and a small mismatch of the thermal expansion coefficient with the electrodes^[4]. Fig. 1.2(a) and (b) show the schemes of O-SOFC and H-SOFC. In O-SOFC, it follows the Equation (1): the oxygen is reduced to oxygen carriers at the cathode electrolyte interface. The oxygen carriers can then be transported through an oxide-ion-conducting electrolyte to the anode interface using an oxygen vacancy compensation mechanism. At the anode side, they can react with the fuel gas to create water, heat and CO₂ or other emissions, as Equation (2). The whole conduction process is represented by Equation (3). In the whole process, in case of fuel is hydrogen, then only water is generated as waste production which is environmentally friendly. Even if other type of fuel, CO₂ would be created, but the CO₂ emission per KWh is less compare to other power generating facilities.

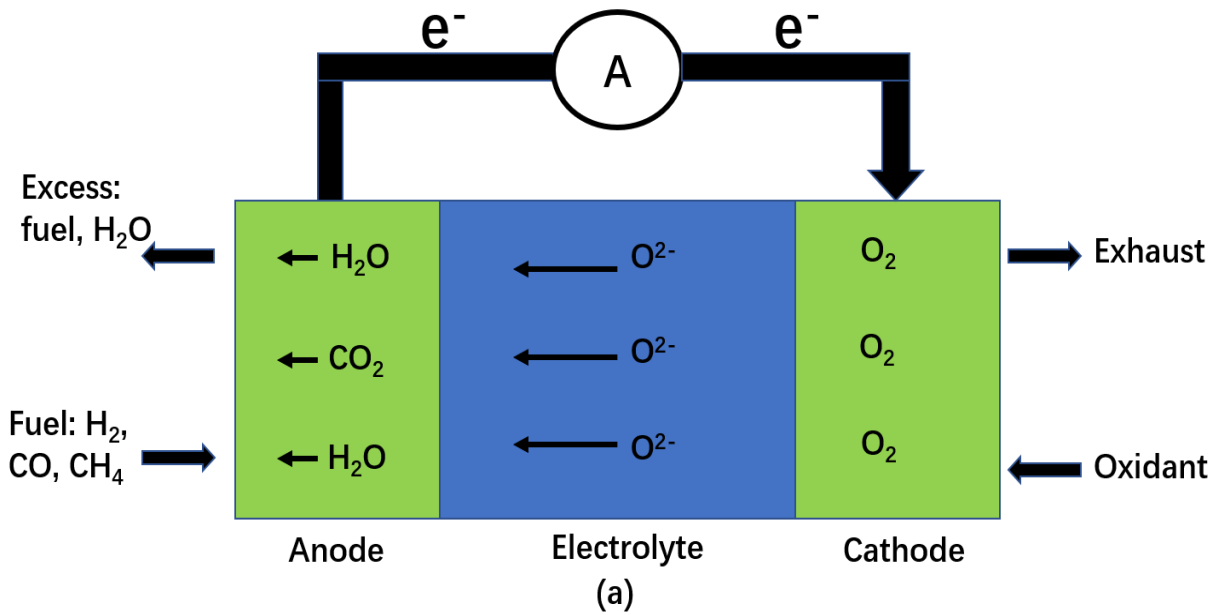
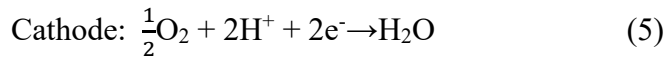
While in H-SOFC, the hydrogen carriers are produced at the anode side follow the Equation (4). The hydrogen carriers can then be transported through an hydrogen-ion-conducting electrolyte to the anode interface using an oxygen vacancy compensation mechanism. At the anode side, they combine with the oxygen ions to produce water (Equation (5)). The whole process is the same as

that of the O-SOFC by Equation (3). The production at the cathodic side, which is only water, can avoid the pollution of fuel burning.

For O^{2-} conduction:



For H^+ conduction:



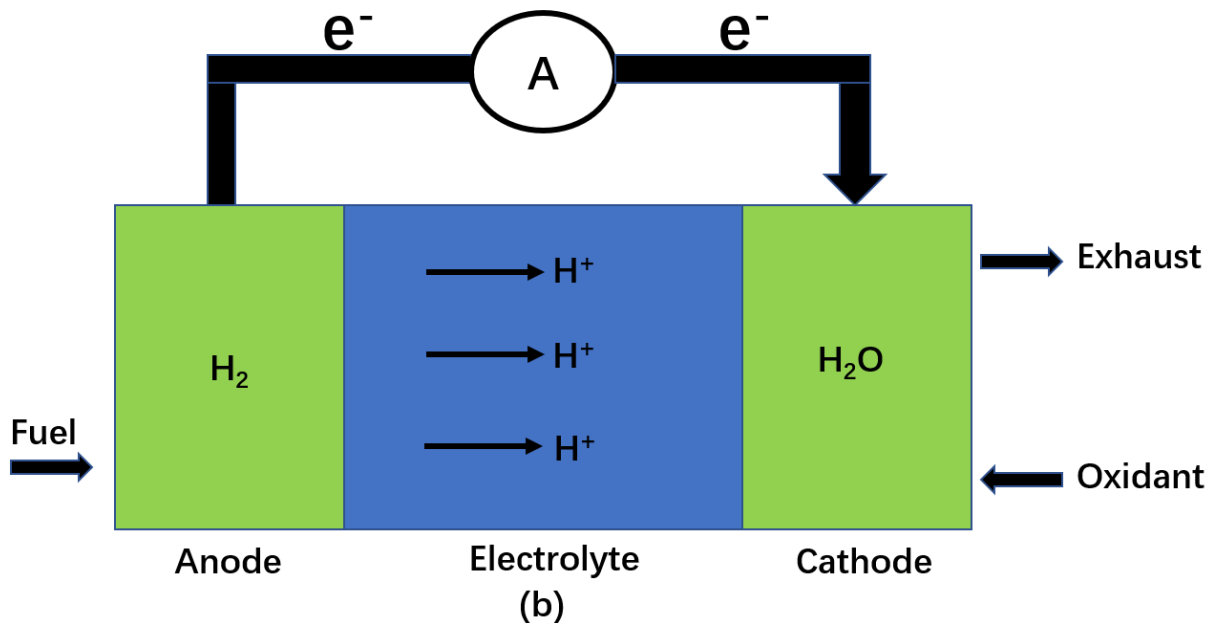


Figure 1.3 The schemes of two SOFC types: (a) O^{2-} carriers (O-SOFC) and (b) H^+ carriers (H-SOFC), respectively.

SOFC does not have combustion and mechanical processes for energy conversion, thereby greatly improving energy conversion efficiency and avoiding the generation of NO_x , SO_x , CO, CO_2 and dust and other pollutants. It is quiet and has a good guarantee for the quality of the power. The operating temperature of SOFC is usually in the range of 500 to 1000 °C, and its by-products are heat and water vapor. Therefore, while supplying electricity, SOFC can also provide hot water and heating.

Compared with PAFC and MCFC, SOFC has the following advantages:

1. Higher current density and power density.
2. The anode and cathode polarization are small, and the polarization loss is concentrated in the electrolyte.
3. Can use hydrogen, hydrocarbons, methanol and other fuels directly without using metal catalyst
4. Avoids the corrosion and sealing problems of acid-base electrolyte or molten salt electrolyte of low temperature fuel cells.

5. Provide high-quality waste heat to achieve combined heat and power, high fuel utilization rate, and energy utilization rate of about 80%.
6. Ceramic materials are widely used as electrolyte, cathode and anode.
7. The ceramic electrolyte requires medium and high temperature operation, which can accelerate the reaction of the battery and simplifies the equipment.

1.7 The applications of SOFC

Baur and Preis developed the first solid oxide fuel cell as early as 1937, but it did not develop rapidly until the early 1980s. As with all types of fuel cells, the research and development of SOFC requires significant investment. At present, most of the research and development of SOFC are carried out in scientific research institutions or research institutes of large companies in developed countries. Among them, the United States, Germany, and Japan have made the fastest progress in SOFC research.

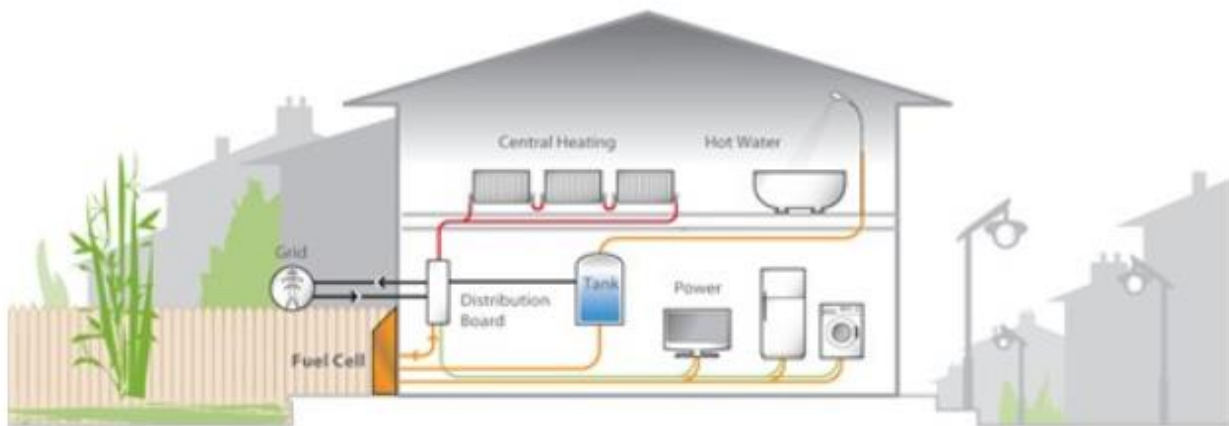


Figure 1.4 Uses of fuel cells in military application^[29].

1. Distributed power generation / cogeneration system

(1) Siemens Westinghouse Power Company^[30]

In 1986, the 400 W tubular SOFC battery pack developed by Siemens Westinghouse Power Company successfully operated in Tennessee, the United States; in 1987, 3 kW-class tubular SOFC

generator sets were installed in Tokyo, Japan and Osaka Gas Company, respectively, and successfully carried out continuous The operation test lasted for 5000 hours, marking the development of SOFC research from experimental research to commercial development. In 1998, the company's 100 kW tubular SOFC power station developed by the company was operated in the Netherlands; in 1992, two 25 kW tubular SOFCs were respectively in Osaka, Japan, For thousands of hours of experimental operation in Southern California, the United States; in 2000, the company designed and manufactured the world's first 220 kW SOFC / GT combined cycle power plant.

(2) Mitsubishi Heavy Industries^[31]

Mitsubishi Heavy Industries began developing SOFC technology in 1984. From 1986 to 1989, co-developed a tubular SOFC cell stack with Tokyo Electric Power Co., Ltd .; in 1991, a 1 kW SOFC cell stack was run for 1000 hours; in 1993, Mitsubishi Heavy Industries developed a new 1 kW SOFC cell stack and succeeded It operated for 3000 hours; in 1996, 10 kW atmospheric SOFC operated continuously for 5000 hours. In 2001, Mitsubishi Heavy Industries and Electric Power Development Co., Ltd. jointly developed a 10kW class pressurized tube-type SOFC power generation system. This system uses natural gas as fuel and adopts internal reforming mode to continuously work for more than 755 hours. When the 10kW system is operated at a design current of 64A, its electrical output power is 10.2 kW and the power generation efficiency is 41.5% (HHV). When the current is 80A, the system's electrical output power can reach 11.5kW; in 2013, Mitsubishi Heavy Industries' 200kW The SOFC + MGT composite power generation system has been running continuously for more than 4,000 hours in Tokyo Gas's Senju Technology Center. The operating temperature of the system is about 900 ° C and the power generation efficiency is 50.2% (LHV).

(3) Bloom energy^[32]

Bloom Energy is a US company dedicated to clean energy. Founded in 2001, it is headquartered

in Sunnyvale, California. The company mainly produces SOFC distributed power. The main products are ES5, ES-5700, ES5710 and so on. Bloom Energy has provided more than 100 SOFC systems for companies such as Google, eBay and Wal-Mart in the United States.

(4) Suzhou Huaqing Jingkun New Energy Technology Co., Ltd.

Huaxin Energy was established in 2010. Its main business includes new energy technology, new material technology products, etc., specific products related to SOFC, such as SOFC single cells, stacks, power generation systems and kilowatt-level test systems. Type 101, HS-102, HS-102, etc.

2. Power source

Nissan released the world's first fuel cell prototype vehicle powered by a SOFC power system. The car is based on Nissan's e-NV200, which uses enzyme biofuel-cell technology and uses the SOFC power system to convert stored bioethanol into electricity to power the car, with a range of over 600 kilometers. Currently, the prototype is undergoing further field tests on Brazilian roads, and Nissan also plans to commercialize ethanol SOFC electric vehicles in 2020^[33].

The biggest highlight of Nissan's SOFC electric vehicle is that the fuel used is liquid bioethanol instead of hydrogen. Considering the serious lag in infrastructure construction such as hydrogen refueling stations and high construction costs, and the fact that ethanol is cheaper, more convenient and safer than hydrogen in manufacturing, transportation, and storage, ethanol SOFC electric vehicles may break the hydrogen proton exchange membrane fuel cell vehicles "Monopoly" has become the main force to open the global market.

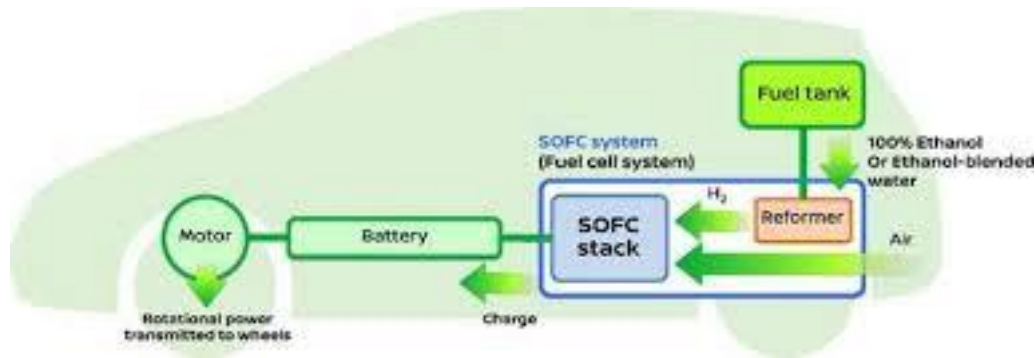


Figure 1.5 Nissan SOFC Electric Vehicle Power System

1.8 The materials of SOFC

The unit structure of SOFC includes a porous cathode and anode, a dense electrolyte, and a connector which is needed to connect each other. The material research of SOFC is mainly the research on the first three types of materials. The selected materials must meet the following basic requirements: sufficient electrical conductivity at the operating temperature; good chemical compatibility and structural stability between the various components; and matching thermal expansion coefficients between different components. In addition, each component has its own different requirements.

1.1.1 Solid electrolyte

Among electrolytes and electrode materials, the research and development of electrolyte materials is the core of SOFC research and development. The electrolyte performance directly determines the battery's operating temperature and performance. The electrolyte of a solid oxide fuel cell is an oxygen ion conductive electrolyte. There are various oxide structures with oxide examples, such as fluorite structure, perovskite structure, pyrochlore and brownmillerite.

The most typical subvalent dopants are Ca^{2+} and Y^{3+} . They can produce calcia-stabilized zirconia (CSZ) and yttria-stabilized zirconia (YSZ), respectively. YSZ can exhibit good oxide-ion conductivity above 700 °C which is used most widely now^[34]. For superior ionic conductivity, Sc-doped zirconia (ScSZ) also work well. But its use is limited by high cost of scandium. Compared to zirconia at low temperatures, ceria particularly shows a higher ionic conductivity. The oxygen vacancies are the main compensating defects in ceria.

With the same doping conditions, the ionic conductivity of ceria is greater than that of the stabilized zirconia, about an order of magnitude. The reason is that Ce^{4+} (0.97 Å in 8-coordination) has a larger ionic radius than Zr^{4+} (0.84 Å), which produces more space in the structure which O^{2-} ions migrate. In the reduced fuel environment, single-phase cation doped ceria exhibits certain

electronic conduction^[34-36]. There are many works have been done to overcome Ce^{4+} to Ce^{3+} , which is the ceria instability due to electronic conduction in the fuel cell operation. It is reported that the above problem can be suppressed by doping YSZ into Sm-doped cerium oxide which can form a composite electrolyte^[37]. In the composite electrolyte, SDC grains could be dispersed into YSZ matrix, so that the electronic contribution is blocked by the YSZ matrix. In recent years, ceria based double phase composite electrolytes, such as GDC- Al_2O_3 and GDC-NaCl, have been researched a lot. These composite materials can effectively solve the problem of Ce^{4+} to Ce^{3+} . But for the conductivity, such composite materials don't have good performance. The work is still needed in the future.

Zhu and co-workers come up with a new way of nanocomposites^[38-42]. The idea of nanocomposites is based on combining cerium dioxide-based nano powders with a second phase (usually an insulating phase). At lower temperatures (300-600 °C), the nanocomposites exhibit superionic conductivity. This introduces a new SOFC class of low temperature SOFC (LT-SOFC). In the previous section, the characteristics, advantages and disadvantages of solid electrolytes developed for SOFC have been discussed in detail.

1.8.1.1. Zirconia based solid electrolytes

Zirconia-based solid electrolytes with a dopant concentration of 8-10 mol% are considered as effective ion transport media for high performance SOFCs. Almost all of the SOFC systems currently under development use stable zirconia because it has sufficient oxide ion conductivity levels and has the required stability in the oxidizing and reducing atmospheres. The widely used dopants are CaO, MgO, Y_2O_3 , and Sc_2O_3 and certain rare earth oxides^[43-49]. When the concentration of the acceptor-type dopant approaches the minimum required to completely stabilize the cubic fluorite structure, the maximum ionic conductivity in a ZrO_2 -based system is observed^[50-52]. Higher dopant concentration can increase the combine ability between oxygen vacancies and dopant cations to the complex defects. Generally, this trend increases as the difference between the host and dopant ion radius increases^[53-55].

Doping aluminum cations can stabilize the zirconia fluorite cubic structure from room temperature to the melting point (2680 °C). And it can increase the number of oxygen vacancies. At higher dopant concentrations, the conductivity decreases due to defect ordering, vacancy aggregation, and electrostatic interactions. It shows the highest oxide ion conductivity in ScSZ of 0.15-0.20 S·cm⁻¹ at 1000 °C [56].

It has been reported that various transition metal oxides co-doped with yttria-stabilized zirconia can enhance ionic conductivity. The 8YSZ-doped Mg²⁺ ion shows an enhanced conductivity of 8YSZMg_{0.5} with a maximum value of 0.0345 S / cm, while the conductivity of 8YSZ at 800 °C is 0.015 S / cm. YSZ meets all requirements, but due to its interaction with muscovite, the reactivity was problematic at higher temperatures containing lanthanum oxide cathodes. It will react with La to form a La₂Zr₂O₇ resistive layer [57].

Recently, Lee et al. have reported a functional Bi_{1.6}Er_{0.4}O₃ (ESB) /Y_{0.16}Zr_{0.84}O_{1.92} material for double-layer solid electrolyte through screen printing with ESB powder on a screen-cast NiO / YSZ anode support. At 700 °C (OCV > 1.1 V), it has reached a maximum power density of 2.1 W / cm², which is 2.4 times that of YSZ-based SOFC. Enhanced oxygen bonding process at the cathode / electrolyte interface improves SOFC performance [58]. Cui et al. have reported Yb₂O₃ doped 8YSZ material and its composite 8YSZ - 4Yb₂O₃ - NaCl/KCl electrolytes. For 8YSZ-4Yb₂O₃ - NaCl/KCl (sintered at 800 °C), a maximum conductivity of 6.1 × 10⁻¹ S/cm was observed at 700 °C. At 700 °C, the maximum power density is 364 mW/cm², resulting in excellent fuel cell performance [59].

An IT-SOFC has been developed recently that includes the following components: a thin film YSZ for manufacturing electrolytes, LSCF / YSZ as a cathode, and NiO-YSZ as an anode or a combination of all three components NiOYSZ-LSCF to make semiconductor ions Membrane (SIM) and device [45]. Compared with traditional SOFC, this SIM device shows higher OCV and power output. In traditional SOFC, OCV and power output loss due to internal short circuit. STEM-EELS analysis shows that the oxygen enrichment at the interface between NiZ-YSZ and LSCF-YSZ is more obvious, which is consistent with enhanced fuel cell performance [60]. From

these results, it can be seen that the ESB / YSZ double layer is a viable option as a solid electrolyte for high-performance SOFC at reduced temperatures.

1.8.1.2. Bi₂O₃-based electrolytes

Of all oxide ion-conducting materials, the oxide phase derived from Bi₂O₃ has got particular interest due to its high ionic conductivity relative to other solid electrolytes. Bi₂O₃ shows a significant polymorphism of two stable phases, a and d^[61]. High electrical conductivity occurs at the d-phase fluorite-type structure in high-temperature. Phase d is stable only above 730 °C. The neutron total scattering technique was used to study the local structure and ion migration path in d- Bi₂O₃^[62,63]. They report that from conventional X-ray or neutron diffraction, it can be seen that the long-range order is consistent with cubic symmetry, and the d phase local structure is very similar to the twisted one found in the pure material phase which is stable at room temperature. Some people believe that the asymmetric electron density around Bi³⁺ ions is essential to promote a wide range of anion disturbances in d- Bi₂O₃, while the flexible cationic sublattice and sufficient relaxation of surrounding anions promote ion diffusion.

The temperature at which the d-Bi₂O₃ phase stabilizes to 973-1073 K can be achieved by replacing bismuth with a rare-earth dopant (such as Y, Dy or Er) and combining them with higher valence cations (such as V, W or Nb)^[64]. Maximum conductivity was observed in systems doped with Er (Bi_{1-x}Er_xO_{1.5}, x = 0.20) and Y (Bi_{1-x}Y_xO_{1.5}, x = 0.23-0.25). These systems are stable only over the temperature range of 1043-1143 °C, and they undergo phase changes beyond this limit and cause a decrease in conductivity.

Adding Bi₂O₃ to scan-doped zirconia shows enhanced ionic conductivity. Higher conductivity was observed in 10ScSZ (10 mol% Sc₂O₃) doped with bismuth oxide. The electrical conductivity of 10ScSZ doped with 1 mol% of Bi₂O₃ at 1000 °C was found to be 0.33 S/cm. The undoped sample has a rhombic crystal structure at room temperature with a conductivity lower than that of the cubic phase. At higher temperatures, a transition to a cubic phase occurs. Adding Bi₂O₃ (2 mol%) to 10ScSZ stabilizes the cubic phase at lower temperatures and shows a maximum conductivity of

0.18 S/cm at 600 °C.

1.8.1.3. LaGaO₃-based electrolytes

Gallium lanthanum gallate (LaGaO₃) is widely studied for IT-SOFC perovskite structure oxides. In the large cation LaGaO₃, La³⁺ is surrounded by 12 O²⁻ anions, and Ga³ cations occupy 6 coordinate positions, forming a network sharing the octahedral angle of GaO₆^[65]. By replacing La³⁺ into the gallium sublattice with an alkaline earth metal element (such as Mg²⁺), the high oxide ion conductivity in LaGaO₃ can be increased to increase the concentration of oxygen vacancies. It can provide the largest oxygen ion mobility by following the principle of minimal lattice distortion. Compared with Ca and Ba, doping Sr results in higher ionic conductivity. Ishihara and Feng first reported the high ionic conductivity of LaGaO₃ doped with (Sr, Mg), which was La_{1-x}Sr_xGa_{1-y}Mg_yO_{3-δ} (LSGM) in 1994^[66,67]. From the literature, the maximum ion conductivity can be reached at x = 0.10-0.20 and y = 0.15-0.20, and further doping will lead to vacancy association. Neutron diffraction studies have determined that simultaneous doping of Sr and Mg will cause the tilt of the GaO₆ octahedron with respect to the parent compound to decrease.

By doping smaller cations at the A position, a decrease in conductivity can also be observed. Introducing a small amount of cations with variable valence (such as cobalt) at the gallium site will increase the ionic conductivity of LSGM and cause a slight increase in electronic conductivity^[68-69]. Computational techniques were used to examine the defect chemistry and migration path of oxides in lanthanum gallate, and the findings indicate that migration occurs through vacancy jumps between the oxygen sites along the edge of the GaO₆ octahedron, with a slightly curved trajectory accompanied by outward release of adjacent cations^[70-71].

In contrast, Mg-vacancy clusters have significant binding energies, suggesting greater vacancy trapping. This is consistent with the increased activation energy for ion migration at higher Mg doping levels in La_{1-x}Sr_xGa_{1-y}Mg_yO_{3-δ}

In contrast, magnesium vacancy clusters have great binding energies, which is indicating greater vacancy trapping. This is related to the increased ion migration activation energy in La_{1-x}Sr_xGa₁₋

$y\text{Mg}_y\text{O}_{3-\delta}$ at higher Mg doping levels^[72]. This results in two different regions or non-linear parts in the Arrhenius plot of the conductivity. The doping of barium instead of strontium will affect the octahedral inclination angle and reduce the activation energy. Therefore, the electrical conductivity of $\text{La}_{0.9}\text{Ba}_{0.1}\text{Ga}_{0.8}\text{Mg}_{0.2}\text{O}_{2.85}$ is lower than that of $\text{La}_{0.9}\text{Sr}_{0.1}\text{Ga}_{0.8}\text{Mg}_{0.2}\text{O}_{2.85}$ at high temperature, but the opposite is true at lower temperatures.

To other lanthanum-based perovskites, such as LaSrO_3 , LaInO_3 and LaYO_3 , they are also used as oxygen ion conductors^[73]. Due to the problems such as phase instability, high reactivity with Ni and volatility of gallium at high temperatures, the use of LSGM electrolytes is still small, which leads to the formation of a LaNiO_3 phase.

1.8.1.4. Doped/co-doped ceria electrolytes

Similar to zirconia, cerium dioxide also has a fluorite structure, which is a common electrolyte for SOFC. It has excellent compatibility with SOFC electrodes. Compared with stable zirconia, doped ceria has a higher ionic conductivity, especially at lower temperatures, which is attributed to its large ionic radius of 0.97 Å (8 times coordination). The main compensation defect of cerium oxide is oxygen vacancy.

Sm and Gd doped cerium oxide were the best ionic conductor in all the noble metals for IT-SOFC. The ionic conductivity of $\text{Ce}_{0.9}\text{Gd}_{0.1}\text{O}_{1.95}$ (CGO10) at 500 °C is 0.01 S/cm. Moreover, other rare earth cations (such as lanthanum [71-73] and Nb^[77]) are also used as dopants in cerium dioxide. Arai et al. investigated the effect of doping alkaline earth metal oxides (such as CaO, SrO, MgO, and BaO) in cerium oxide^[78]. The dopant of CaO and SrO can improve the conductivity of CeO_2 . However, due to the size mismatch of Mg^{2+} (0.89 Å), Ba^{2+} (1.42 Å) and the Ce^{4+} (0.97 Å), the dopant of BaO and MgO did not significantly improve the conductivity compared to CaO and SrO.

Kim et.al. proposed the concept of the critical ion radius of a dopant. It is the ideal doped cation radius, which has the same radius as the undoped ceria. The critical ionic radii of trivalent and divalent dopants in cerium dioxide are 1.038 Å and 1.11 Å, respectively. For example, although the ionic radii of Gd^{3+} (1.053 Å) and Sm^{3+} (1.079 Å) are larger than the ionic radii of Y^{3+} (1.019 Å),

Gd³⁺ and Sm³⁺ doped cerium dioxide has a higher ionic radius than Y³⁺. Kilner et al. and Catlow suggests that a small ionic size mismatch between the host and the dopant is responsible for the high conductivity^[79-81].

Herle et al. reported that two or more cations co-doping of ceria (such as alkaline earth and rare earth cations) can increase the conductivity than only one cation doped ceria. Some kind of materials have been investigated such as: Ce_{0.85}Gd_{0.10}Mg_{0.05}O_{1.90}, Ce_{0.8}Gd_{0.2-x}Sm_xO_{1.90}, Ce_{1-x-y}Gd_xPr_yO_{2-z}, Ce_{0.80}Sm_{0.20-x}Y_xO_{1.90}, Ce_{0.70}Sm_{0.15}Ge_{0.15}O_{2-δ}, Ce_{0.99-x}Gd_xCu_{0.01}O_{2-δ} (0 < x < 0.3), Ce_{0.8}Pr_{0.2-x}Dy_xO_{2-δ}, Ce_{0.8}Sm_xGd_yNd_zO_{1.9} (x, y and z = 0.2, 0.1, 0.0667 or 0 and x + y + z = 0.2) etc^[82-90].

By Mori et al., an effective index *Ei* is defined to explain the oxide ion conductivity trend of co-doped cerium oxide electrolytes^[91]. They reported that CeO₂-based systems achieve the ideal fluorite structure and show the largest ionic conductivity when the effective index approaches 1. *Ei* can be defined as:

$$Ei = \frac{\text{avg.rc} \times \text{rd}}{\text{eff.ro} \times \text{rh}} \quad (2)$$

where, avg.rc is the average ionic radius of the cations, eff.ro is the effective ionic radius of oxygen ion, rd is the average ionic radius of the dopant and rh is the radius of host cation.

Written by Yammamura et al., it has been reported that the oxygen vacancies ordering is suppressed due to co-doping^[92]. This promotes the configurational entropy of the system and subsequently reduces the activation energy. The overall conductivity is increased by this. The structural entropy *S* of a typical system with a constant number of oxygen vacancies Ce_{1-x-y}M'_xM_yO_{2-δ} can be expressed as:

$$S = R[(1-x-y)\ln(1-x-y) + x\ln x + y\ln y] \quad (3)$$

where 'R' is the gas constant (8.314 J/mol-K). Co-doped ceria systems have higher configurational entropy than that of singly doped ceria.

From previous studies, it has been reported that the vacancies are not free which are created by the

doping of aluminum-valent cations. They combine with dopants to form related defect pairs or clusters^[93]. By Li et al., it is reported that the vacancy association of dopants leads to the formation of ordered defect clusters. And these defect clusters further develop into ordered nano-sized domains. Associative energy is related to two factors: (i) Gōlen interaction, which is an electrostatic interaction due to different valences; (ii) elastic strain due to the size mismatch between the dopant and the cation. They performed atomic simulation studies of defect aggregation and ordering in atomically cation-doped ceria. It is reported that there are two possible preferred sites for dopant-vacancy correlation pairs.

Compared with divalently doped cerium oxide, trivalent cation-doped cerium oxide shows high ionic conductivity. For some co-doped systems, such as $\text{Ce}_{0.85}\text{Sm}_{0.15-x}\text{Gd}_x\text{O}_{1.925}$ ^[94], $\text{Ce}_{1-x-y}\text{Mg}_x\text{La}_y\text{O}_{2-(x+y)/2}$ ^[95] and $\text{Ce}_{1-x-y}\text{Al}_x\text{La}_y\text{O}_{2-(x+y)/2}$ ^[96], the effect of doping in ceria was analyzed using the concepts of radius ratio ($r_d = r_h$) and effective ion index. Compared to the $\text{Ce}_{0.85}\text{Sm}_{0.15}\text{O}_{1.925}$ composition, the ratio $r_d = r_h$ of the $\text{Ce}_{0.85}\text{Gd}_{0.15}\text{O}_{1.925}$ composition is closer to 1. Therefore, it shows the maximum electrical conductivity. Compared with the composition $\text{Ce}_{0.85}\text{Sm}_{0.09}\text{Gd}_{0.06}\text{O}_{1.925}$, the E_i value of the composition $\text{Ce}_{0.85}\text{Sm}_{0.09}\text{Gd}_{0.06}\text{O}_{1.925}$ is closer to 1. Therefore, the conductivity with the composition of $x = 0.06$ is greater than the conductivity with $x = 0.09$.

1.8.2 Cathode material^[97,98]

The main function of the SOFC cathode is to provide a place for the electrochemical reduction reaction of the oxidant. Therefore, the cathode material must have the following properties:

- (1) Stability in an oxidizing atmosphere.
- (2) Have sufficient electronic and ionic conductivity.
- (3) It has a catalytic effect on oxygen ionization at the operating temperature of the battery.
- (4) It has sufficient porosity to make the oxidant easily diffuse to the reaction catalytic active surface.

Sr^{2+} doped lanthanum manganate is the most commonly used cathode material in traditional SOFC.

However, the oxygen ion conductivity of LSM is relatively low, only $10^{-7} \text{ S} \cdot \text{cm}^{-1}$ at $900 \text{ }^\circ\text{C}$. Therefore, LSM cannot be used as the cathode material of IT-SOFC. In order to enhance the electrochemical catalytic performance of fuel cell cathode materials under low temperature operation, many new cathode materials have been studied to replace LSM, such as $\text{Sm}_{0.5}\text{Sr}_{0.5}\text{CoO}_{3-\delta}$, $\text{La}_{1-x}\text{Sr}_x\text{Co}_{1-y}\text{Fe}_y\text{O}_{3-\delta}$, $\text{Ba}_x\text{Sr}_{1-x}\text{Co}_{1-y}\text{Fe}_y\text{O}_{3-\delta}$ and so on.

1.8.3 Anode material^[98-100]

The main function of the SOFC anode is to provide a place for the electrochemical oxidation reaction of the fuel. Therefore, the anode material must have the following properties:

- (1) Stability under reducing atmosphere.
- (2) It must also have sufficient electronic and ionic conductivity.
- (3) It has electrochemical catalytic performance for fuel gas at the operating temperature of the battery.
- (4) The anode must have sufficient porosity to make the oxidant easily diffuse to the reaction catalytic active surface.

Traditional SOFC generally uses Ni-YSZ cermet composite materials as anode materials. Because Ni-YSZ has relatively high catalytic performance and low price. Adding YSZ into Ni material has three functions:

- (1) The thermal expansion coefficient of the Ni material matches the thermal expansion coefficient of other battery components.
- (2) Prevent Ni particles from agglomerating and growing up.
- (3) Provide an oxygen ion diffusion channel.

The anode must have a porous structure to facilitate the diffusion of the fuel reaction gas.

1.9 Research aims

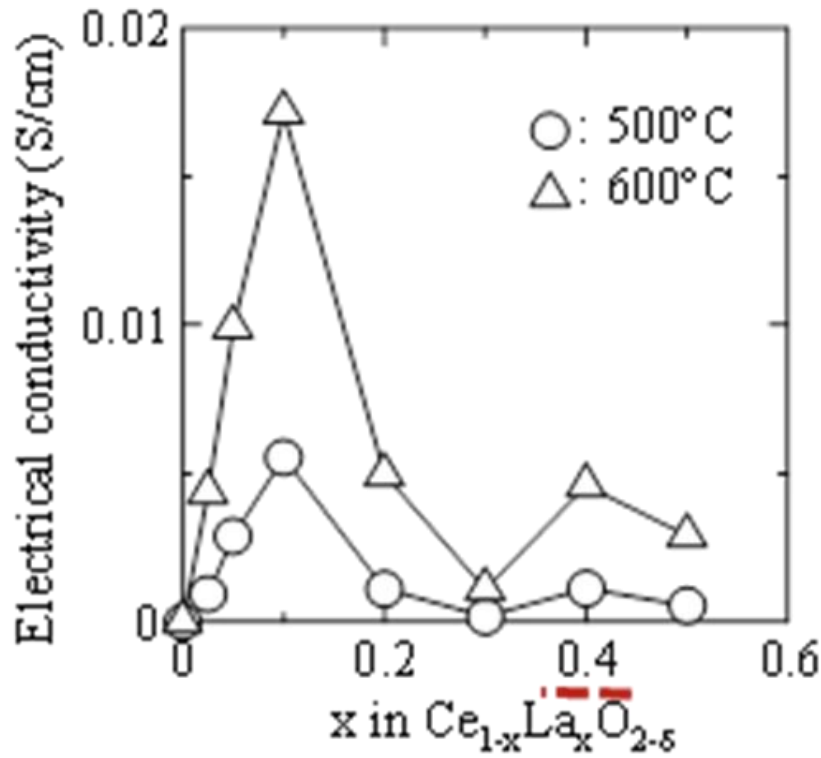


Figure 1.6 The conductivity of different doping amount in LDC material^[101].

According to a previous report, the electrical conductivity is related with the calcined temperature. Otherwise, the electrical conductivity of Ce_{1-x}La_xO_{2-δ} (LDC) shows a specific behavior at x = 0.3. Usually, the conductivity of a ceria-type material has the highest value at 0.1 ≤ x ≤ 0.2 and continues to decrease with an increase in the amount of La^[101]. However, as Figure 1.2 indicates, the conductivity of LDC shows an increasing trend again from x ≥ 0.3. According to some previous studies, the electrical conductivity changes with the local structure^[102,103]. For example, oxygen ordering in a rare earth C-type oxide has been detected in La₂Ce₂O₇. The composition of La₂Ce₂O₇ is nominally associated with the pyrochlore-type structure, which can be considered an ordered defect fluorite-type structure. Assuming that Ln₂Ce₂O₇ has a pyrochlore structure, the coordination number of a larger Ln³⁺ ion is 8, whereas that of a smaller Ce⁴⁺ ion is 6, which indicates that a disproportion in the coordination numbers occurs owing to a difference in the cation sizes. In the case of zirconate, the electrical conductivity in Ln₂Zr₂O₇ increases with an increase in the ionic

radius of Ln^{3+} in the fluorite-type phase region, and finally shows the maximum value within the vicinity of the phase boundary in the pyrochlore-type region. Thus, we suspect that a local structural change also occurs in our target materials.

In the first and second part, we introduce La and Gd individually into ceria to study the local structural change. We introduced XAFS to analyze the results. Based on the results, we obtained the regularities of the materials with different levels of doped La and Gd as well as the relationship between the conductivity and local structural change. The proposed method aims to be a practical approach for solving structural problems in the future.

BaCeO_3 has low chemical stability under CO_2 and H_2O atmospheres. In contrast, BaZrO_3 has excellent chemical stability. However, high sintering temperature and long sintering duration are required to obtain a high density BaZrO_3 material. Therefore, in the third part, in order to obtain a high density sample, a sintering aid such as ZnO or CuO would be required. In addition, it has been reported that the relative density could be improved by an introduction of A-site deficiency in the SrTiO_3 -based material. In this study, we report structure changes of $\text{Ba}_{1-x}\text{Zr}_{0.9}\text{Y}_{0.1}\text{O}_{3-\delta}$ ($x=0, 0.04$) sintered with ZnO as a sintering aid, and characterizations of the composite materials. Also according to the previous literature^[104,105], BaO pellet will have sublimation and surface decomposition due to the high temperature (up to $1700\text{ }^\circ\text{C}$) to obtain a dense material. We plan to make a new method to prevent BaO vapor and Y getting aggregation from the surface of the pellet.

Reference

- [1] George Wand, Johnson Matthey plc: 14. [on line]
- [2] International Association for Hydrogen Energy. [on line]
- [3] EnergyGroove.net. [on line]
- [4] Tex Tech Industries. [on line]
- [5] Larminie, James (1 May 2003). Fuel Cell Systems Explained, Second Edition. SAE International.
- [6] Wang, J.Y. (2008), International Journal of Hydrogen Energy. 33 (21): 6339–6350.
- [7] Wang, J.Y.; Wang, H.L. (2012), Fuel Cells. 12 (6): 989–1003.
- [8] Wang, J.Y.; Wang, H.L. (2012), International Journal of Hydrogen Energy. 37 (14): 10881–10897.
- [9] Williams, K.R. Biographical Memoirs of Fellows of the Royal Society. (1994), 39: 2–9.
- [10] Srivastava, H. C. Nootan ISC Chemistry (12th) Edition 18, (2014), pp. 458–459.
- [11] Department of Energy Energy Efficiency and Renewable Energy Fuel Cell Technologies Program. 7 July 2011. Accessed 3 August 2011. [on line]
- [12] americanhistory.si.edu. [on line]
- [13] scopeWe - a Virtual Engineer. [on line]
- [14] Samuel Simon Araya, Fan Zhou, et.al, international journal of hydrogen energy, 41, (2016) 21310-21344.
- [15] U.S. Department of Energy, accessed 9 August 2011. [on line]
- [16] FCTec.com, accessed 9 August 2011 Archived 3 March 2012 at the Wayback Machine. [on line]
- [17] FuelCell Energy, accessed 9 August 2011 Archived 11 January 2013 at Archive. [on line]
- [18] Ermete Antolini, Applied Energy 88 (2011) 4274–4293.
- [19] Linan Shu, Jaka Sunarso, et al, International journal of hydrogen energy, 44, (2019), 31275 - 31304.
- [20] I. Sreedhar, Bhawana Agarwal, Priyanka Goyal, Satyapaul A. Singh, Journal of

Electroanalytical Chemistry, 848, (2019), 113315.

[21] Nandini Jaiswal, Khagesh Tanwar, et.al, Journal of Alloys and Compounds, 781, (2019), 984-1005.

[22] Huicui Chen, Xin Zhao, Tong Zhang, Pucheng Pei, Energy Conversion and Management, 182, (2019), 282–298.

[23] Christophe Lin-Kwong-Chon, Brigitte Grondin-Pérez, Jean-Jacques Amangoua Kadjo, Cédric Damour, Michel Benne, Annual Reviews in Control, 47, (2019), 133–154.

[24] Tong Zhang, Peiqi Wang, Huicui Chena, Pucheng Pei, Applied Energy, 223, (2018), 249–262.

[25] 刘洁, 王菊香, 邢志娜,等. 节能技术, 2010, 28(4): 364-368.

[26] 燃料电池及其关键材料发展趋势, 中国电池网

[27] 王华文,齐国祯, [J].高桥石化, 2005 , 20 (3): 46.

[28] J.H. Hirschenhofer, D.B. Stauffer, R.R. Engelman, M.G. Klett, Fuel Cell Handbook, fourth ed., US Department of Energy Federal Energy Technology Center, 1998.

[29] U.S. Energy Information Administration.

[30] Hassmann, Klaus. (2001). SOFC Power Plants, the Siemens-Westinghouse Approach. Fuel Cells.

[31] YUKIO YOSHIDA, NAGAO HISATOME, KOICHI TAKENOBU, Technical Review Vol.40 No.4 (Aug. 2003).

[32] bloomenergy.com. [on line]

[33] A fuel cell system that generates electricity from bioethanol to power a vehicle, Nissan-global.com. [on line]

[34] R. Doshi, V.L. Richards, J.D. Carter, X. Wang, M. Krumpelt, J. Electrochem. Soc. 146, (1999), 1273-1278.

[35] M. Godickemeier, K. Sasaki, L.J. Gauckler, in: Proc. Second Eur. Solid Oxide Fuel Cell Forum, Oslo, Norw, 1996, pp. 17-726.

[36] L.C. Li, L.Z. Lu, H.Q. Xie, J. Mater. Sci. Technol. 14 (1998) 451-456.

- [37] A. Atkinson, *Solid State Ionics* 95 (1997) 249-258.
- [38] B. Zhu, S. Li, X.L. Sun, J.C. Sun, *Molten Salts Ion, Liq. Never Twain*, U.S, 2010.
- [39] B. Zhu, *J. Power Sources* 93 (2001) 82-86.
- [40] B. Zhu, X.T. Yang, J. Xu, Z.G. Zhu, S.J. Ji, M.T. Sun, J.C. Sun, *J. Power Sources*, 118, (2003), 47-53.
- [41] Q.X. Fu, S.W. Zha, W. Zhang, D.K. Peng, G.Y. Meng, B. Zhu, *J. Power Sources*, 104, (2002), 73-78.
- [42] B. Zhu, X. Liu, M. Sun, S. Ji, J. Sun, *Solid State Sci.*, 5, (2003), 1127-1134.
- [43] D.W. Strickler, W.G. Carlson, *J. Am. Ceram. Soc.* 47 (1964) 122-127.
- [44] J.M. Dixon, L.D. LaGrange, U. Merten, C.F. Miller, J.T. Porter, *J. Electrochem. Soc.* 110 (1963) 276-280.
- [45] X. Guo, J. Maier, *J. Electrochem. Soc.* 148 (2001) E121-E126.
- [46] T.-H. Yeh, W.-C. Hsu, C.-C. Chou, *J. Phys. IV EDP Sci.*, (2005), 213-219.
- [47] O. Yamamoto, Y. Arati, Y. Takeda, N. Imanishi, Y. Mizutani, M. Kawai, Y. Nakamura, *Solid State Ionics*, 79, (1995), 137-142.
- [48] H.A. Johansen, J.G. Cleary, *J. Electrochem. Soc.* 111, (1964), 100-103.
- [49] D.K. Hohnke, *J. Phys. Chem. Solid.* 41, (1980), 777-784.
- [50] E. Djurado, F. Boulch, L. Dessemond, *Electrochemical Society Proceedings 2003-07 SOFC VII*, 2003, p. 160.
- [51] V. V Kharton, E.N. Naumovich, A.A. Vecher, *J. Solid State Electrochem.* 3 (1999) 61-81.
- [52] O. Yamamoto, Y. Arachi, H. Sakai, Y. Takeda, N. Imanishi, Y. Mizutani, M. Kawai, Y. Nakamura, *Ionics (Kiel)* 4 (1998) 403-408.
- [53] H.J.M. Bouwmeester, A.J. Burggraaf, in: A. Burggraaf, L. Cot (Eds.), Elsevier, Amsterdam, 1996, pp. 435-528.
- [54] N.M. Sammes, G.A. Tompsett, H. Nēafe, F. Aldinger, *J. Eur. Ceram. Soc.* 19, (1999), 1801-1826.
- [55] M. Mogensen, N.M. Sammes, G.A. Tompsett, *Solid State Ionics*, 129, (2000), 63-94.

- [56] M. Hirano, S. Watanabe, E. Kato, Y. Mizutani, M. Kawai, Y. Nakamura, *J. Am. Ceram. Soc.* 82, (1999), 2861-2864.
- [57] A.J. Jacobson, *Chem. Mater.* 22, (2010), 660-674.
- [58] D.W. Joh, J.H. Park, D. Kim, E.D. Wachsman, K.T. Lee, *ACS Appl. Mater. Interfaces* 9 (2017) 8443-8449.
- [59] Y. Cui, R. Shi, J. Liu, H. Wang, H. Li, *Materials* 11 (2018) 1824-1833.
- [60] Y. Cai, B. Wang, Y. Wang, C. Xia, J. Qiao, P.A. Aken, *J. Power Sources* 384, (2018), 318-327.
- [61] T. Takahashi, H. Iwahara, Y. Nagai, *J. Appl. Electrochem.* 2, (1972), 97-104.
- [62] S. Hull, S.T. Norberg, M.G. Tucker, S.G. Eriksson, C.E. Mohn, S. Stølen, *Dalton Trans.* (2009), 8737-8745.
- [63] C.E. Mohn, S. Stølen, S.T. Norberg, S. Hull, *Phys. Rev. Lett.* 102 (2009), 155502-1-155502-4.
- [64] V.V. Kharton, F.M.B. Marques, A. Atkinson, *Solid State Ionics*, 174, (2004), 135-149.
- [65] L. Malavasi, C.A.J. Fisher, M.S. Islam, *Chem. Soc. Rev.* 39, (2010), 4370-4387.
- [66] T. Ishihara, H. Matsuda, Y. Takita, *J. Am. Chem. Soc.* 116, (1994), 3801-3803.
- [67] M. Feng, J.B. Goodenough, *Inorg. Chem.* 31, (1994), 663-672.
- [68] F. Goutenoire, O. Isnard, E. Suard, O. Bohnke, Y. Laligant, R. Retoux, P. Lacorre, *J. Mater. Chem.* 11, (2001), 119-124.
- [69] M. O'keeffe, B.G. Hyde, The solid electrolyte transition and melting in salts, *Philos. Mag.* 33, (1976), 219-224.
- [70] M.S. Khan, M.S. Islam, D.R. Bates, *J. Phys. Chem. B*, 102, (1998), 3099-3104.
- [71] M.S. Islam, R.A. Davies, *J. Mater. Chem.*, 14, (2004), 86-93.
- [72] S. Li, B. Bergman, Doping effect on secondary phases, *J. Eur. Ceram. Soc.* 29, (2009), 1139-1146.
- [73] T.Y. Chen, K.Z. Fung, *Electrochemical Society Proceedings*, 2003-07, SOFC VII, 2003, pp. 339-348.
- [74] E. Suda, B. Pacaud, M. Mori, *J. Alloys Compd.* 408, (2006), 1161-1164.

- [75] X. Sha, Z. Lü, X. Huang, J. Miao, Z. Ding, X. Xin, W. Su, *J. Alloys Compd.* 428, (2007), 59-64.
- [76] T. Shimonosono, Y. Hirata, S. Sameshima, T. Horita, *J. Am. Ceram. Soc.*, 88, (2005), 2114-2120.
- [77] K. Yashiro, T. Suzuki, A. Kaimai, H. Matsumoto, Y. Nigara, T. Kawada, J. Mizusaki, J. Sfeir, *Solid State Ionics*, 175, (2004), 341-344.
- [78] H. Yahiro, K. Eguchi, H. Arai, *J. Mater. Sci.*, 23, (1988), 1036-1041.
- [79] D.J. Kim, *J. Am. Ceram. Soc.*, 72, (1989), 1415-1421.
- [80] C.R.A. Catlow, *Solid State Ionics*, 12, (1984), 67-73.
- [81] J.A. Kilner, *Solid State Ionics*, 8, (1983), 201-207.
- [82] J.V. Herle, D. Seneviratne, A.J. McEvoy, *J. Eur. Ceram. Soc.* 19, (1999), 837-841.
- [83] F.Y. Wang, S. Chen, Q. Wang, S. Yu, S. Cheng, *Catal. Today*, 97, (2004), 189-194.
- [84] N. Kim, B.H. Kim, D. Lee, *J. Power Sources*, 90, (2000), 139-143.
- [85] S. Lübke, H.-D. Wiemhöfer, *Solid State Ionics*, 117, (1999), 229-243.
- [86] X. Sha, Z. Lü, X. Huang, J. Miao, L. Jia, X. Xin, W. Su, *J. Alloys Compd.*, 424, (2006), 315-321.
- [87] M.S. Arshad, R. Raza, M.A. Ahmed, G. Abbas, A. Ali, A. Rafique, M.K. Ullah, S. Rauf, M.I. Asghar, N. Mustaq, S. Atiq, *Ceram. Int.*, 44, (2018), 170-174.
- [88] T.H. Santos, J.P.F. Grilo, F.J.A. Loureiro, D.P. Fagg, F.C. Fonseca, D.A. Macedo, Structure, densification and electrical properties of Gd and Cu co-doped ceria solid electrolytes for SOFCs applications: Effect of Gd₂O₃ content.
- [89] C. Madhusudan, K. Venkataramana, C. Madhuri, C.V. Reddy, *J. Mater. Sci. Mater. Electron.*, 29, (2018), 17067-17077.
- [90] A.V.C. Aldridge, R.T. Baker, *Solid State Ionics*, 316, (2018), 9-19.
- [91] T. Mori, J. Drennan, J.H. Lee, J.G. Li, T. Ikegami, *Solid State Ionics*, 154, (2002), 461-466.
- [92] H. Yamamura, E. Katoh, M. Ichikawa, K. Kakinuma, T. Mori, H. Haneda, *Electrochem. Commun.*, 68, (2000), 455-459.

- [93] K. Huang, M. Feng, J.B. Goodenough, *J. Am. Ceram. Soc.*, 81, (1998), 357-362.
- [94] N.K. Singh, P. Singh, D. Kumar, O. Parkash, *Ionics (Kiel)*., 18, (2012), 127-134.
- [95] N. Singh, N.K. Singh, D. Kumar, O. Parkash, *J. Alloys Compd.*, 519, (2012), 129-135.
- [96] N. Singh, O. Parkash, D. Kumar, *Ionics (Kiel)*., 19, (2013), 165-170.
- [97] F. Ramadhani, M.A. Hussain, H. Mokhlis, S. Hajimolan, *Renewable and Sustainable Energy Reviews*, 76, (2017), 460–484.
- [98] Shahzad Hossain, Abdalla M. Abdalla, Siti Noorazeen Binti Jamaina, Juliana Hj Zaini, Abul K.Azad, *Renewable and Sustainable Energy Reviews*, 79, (2017), 750–764.
- [99] Zia Ud Din, Z.A. Zainal, *Renewable and Sustainable Energy Reviews*, 72, (2017), 1050–1066.
- [100] Linan Shu, Jaka Sunarso, Siti Salwa Hashim, Junkui Mao a, Wei Zhou, Fengli Liang, *international journal of hydrogen energy*, 44, (2019), 31275 -31304.
- [101] H. Yamamura, H. Nishino, K. Kakinuma and K. Nomura, *Solid State Ionics*, 158 (2003) 359–365.
- [102] L. Kalland, S. T. Norberg, J. Kyrklund, S. Hull, S. G. Eriksson, T. Norby, C. E. Mohn and C. S. Knee, *Phys. Chem. Chem. Phys.*, 18, (2016) 24070–24080.
- [103] E. Suda, B. Pacaud, Y. Montardi, M. Mori, M. Ozawa and Y. Takeda, *Electrochemistry*, 71 (2003) 866–872.
- [104] F. Iguchi, T. Yamada, N. Sata, T. Tsurui, H. Yugami, *Solid State Ionics* 177 (26–32) (2006) 2381.
- [105] A. Magrez, T. Schober, *Ionics* 11 (2005) 171.

Chapter 2 Preparation and characterization of $\text{Ce}_{1-x}\text{La}_x\text{O}_{2-\delta}$ powder and sintered samples

2.1. Overview of the preparation method

The preparation methods of solid-phase electrolytes can be divided into:

1. Solid state reaction method^[1,2]: including reduction-chemical method, thermal decomposition method, etc.
2. Gas phase reaction method^[3,4]: including gas state synthesis method and gas state thermal decomposition method.
3. Liquid phase reaction method^[5-7]: including sol-gel method, co-precipitation method, uniform precipitation method, solvent removal method, alkoxide hydrolysis method, etc.

The solid-phase reaction method is one of the earliest methods used for doping CeO_2 powders. In recent years, it has been widely used as a laboratory study, and it is a liquid-state synthesis method that has developed rapidly. It will be introduced as following.

(1) Solid state method

Solid-phase chemical reactions are one of the earliest chemical reactions used by humans. Since the beginning of the 20th century, it has been inextricably linked with solid materials science^[8-10]. The solid phase reaction method refers to a product obtained by directly reacting and synthesizing a solid phase reactant at 1000 to 1600 degrees. It has the characteristics of no solvent, high selectivity, high yield, and simple process. Therefore, it is the earliest method used in the synthesis of doped CeO_2 .

Narrow sense solid phase reaction means that the reactant products are all solid phase. The reaction steps are roughly as follows: first the reactants diffuse to the interface, then react at the interface, and finally diffuse through the product. Generally, increasing the reaction temperature can increase the ion diffusion rate. The main factors affecting the reaction rate are:

1. The surface area of the reactant solids and the contact area between the reactants.

2. The nucleation speed of the product phase.
3. Ion diffusion rate at the phase interface.

The most commonly used method is the high temperature solid phase reaction method. The required solid raw materials are mixed, ground, and then placed in a crucible and heated for burning. Some reactions require a certain heating and cooling process, and a different atmosphere or vacuum is used. Before burning, the powder can also be pressed into a crucible. This can bring the solid raw materials into close contact to accelerate the reaction.

The method has a simple process and requires only high-temperature furnaces. But the temperature needs to be high. This method has some disadvantages for obtaining high activity and conductivity. On the one hand, because the reactants need to be ground sufficiently for a long time, the obtained sample is highly likely to be contaminated with other impurities. Secondly, since the solid-phase reaction is a multi-phase reaction, the reaction mainly proceeds between the interfaces. The interphase diffusion of ions is restricted by some uncertain factors. Therefore, the composition and structure of the reaction products tend to be non-uniform. Greatly affected the grain conductivity.

(2) Sol-gel method^[11-15]

The sol-gel method is a process developed for the manufacture of glass, ceramics, and many solid materials developed in the mid-1960s. It uniformly mixes and reacts the precursors in the liquid phase to form a stable sol system. Upon standing, it turns into a gel, and the liquid medium contained therein is removed by evaporation or extraction.

The powder prepared by the sol-gel method has the following characteristics:

1. High chemical uniformity. This is because the sol is made from a solution, and the chemical composition between the colloidal particles and the colloidal particles is completely the same;
2. High purity. Like other chemical methods, there are no mechanical steps in the process;
3. Ultra-fine size particles. Colloidal particle size is generally less than-. 1 micron
4. Complex oxide or non-oxide powders can be prepared, and the development prospect is good.

However, this process also has its inherent disadvantages, such as the difficulty to scale up the output, high cost, and strict process requirements.

(3) Co-precipitation method^[16-20]

Coprecipitation is the most common method for synthesizing metal oxide ultrafine powder materials by liquid-phase chemical reaction. It uses various substances dissolved in water to react to form insoluble hydroxides, carbonates, sulphates, acetates, etc. The precipitate is then decomposed by heating to finally obtain the desired compound product. The co-precipitation method can be widely used to synthesize composite oxide ultrafine powder materials. The advantages of this method are:

1. The ultrafine powder material with uniform chemical composition is directly obtained through various chemical reactions in the solution;

2. It is easy to prepare ultrafine powder material with small particle size and uniform distribution.

Preparation of CeO₂ by carbonate co-precipitation is the simplest wet chemical preparation method.

According to the insolubility of the metal carbonate, multiple metal ions in the solution are simultaneously precipitated out by using an excess of carbonic acid precipitant, so that the particles are uniformly mixed in molecular size. In addition, ammonium carbonate or ammonium bicarbonate is used as a co-precipitant, which is not as sensitive to washing and drying as the hydroxide precipitant, and the output is close to 100%. This method has the following advantages:

1. The rare earth metal carbonate is relatively easy to form a solid solution, which ensures a high degree of uniformity of the cations in the precipitation precursor and the final oxide solid solution.

2. The carbonate precursor is non-gelatinous, so that the final powder has a lower degree of agglomeration.

3. By controlling the molar ratio of metal ions and precipitant, spherical particles with regular morphology can be obtained, thereby improving the sintering activity.

2.2 Experiment

We synthesized samples of Ce_{1-x}La_xO_{2-δ} (0 ≤ x ≤ 0.5) using the nanoparticle growth method, which is a type of coprecipitation method^[21]. First, we weighed the starting materials of Ce(NO₃)₃·6H₂O

(purity of 99.99%, manufactured by Wako Pure Chemical Industries, Ltd.) and $\text{La}(\text{NO}_3)_3 \cdot 6\text{H}_2\text{O}$ (purity of 99.0%, manufactured by Wako Pure Chemical Industries, Ltd.) as stoichiometry, and then dissolved them into 100 mL of deionized water. The solution was stirred and heated up to 80 °C. Subsequently, NH_4HCO_3 (purity of 99.99%, manufactured by Kanto Kagaku Co., Ltd.) was weighed and dissolved in 100 ml of deionized water as a precipitating reagent. We next added the reagent dropwise to a metal ion solution to form a precipitate. After aging for 3 h with stirring at 80 °C, the precipitate was collected using filtration. Next, we placed the precipitate in a drying oven at 100 °C overnight to remove the water completely. The dried sample was disintegrated for 15 min using an agate mortar and then fired at 600 °C for 1 h. The calcined sample was disintegrated again and mixed in a rotary ball mill using zirconia balls with ethanol as a medium for 72 h and dried again. The sample was then grinded for 5 min in an agate mortar. After grinding, the sample was pressed into a 13-mm disk pellet uniaxially at a pressure of 30 MPa for 2 min. The pellets were then sintered at 1,500 °C for 5 h in air and the colour of the pellets changed to grey.

2.3 Synthesis of high density sintered compact of $\text{Ce}_{0.9}\text{La}_{0.1}\text{O}_{2-\delta}$

2.3.1 The XRD pattern for different ratio of co-precipitation in synthesis of $\text{Ce}_{0.9}\text{La}_{0.1}\text{O}_{2-\delta}$.

First, we considered about the influence of the ratio between metal ion and precipitating reagent. The amount of the precipitating reagent may affect the size of the particles. We made the samples $\text{Ce}_{0.9}\text{La}_{0.1}\text{O}_{2-\delta}$ that the ratio between metal ion and precipitating reagent as 1:20, 1:15 and 1:5, respectively. Then we prepared the samples for XRD measurements. Figure 2.1 showed the XRD results of all the samples which the ratios between metal ion and precipitating reagent were 1:5, 1:15 and 1:20, respectively. From the XRD pattern, it was confirmed that all samples have a single phase of fluorite type structure.

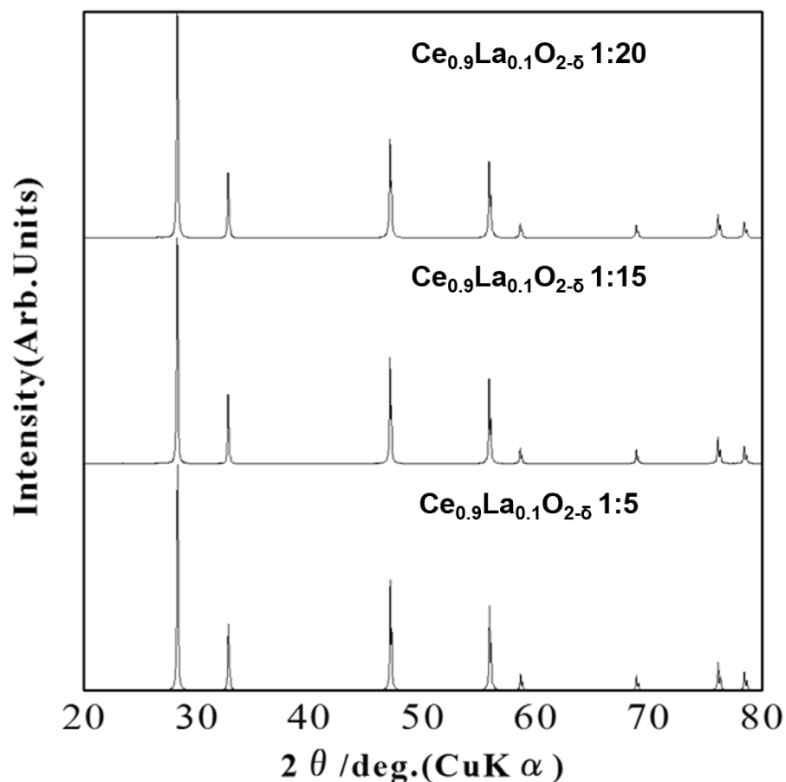


Fig. 2.1 XRD pattern of $\text{Ce}_{0.9}\text{La}_{0.1}\text{O}_{2-\delta}$ after synthesis at 1500 °C for 5 hours, synthesized as the ratio between metal ion and precipitating reagent are 1:20, 1:15 and 1:5, respectively.

Then we calculated the lattice parameters of each samples with different ratios of metal ion and precipitating reagent. And we made the samples in to pellets, sintered at 1500 °C for 5 hours to measure the relative density. Table 1 showed the lattice constants and relative densities of $\text{Ce}_{0.9}\text{La}_{0.1}\text{O}_{2-\delta}$ synthesized at different concentration ratios. The values of these lattice constants were close to the lattice constant 5.4477(4) Å of $\text{Ce}_{0.9}\text{La}_{0.1}\text{O}_{2-\delta}$ in which ICP measurement was previously performed (La content: about 12.5%). In addition, there was no significant difference between our results and the theoretical lattice constant (5.4427 Å) calculated from the ionic radius obtained from the previous report^[22]. It was considered that we synthesized the samples successfully through the co-precipitation method. When the ration was 1:15, the relative density reached to 96.5% which was the highest in all the three conditions. And we could get the conclusion that the ratio of metal ion and precipitating reagent had relationships with the particle

size of our target samples. But how the amount of the precipitating reagent affects the particle size, we still need to search the proof.

	1:20	1:15	1:5
Lattice parameter [\AA]	5.4466(4)	5.4470(4)	5.4453(2)
Relative density [%]	87.9	96.5	90.8

Table 1 Lattice constant and relative density of $\text{Ce}_{0.9}\text{La}_{0.1}\text{O}_{2-\delta}$ after synthesis at $1500\text{ }^{\circ}\text{C}$ for 5 hours, synthesized as the ratios between metal ion and precipitating reagent are 1:5, 1:15 and 1:20, respectively.

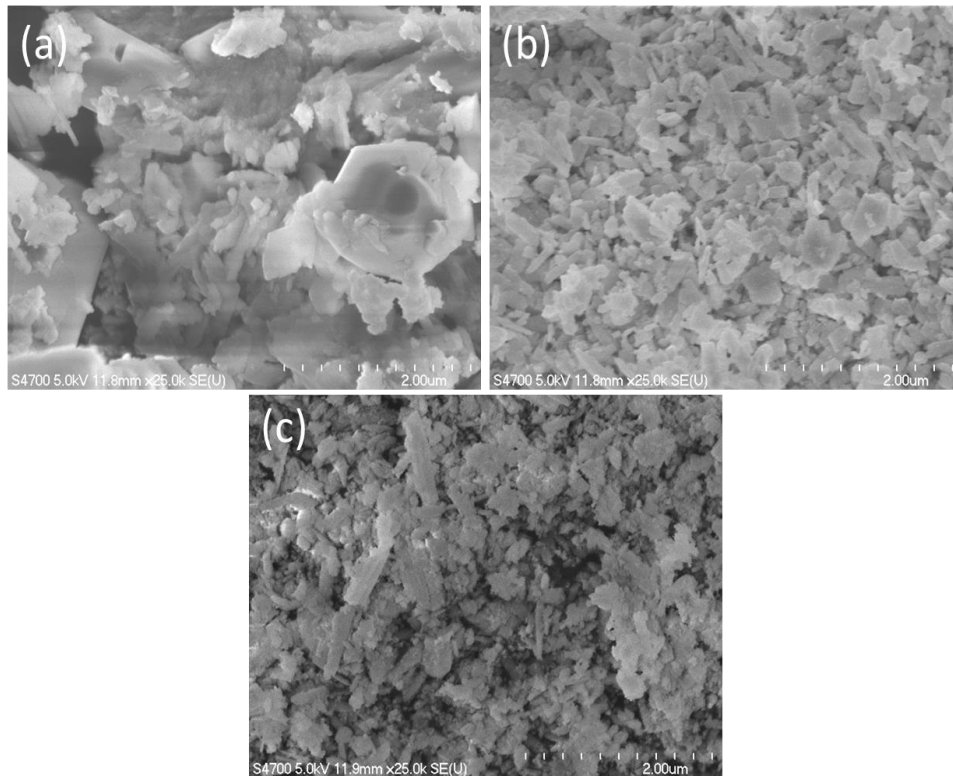


Figure 2.2. The SEM image of $\text{Ce}_{0.9}\text{La}_{0.1}\text{O}_{2-\delta}$ powders synthesized at $600\text{ }^{\circ}\text{C}$ for 1 h as the ratios between metal ion and precipitating reagent were 1:20, 1:15 and 1:5, respectively.

Figure 2.2 was the SEM image of $\text{Ce}_{0.9}\text{La}_{0.1}\text{O}_{2-\delta}$ powders synthesized at 600 °C for 1 h as the ratio between metal ion and precipitating reagent were 1:20, 1:15 and 1:5, respectively. There are usually two factors for the relative density: one is uniform particle diameter, the other is the particle topographical features. We observed the samples with SEM measurement. According to the SEM image, the powder sample of 1:20 ratio with a low raw material concentration had a large particle diameter. The particle diameter and the topographical features were not uniform, either. On the other hand, from 1:15 SEM image, it could be seen obviously that for the powder sample which had a higher raw material concentration than the 1:20 sample, the particle diameter and the topographical features were both uniform. Further, compare with the sample of 1:5, it was confirmed that the particles of 1:15 were more grown uniformly. According to several literatures^[23-25], it is said that the raw material concentration affects the nucleation state, particle size and uniformity the particle topographical features during nucleation process. Basically, the particle diameter is depended on the amount of nuclei generated in the initial stage. As the amount of nuclei decreases, the particle size increases which lead to the quantity of the final product decreases. The amount of nuclei is related to the concentration of urea (precipitant) in solution, and the amount of nuclei increases very early when the concentration of urea is high, according to Ming-Yao Cheng et al. However, they reported that if the concentration of nuclei was too high, the generated nuclei would aggregate together which caused to a larger particle size and ununiform particle topographical features^[26]. However, based on our previous research, we investigated the particle size, presence or absence of agglomeration, and sinter ability by changing the concentration of the precipitant, no significant improvement was observed with the concentration of the precipitant. From this, it was conceivable that the raw material concentration further affected the state at the time of nucleation, the particle diameter, and the aggregation of particles.

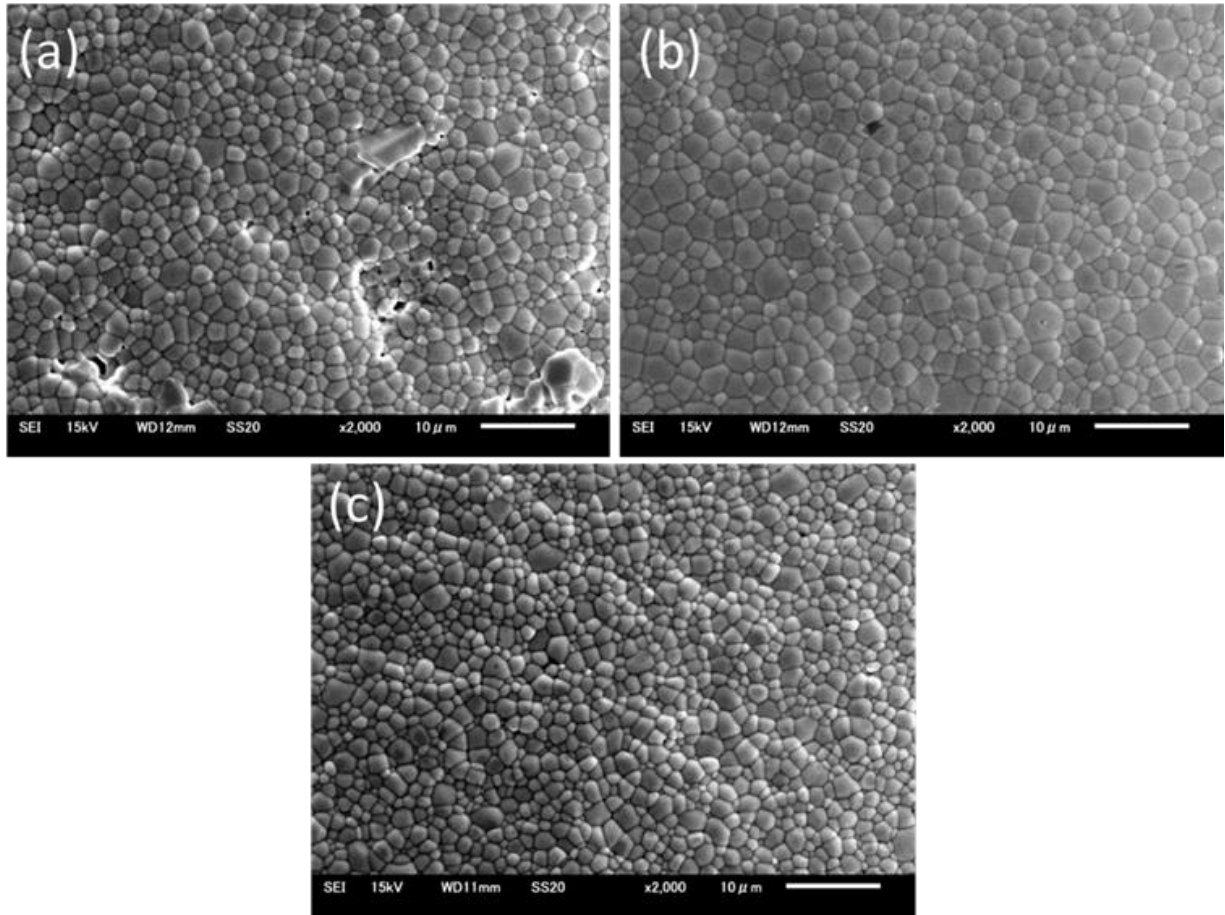


Figure 2.3. The SEM image of $\text{Ce}_{0.9}\text{La}_{0.1}\text{O}_{2-\delta}$ surface synthesized at 1500 °C for 5 h as the ratio between metal ion and precipitating reagent were 1:20, 1:15 and 1:5, respectively.

Figure 2.3 was the SEM image of $\text{Ce}_{0.9}\text{La}_{0.1}\text{O}_{2-\delta}$ surface synthesized at 1500 °C for 5 h as the ratio between metal ion and precipitating reagent were 1:20, 1:15 and 1:5, respectively. From the SEM image of 600 °C, the ununiform of the particle diameter was observed in the calcined particles on the sample surface of 1:20. It could also be observed on the pellet surface after calcining at 1500 °C. In addition, we can see obviously that the vacancies existed on the surface of the calcined pellets surface. There are a large number of pores existed on the 1:5 sample surface as well. We can conclude that the particle size of the calcined particles is related with the starting material concentration. Compared with all the three samples, if the metal ion concentration is high, the particle size will be small. It is considered that the concentration of the raw material affects the

amount of nuclei generated at the time of forming the precipitate. The amount of the nuclei particles has an effect on the presence or absence of particle growth and aggregation during aging process. The size of the obtained particles affects the relative density of the sintered pellets. If the particle size is large, the initial packing density is low when forming into a green body by molding under the pressure, and it is thought that the particles did not sufficiently contact with each other and the sintering process was difficult to proceed. While the particle diameter is small, it is considered that it is easy for the aggregation of the samples due to the particle diameter too small and uniform to aggregate.

Other than the surface of the 1:15 samples, there was no obviously vacancies to be observed. It was considered that a high-density sintered body of 96.5% could be synthesized in the 1:15 sample because small particle size and high uniformity were obtained under this condition. We made all samples under this kind of conditions in the bellow experiments.

2.3.2 Structural change with La doping of $Ce_{1-x}La_xO_{2-\delta}$

Figure 2.4 was the XRD patterns of $Ce_{1-x}La_xO_{2-\delta}$ ($x = 0-0.5$) fired at 1500 °C. From the XRD patterns, all samples showed a fluorite-type structure with La dopant increasing, and there was no second phase in all the XRD patterns. The lattice constants of each samples which were calculated from the XRD peak, apparently increased with the increase of the La doping amount. But it did not follow the Vegard rule and showed a non-linear tendency after $x = 0.3$. The value was shown in Figure 2.5. This was also apparent to compare with the lattice constant obtained by theoretical calculation^[22]. From figure 2.5, it was conceivable that in the state ($x = 0.3, 0.4, 0.5$), although the structure change could not be observed in the XRD pattern, a structural change had occurred. Further, assuming that a structural change had occurred, the reason why a structure change peak did not appear in the XRD pattern was considered as follows.

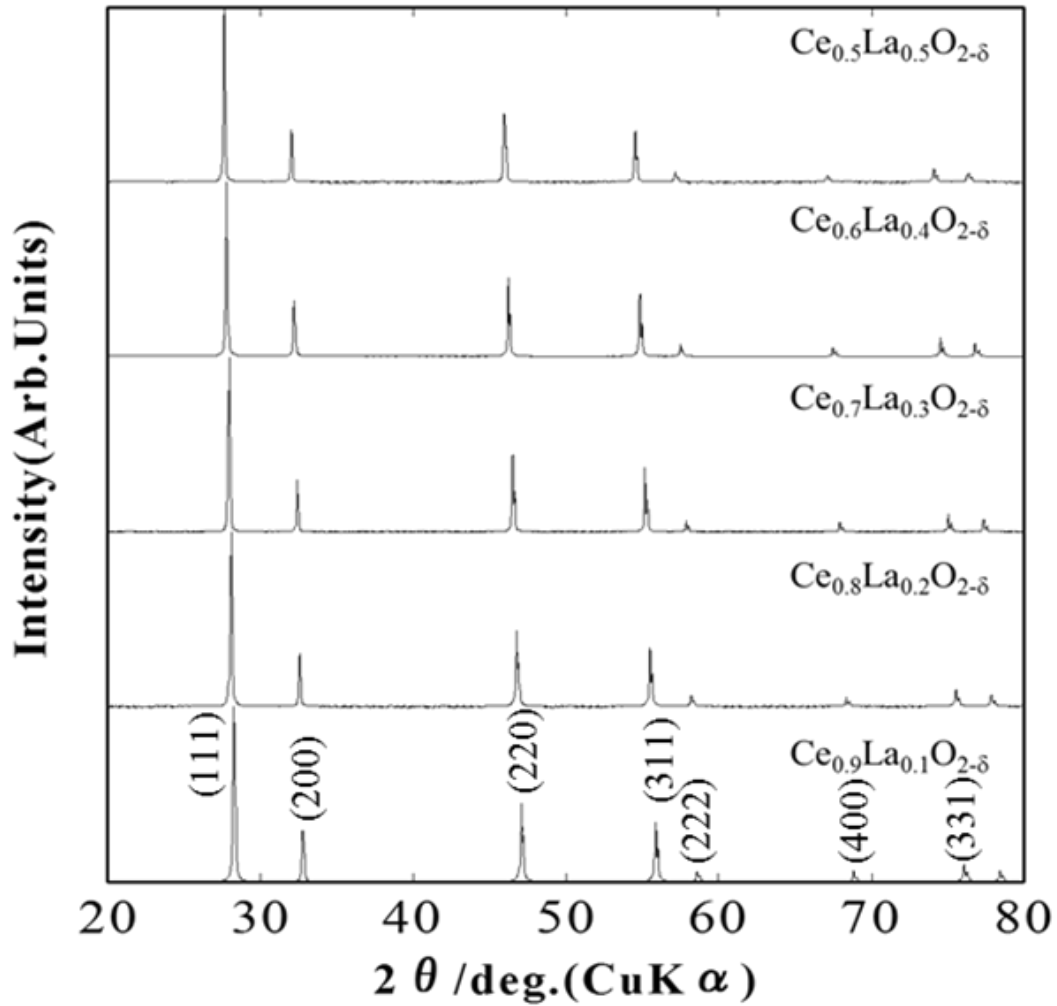


Figure 2.4 XRD patterns of $\text{Ce}_{1-x}\text{La}_x\text{O}_{2-\delta}$ ($x = 0-0.5$) fired at 1500 °C for 5 h.

The peak in the XRD shows a peak peculiar to the substance depending on what basic structure the lattice of the substance has and what kind of atoms are included. At this time, the crystal scattering factor is used to determine the presence or absence of a peak, and is represented by the following equation (2.1).

$$F = f \times \sum e^{2i\pi \times (hu + kv + lw)} \dots \dots \dots (2.1)$$

In this equation, the index of the peak to be obtained, information of the atomic position, and the atom scattering factor (having a value substantially equal to the atomic number) represented by f are substituted. If the value does not become 0, the peak exists. Otherwise the peak will disappear.

This is called the extinction law^[27]. For example, since a peak due to superlattice reflection exists on the (110) plane as a peak specific to the pyrochlore type, the F value is calculated using equation (2.1). Here, in this example, LaO-doped CeO₂ was used, but the atomic number of La and Ce changed by only one, and as a result, the F value was infinitely close to 0. It is probable that the peak of the (110) plane was not confirmed.

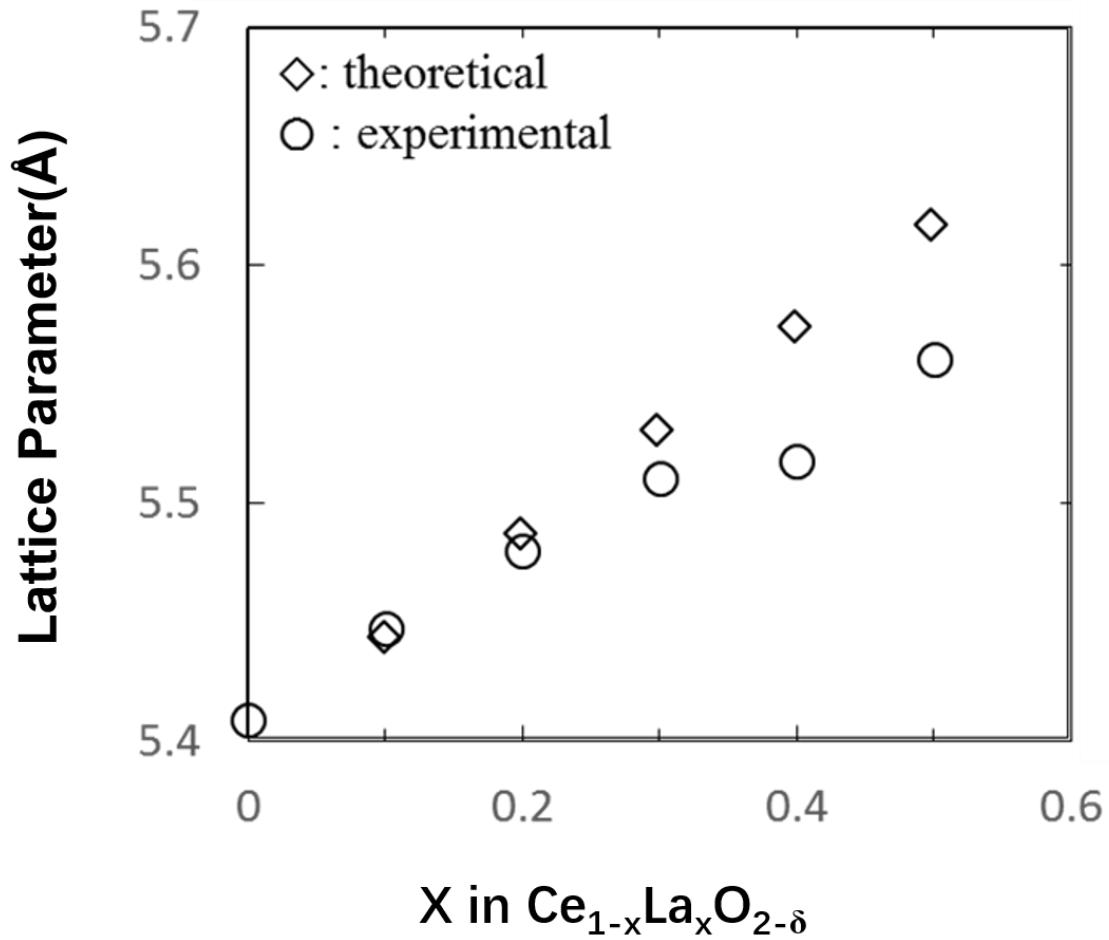


Fig. 2.5 Lattice constant of Ce_{1-x}La_xO_{2-δ} (x = 0-0.5) fired at 1500 °C for 5 h.

2.4 Conclusion.

In this part of work, we synthesized the $Ce_{1-x}La_xO_{2-\delta}$ ($x = 0.1 \sim 0.5$) samples with the co-precipitation method. First we researched about the starting conditions about the ratio between metal ion and precipitating reagent were 1:20, 1:15 and 1:5, respectively. We could see with three kinds of conditions, the XRD had no difference about the final products. But the relative densities were different with the amount of the starting materials. Then we used the SEM measurement to check about the surface of the powders sintered at 600 °C for 1h and pellets sintered at 1500 °C for 5 h, respectively. We could conclude that, with the powders sintered at 600 °C for 1h, the powder sample of 1:20 ratio with a low raw material concentration had a large particle diameter and the particle diameter and the topographical features were not uniform, either. It could be seen obviously that for the 1:15 powder sample, the particle diameter and the topographical features were both uniform. Further, compared with the samples of 1:5, the 1:15 powder sample was also that the particles were grown more uniformly. To the pellets sintered at 1500 °C for 5 h, on the sample surface of 1:20, the ununiform of the particle diameter was observed. In addition, we could see obviously that the vacancies existed on the surface of the calcined pellets surface. There were a large number of pores existed on the 1:5 sample surface as well. As the 1:15 pellets, the particle size was uniform and there was no obviously pores on the surface. We could conclude that the particle size of the calcined particles was related with the starting material concentration and the best condition is 1:15 about the ratio of metal ion and precipitating reagent.

Then we synthesized the $Ce_{1-x}La_xO_{2-\delta}$ ($x = 0.1 \sim 0.5$) samples under this condition. We measured the XRD. We could see that all the samples appeared a single phase in the XRD patterns. But when we calculated the lattice parameters of each sample, the experimental data was not fit with the theoretical one. So we suspected that there was a structure change at $x=0.3$ of $Ce_{1-x}La_xO_{2-\delta}$ ($x = 0.1 \sim 0.5$) samples. It would be researched in the work below.

Reference

- [1] Anthony R. West, Wiley and Sons, 2005.
- [2] B. Gerand, G. Nowogrocki, J. Guenot, M. Figlarz, Academic press.
- [3] Lev N. Sidorov, in Encyclopedia of Spectroscopy and Spectrometry, 1999, Pages 915-923.
- [4] P.G. Jambrina, J. Aldegunde, in Computer Aided Chemical Engineering, Volume 39, 2016, Pages 583-648.
- [5] Bangwei Zhang, in Physical Fundamentals of Nanomaterials, 2018.
- [6] P. Duran, J. Tartaj, F. Capel, C. Moure, Journal of the European Ceramic Society 24 (2004) 2619–262.
- [7] Tatsuya Kawada, Natsuko Sakai, Harumi Yokokawa, Masayuki Dokiya, Iwao Anzai, Solid State Ionics, Volume 50, Issues 3–4, 1992, 189-196.
- [8] R.C. Olegário et al. , Dyes and Pigments, 106, (2014), 14-19.
- [9] L. Lei, L.L. Zhang , Matter and Radiation at Extremes, 3, (2018), 95-103.
- [10] C. Sun, U. Stimming, Journal of Power Sources, 171, (2007), 247–26.
- [11] Hench, L. L, J. K. West, Chemical Reviews, (1990), 90: 33–72.
- [12] Klein, L, Springer Verlag. (1994).
- [13] Klein, L.C. and Garvey, G.J., Journal of Non-Crystalline Solids, Vol. 38, (1980), p.45
- [14] Brinker, C.J., et al., J. Non-Crystalline Solids, Vol.48, 1982, p.47.
- [15] Einstein, A., Ann. Phys., Vol. 19, p. 289 (1906), Vol. 34, 1911, p.591.
- [16] A.-H. Lu, E. L. Salabas and F. Schüth, Angew. Chem. Int. Ed., 2007, 46,1222–1244.
- [17] Otto Hahn, Cornell University Press, Ithaca, New York, USA, 1936.
- [18] Patnaik, P. Dean's Analytical Chemistry Handbook, 2nd ed. McGraw-Hill, 2004.
- [19] Alan Townshend and Ewald Jackwerth, Pure & App. Chem., Vol.61, No.9, pp. 1643-1656, 1989.
- [20] Harvey, D. Modern Analytical Chemistry. McGraw-Hill, 2000.
- [21] B. Ravel and M. Newville, J. Synchrotron Rad., 12 (2005) 537–541.
- [22] Toshihiro Moriga, et al, Solid State Ionics 31 (1989) 319-328.

- [23] Seong Jae Hong and Anil V. Virkar, *J. Am. Ceram. Soc.*, 78 (1995) 433-439.
- [24] Messing GL, Hirano S, Hausner H. *Ceramic Powder Science III*, vol.12. Westerville: American ceramic society; 1990. p. 129–36.
- [25] Min-Young Cho, et al, *Materials Letters* 64(2010), 323-326.
- [26] Zhigang Liu, et al, *Journal of Natural Gas Chemistry* 19, (2010), 313-317.
- [27] Hideo Nagashima, *J. Mine. Soc. Jpn.* 6(3), (1963), 175-184.

Chapter 3: Local structure changes of $\text{Ce}_{1-x}\text{Ln}_x\text{O}_{2-\delta}$ (Ln = La, Gd)

solid electrolytes

3.1 Introduction

X-ray absorption fine structure (XAFS) spectroscopy is one of the most powerful tools for describing local structures. In this technique, we adjust the X-ray energy to be consistent with the internal electron layer in the element under study, then use it to detect the sample, and then monitor the amount of X-ray absorption as a function of its energy^[1-3]. If sufficient accuracy is used, the spectrum will show small oscillations, which is the result of the influence of the local environment on the basic absorption probability of the target element. From the spectrum, we can also get the distance between the absorbing atoms and neighboring atoms, the number and type of these atoms, and the oxidation state of the absorbing elements. These are the parameters that determine the local structure. By selecting X-rays of different energies, we can obtain such information for all elements in the sample^[4,5].

When the energy of the X-rays resonates with the energy of an element inner electron shell in the sample, a sudden rise in electrons occurs and the electron is excited to form a continuous spectrum. Due to the shape of the spectrum, this spectrum is also called the absorption edge. In most cases, the absorbing edges are separated, and the target element is simply selected by scanning a suitable energy range. Along the absorption edge, as the X-ray energy increases, the absorption rate decreases monotonically as the penetration depth of the X-ray becomes larger. As the spectrum is expanded across a particular edge, fine structures are observed^[7,8]. The X-ray absorption near-side structure (XANES) region appears when the spectral peaks and shoulders that are more than 20 to 30 electron volts wide pass through the start of the edge. The fine structure on the high energy side of the edge where the energy decays to several hundred electron volts is called X-ray absorption fine structure (XAFS). The fine structure in XANES and XAFS has been studied thoroughly, which enables XAFS to be used to determine the type and local structure of chemical substances^[9].

Outside the edge region, the XAFS fine structure is superimposed in the form of a series of undulating oscillations on the smoother absorption curve that should be isolated atoms. These fine structures are formed due to interference between ionized photoelectron waves and backscattered waves of some of these waves from neighboring atom pairs. With the change of the X-ray energy, the interference conditions also change correspondingly, causing adjacent atoms to produce an oscillating fine structure.

XAFS includes two technologies, EXAFS and XANES. EXAFS is an oscillation of the element's X-ray absorption coefficient in the range of 30-1000 eV on the high energy side of the absorption side. The generation of EXAFS is related to the scattering of absorbing atoms and other atoms around it, that is, they are all related to structure. Therefore, by measuring EXAFS, we can study the neighbor structure around the absorbing atoms, and get the parameters such as atomic distance, coordination number, atomic mean square displacement, etc. The main feature of EXAFS method is that it can measure different kinds of atoms separately, give the neighbor structure of specified element atoms, and also distinguish the types of neighbor atoms^[10-12]. The strong X-ray source can also be used to study the neighbor structure of atoms with very little content, and it can be used for both ordered and disordered substances. In this way, EXAFS can be used to solve some material structure problems that are difficult or impossible to solve by other methods.

EXAFS has the following characteristics:

- 1) EXAFS depends on short-range ordering and does not rely on long-range ordering, so it can measure a wide range of samples, which can be used for amorphous, liquid, molten, catalyst active centers, metal proteins, and impurity atoms in crystals. Structural research
- 2) The X-ray absorption edge has elemental characteristics. For atoms of different elements in the sample, the atomic neighboring structure of different elements in the same compound can be studied by adjusting the incident X-ray energy;
- 3) Fluorescence can be used to measure samples with concentrations as low as one part per million;
- 4) Polarized X-rays can be used to measure atomic bond angles in oriented samples, and can measure surface structure.

5) Sample preparation is relatively simple and no single crystal is required. When the experimental conditions are available, the data collection time is relatively short, and it usually takes only a few minutes to measure a spectral line with a synchrotron X-ray source.

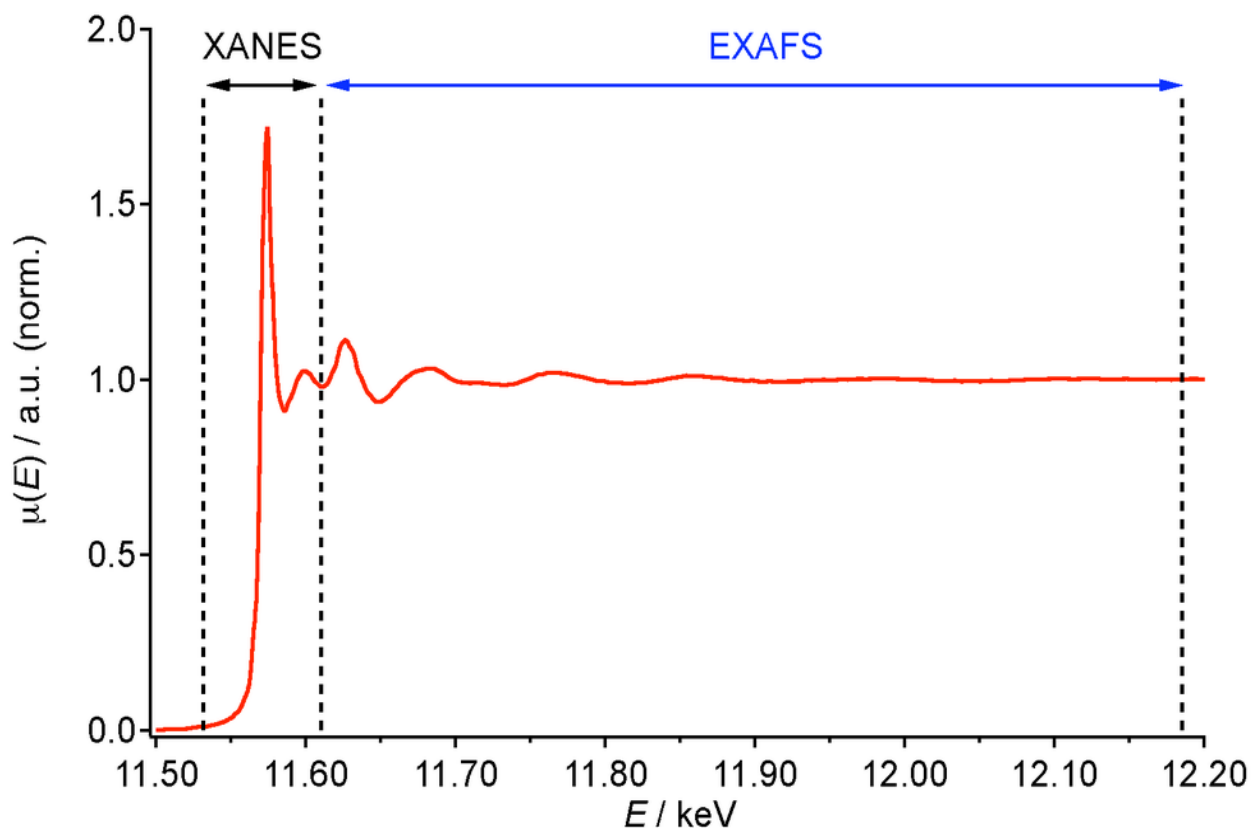


Figure 3.1 Representative EXAFS absorption spectrum^[13].

3.2 XAFS measurement and analysis

3.2.1 The preparation of XAFS samples

We synthesized samples of $\text{Ce}_{1-x}\text{La}_x\text{O}_{2-\delta}$ ($0 \leq x \leq 0.5$) for XAFS measurements using the nanoparticle growth method, which was the same coprecipitation method as above^[19]. First, we weighed the starting materials of $\text{Ce}(\text{NO}_3)_3 \cdot 6\text{H}_2\text{O}$ (purity of 99.99%, manufactured by Wako Pure Chemical Industries, Ltd.) and $\text{La}(\text{NO}_3)_3 \cdot 6\text{H}_2\text{O}$ (purity of 99.0%, manufactured by Wako Pure Chemical Industries, Ltd.) by stoichiometry ratio, and then dissolved them into deionized water 100 ml. Then

we kept the solution stirred at 80 °C. We next added the reagent which was NH_4HCO_3 (purity of 99.99%, manufactured by Kanto Kagaku Co., Ltd.) weighed and dissolved into 100 ml deionized water to the solution drop by drop. After 3 h stirring, the precipitate was collected using filtration. Next, we dried the precipitate at 100 °C overnight to remove the water completely. The dried sample was disintegrated for 15 min and then fired at 600 °C for 1 h. The calcined sample was disintegrated again and took a ball milling method with ethanol as a medium for 72 h and dried again. The sample was then grinded for 5 min. After grinding, the sample was pressed into a 13-mm disk pellet uniaxially at a pressure of 30 MPa for 2 min. The pellets were then sintered at 1,500 °C for 5 h in air and the colour of the pellets changed to grey.

Synthesis for Gd-doped CeO_2 powder $\text{Ce}_{1-x}\text{Gd}_x\text{O}_{2-\delta}$ ($0 \leq x \leq 0.5$) was also carried out by the same procedure. The change of starting material is $\text{Gd}(\text{NO}_3)_3 \cdot 6\text{H}_2\text{O}$ (Wako Pure Chemical Industries, Ltd., 99.95% or higher purity).

3.2.2 The XAFS experiment

XAFS measurements of La- and Gd-doped ceria were conducted at the BL16B2 beamline of the Spring-8 synchrotron facility in Japan. An asprate amount of doped ceria was mixed with hexagonal boron nitride powder and pressed into a 10-mm pellet uniaxially for measurement. XAFS spectra near the Ce K-edge (40.45 keV), La K-edge (38.94 keV), and Gd K-edge (50.24 keV) were measured using transmission mode at room temperature. In addition, CeO_2 , La_2O_3 , and Gd_2O_3 were measured as reference samples. An X-ray was monochromatized using a Si(311) double-crystal monochromator. A cylindrical Rh-coated mirror was used for elimination of the higher harmonics. Ionization chambers were filled with Ar-diluted Kr gas (Ar:Kr = 75:25) for measuring the incident X-ray and pure Kr gas for the transmitted X-ray, respectively.

The XAFS spectra were analyzed for both the first and second neighbor shells. Athena was used as the analysis software for the XAFS oscillation extraction, and Artemis was used for the curve-fitting of the XAFS oscillation^[46]. The XAFS analysis conditions and parameters obtained are summarized in Tables 1 and 2, respectively. The k-range used for obtaining the radial distribution functions for each absorbing atom (in Figure 4) was basically fixed from 3 to 13 \AA^{-1} . Curve-fitting

was applied against the r-range from roughly 1.4 to 2.1 Å for the first-neighbors and from 2.8 to 4.1 Å for the second-neighbors, respectively.

When we analyzed the distance between La absorbing atoms in the second neighbor shell, we assumed that the distances are mainly composed of two types of coordination. One is La-La and the other is La-Ce. Because La is larger in ionic radius than Ce, of course, when the two types of bond distance are obtained in the second neighbor shell, the longer one is attributable to La-La and the shorter one is attributable to La-Ce, and the coordination number by either La or Ce will be distributed according to the cation composition. In a similar manner, the constitution of the two types of coordination in the second neighbor of Ce and Gd as the absorbing atoms was assumed based on the fact that the ionic radius decreases in the following way: La³⁺ (1.16 Å in 8-fold coordination), Ce⁴⁺ (1.143 Å in 8-fold coordination), and Gd³⁺ (1.053 Å in 8-fold coordination)^[47].

			N	S02	E0	R	δ2	R-factor
LDC	La K-edge	0	8	1.816±0.368	-9.439±2.840	2.353±0.014	0.008±0.002	0.0041
		0.1	8	1.627±0.360	-5.625±2.895	2.458±0.018	0.008±0.002	0.010
		0.2	8	1.729±0.238	-6.421±1.781	2.463±0.012	0.010±0.001	0.0036
		0.3	8	1.739±0.242	-3.687±1.794	2.463±0.013	0.011±0.002	0.0035
		0.4	8	1.562±0.349	-7.387±2.880	2.460±0.020	0.011±0.002	0.0087
	0.5	8	1.440±0.312	-8.690±2.822	2.450±0.019	0.011±0.002	0.0084	
	Ce K-edge	0	8	1.816±0.368	-9.439±2.840	2.353±0.014	0.008±0.001	0.0041
		0.1	8	1.794±0.211	-7.533±1.656	2.339±0.009	0.010±0.001	0.0029
		0.2	8	1.715±0.228	-9.890±1.932	2.318±0.011	0.011±0.001	0.0015
		0.3	8	1.686±0.254	-15.280±2.192	2.295±0.011	0.011±0.001	0.0018
0.4		8	1.677±0.246	-11.889±2.195	2.285±0.012	0.012±0.001	0.0017	
				-12.497±1.750	2.268±0.009	0.012±0.001	0.0010	
			N	S02	E0	R	Δ2	R-factor
GDC	Gd K-edge	0	8	1.810±0.368	-9.439±2.840	2.353±0.014	0.008±0.001	0.0041
		0.1	8	1.326±0.546	-1.318±5.231	2.391±0.032	0.010±0.004	0.0227
		0.2	8	1.342±0.439	-2.259±4.269	2.364±0.024	0.008±0.003	0.0154
		0.3	8	1.261±0.422	-10.150±4.527	2.350±0.023	0.007±0.002	0.0119
		0.4	8	1.173±0.436	-11.505±5.089	2.348±0.026	0.007±0.003	0.0060
	0.5	8	1.051±0.449	-5.034±5.689	2.341±0.030	0.006±0.003	0.0082	
	Cd K-edge	0	8	1.816±0.368	-9.439±2.840	2.353±0.014	0.007±0.001	0.0041
		0.1	8	1.354±0.630	-0.992±5.832	2.394±0.037	0.001±0.004	0.0283
		0.2	8	1.342±0.439	-2.259±4.269	2.364±0.024	0.008±0.003	0.0154
		0.3	8	1.272±0.385	0.008±0.003	2.351±0.021	-9.951±3.997	0.0127
0.4		8	1.183±0.269	-11.575±3.052	2.348±0.015	0.007±0.002	0.0072	
0.5	8	1.090±0.309	-5.099±3.761	2.341±0.019	0.007±0.002	0.0118		

Table 1 XAFS analysis condition and obtained parameters of 1st shell for LDC and GDC.

	absorbing atom	scattering atom	composition	N	S02	E0	R	$\delta 2$	R-factor	
LDC	La	La	0	0	-	-	-	-	-	
			0.1	1.2	5.832±3.991	-49.165±6.650	3.972±0.017	0.003±0.001	0.008	
			0.2	2.4	14.899±15.547	5.366±7.731	3.957±0.118	0.026±0.016	0.004	
			0.3	3.6	8.805±3.609	-12.316±9.656	3.964±0.008	0.006±0.001	0.065	
			0.4	4.8	4.154±2.106	-12.411±4.260	3.960±0.004	0.008±0.001	0.021	
			0.5	6	7.392±5.333	-3.448±4.739	3.940±0.026	0.012±0.003	0.006	
		Ce	0	12	-	-	-	-	-	-
			0.1	10.8	3.274±1.704	-3.152±4.166	3.896±0.041	0.013±0.004	0.008	
			0.2	9.6	2.087±0.594	-12.290±2.476	3.853±0.008	0.007±0.001	0.004	
			0.3	8.4	5.621±19.455	-1.958±6.211	3.873±0.136	0.006±0.009	0.065	
			0.4	7.2	3.914±14.503	-5.005±3.465	3.865±0.146	0.008±0.012	0.021	
			0.5	6	3.229±3.688	8.409±7.695	3.862±0.025	0.010±0.003	0.006	
	Ce	La	0	0	-	-	-	-	-	
			0.1	1.2	3.274±1.704	0.225±28.297	3.896±0.041	0.013±0.004	0.012	
			0.2	2.4	2.087±0.594	-21.314±37.558	3.853±0.008	0.007±0.001	0.024	
			0.3	3.6	5.621±19.455	-11.137±50.831	3.873±0.136	0.006±0.009	0.024	
			0.4	4.8	3.914±14.503	-8.246±54.036	3.865±0.146	0.008±0.012	0.034	
			0.5	6	3.229±3.688	-9.076±10.291	3.862±0.025	0.010±0.003	0.030	
		Ce	0	12	-	-	-	-	-	-
			0.1	10.8	1.653±1.124	-13.039±1.960	3.837±0.015	0.006±0.002	0.012	
			0.2	9.6	2.109±3.069	-11.077±7.629	3.833±0.036	0.009±0.002	0.024	
			0.3	8.4	0.707±5.883	0.172±126.236	3.786±0.289	0.003±0.019	0.024	
			0.4	7.2	0.719±6.541	3.039±143.315	3.783±0.281	0.004±0.022	0.034	
			0.5	6	1.119±1.508	1.009±21.066	3.781±0.039	0.006±0.003	0.030	
GDC	Gd	Gd	0	0	-	-	-	-	-	
			0.1	1.2	40.625±55.241	-2.001±9.770	3.993±0.072	0.011±0.006	0.003	
			0.2	2.4	5.427±12.783	0.978±11.823	3.925±0.072	0.006±0.013	0.004	
			0.3	3.6	4.221±7.813	-7.049±12.120	3.906±0.047	0.007±0.009	0.004	
			0.4	4.8	7.181±5.059	-7.058±5.608	3.850±0.060	0.018±0.011	0.110	
			0.5	6	0.994±0.840	-44.575±8.590	3.838±0.033	0.005±0.003	0.067	
		Ce	0	12	-	-	-	-	-	-
			0.1	10.8	3.719±4.318	7.079±7.892	3.881±0.047	0.009±0.005	0.003	
			0.2	9.6	1.074±2.815	6.818±12.947	3.830±0.080	0.004±0.013	0.004	
			0.3	8.4	1.737±3.509	0.048±10.131	3.806±0.049	0.006±0.010	0.004	
			0.4	7.2	0.697±0.517	1.888±11.298	3.794±0.041	0.007±0.003	0.110	
			0.5	6	0.963±0.889	1.942±7.438	3.810±0.043	0.013±0.007	0.067	
	Ce	Gd	0	0	-	-	-	-	-	
			0.1	1.2	3.719±4.318	-5.023±10.177	3.881±0.047	0.009±0.005	0.010	
			0.2	2.4	1.074±2.815	-32.092±21.350	3.830±0.080	0.004±0.013	0.021	
			0.3	3.6	1.737±3.509	-43.570±18.188	3.806±0.049	0.006±0.010	0.089	
			0.4	4.8	0.697±0.517	31.930±4.399	3.794±0.041	0.007±0.003	0.003	
			0.5	6	0.963±0.889	35.886±4.837	3.810±0.043	0.013±0.007	0.002	
		Ce	0	12	-	-	-	-	-	-
			0.1	10.8	1.383±0.351	-15.586±2.314	3.832±0.006	0.005±0.001	0.010	
			0.2	9.6	1.949±0.374	-11.336±2.178	3.817±0.011	0.007±0.001	0.021	
			0.3	8.4	2.187±0.656	-20.524±3.895	3.777±0.021	0.008±0.001	0.089	
			0.4	7.2	0.995±0.437	-13.686±2.630	3.772±0.019	0.006±0.001	0.003	
			0.5	6	1.154±0.321	-13.529±2.406	3.743±0.012	0.006±0.001	0.002	

Table 2 XAFS analysis condition and obtained parameters of 2nd shell for LDC and GDC.

3.3 Results and discussion

3.3.1 The local structure change of LDC and GDC

According to a previous report, the solubility limit of Gd in the fluorite type structure was within the compositional range of $0.4 < x < 0.5$ ^[22]. It was also demonstrated that peaks assigned to the rare earth oxide C-type Gd_2O_3 appear when x reached 0.5. As shown in the powder X-ray diffraction patterns for $Ce_{1-x}La_xO_{2-\delta}$ ($0 \leq x \leq 0.5$), LDC and $Ce_{1-x}La_xO_{2-\delta}$ ($0 \leq x \leq 0.5$), and GDC, however, no impurities were contained in these samples. One possible reason for the difference is due to the difference in the firing temperature. The GDC samples used in this experiment were fired at 1,500 °C, whereas those in the report were fired at 1,300 °C. The higher temperature leads

to a more disordered atomic arrangement in the lattice, and the C-type structure can be considered as the superstructure of the fluorite type structure. The oxygen deficiency might be affected by the firing temperature as well.

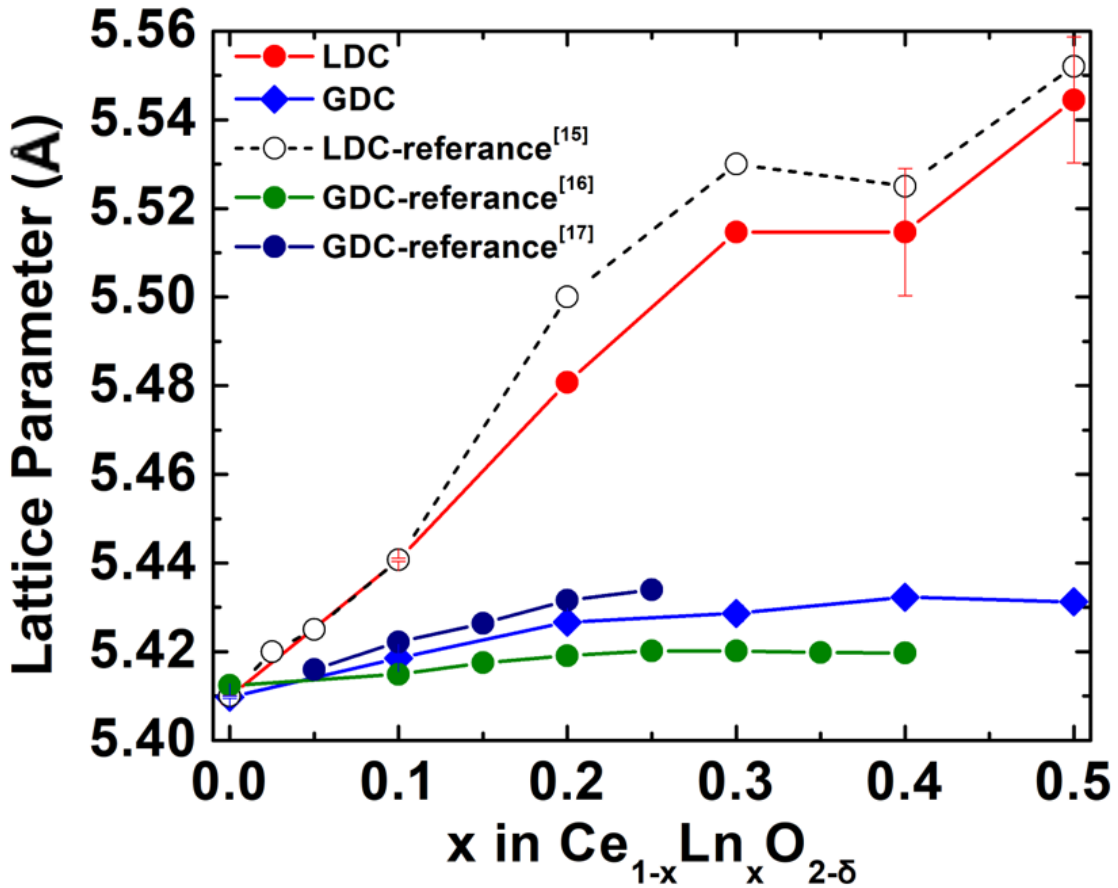


Figure 3.1 The lattice parameters of $Ce_{1-x}Ln_xO_{2-\delta}$ ($Ln=La, Gd$) ($0 \leq x \leq 0.5$).

Figure 3.1 showed the lattice parameters of the LDC and GDC with an increasing doping amount of La and Gd, respectively. For both LDC and GDC, the lattice parameters increased gradually with the amount of doped Ln. The changes in the lattice parameters in LDC were obvious and larger than those of the lattice parameters in the GDC. In the curve of the lattice parameters in the LDC, the trend of change as a function of x was similar with the previously reported results^[23], although the values were somewhat different. Interestingly the lattice constants increased linearly with an increase in x but with a bend point at x = 0.4. Thus, we considered that there was a drastic

structural change in the composition between $x = 0.3$ and $x = 0.4$ in LDC.

For GDC, the increase in the lattice parameters with an increase in the doping amount was not as obvious as in LDC. In the curve of the lattice parameters in GDC, the trend of change in the value was similar with previously reported results [23, 24]. The change was extremely smooth, and no abrupt changes in the compositional dependence of the lattice parameters were detected. Our data were between the results of the previous studies, which supports their correctness. Some previous results had reported that the local structure changes from a fluorite type structure to a rare earth C-type structure with $x \geq 0.4$ [22]. From this, we considered that there may be different structural changes in the LDC and GDC.

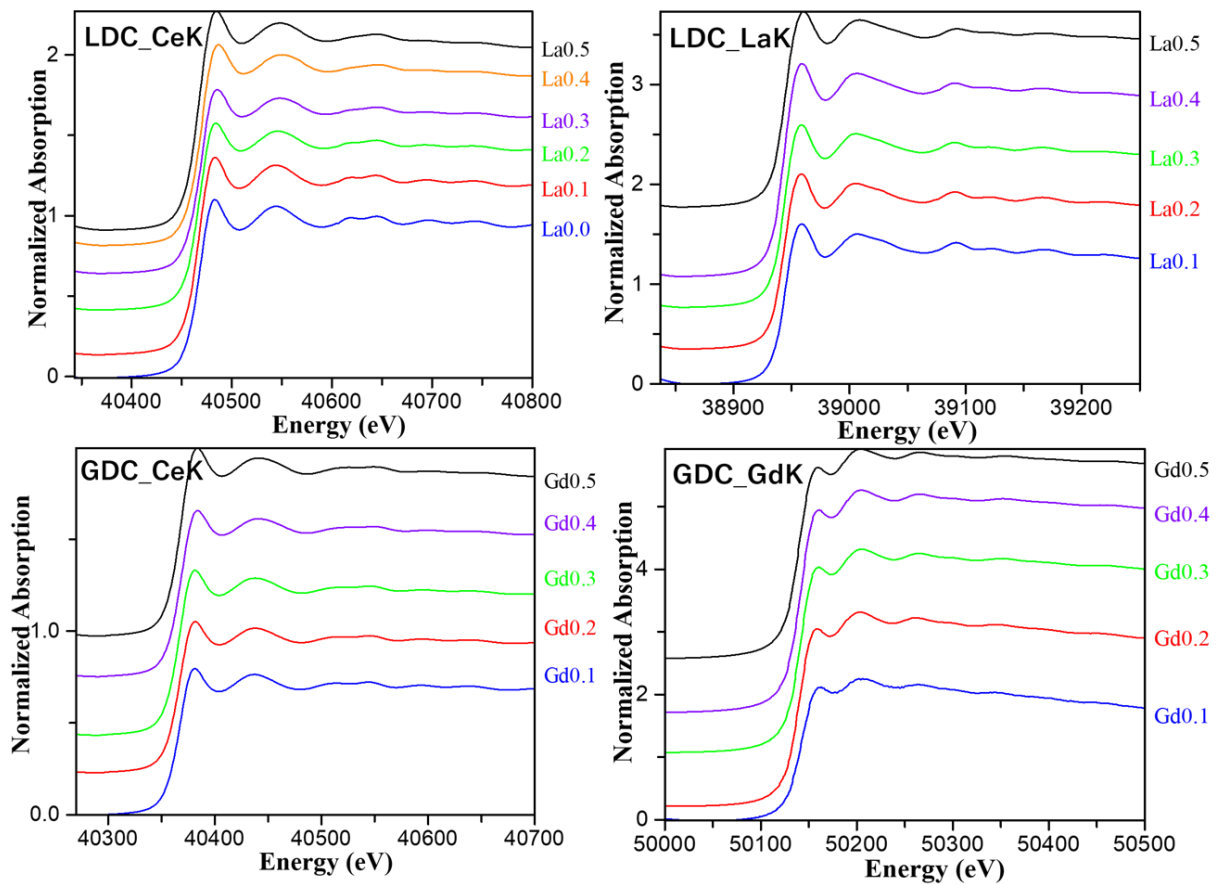


Figure 3.2 The EXAFS spectra near the CeK, LaK and GdK of $Ce_{1-x}La_xO_{2-\delta}$ and $Ce_{1-x}Gd_xO_{2-\delta}$.

Figure 3.2 showed the absorption spectra near the Ce K absorption edge and the La K absorption

edge in the LDC, and those near the Ce K absorption edge and Gd K absorption edge in the GDC. The energy of the absorption edge is related to the electronic state of the X-ray absorbing cations. From the Ce K spectra in the LDC and GDC, we could see that the peak position of the absorption edge was not clearly changed with an increase in the amount of dopant. This indicated that in both LDC and GDC, most of the CeO₂ valence was 4+ and was not changed to 3+ as the amount of Ln doping increases. The structural change was not caused by the change in Ce valence. Nolan claimed that a reduction of Ce⁴⁺ to Ce³⁺ in La-doped CeO₂ was preferably caused by the introduction of La³⁺[25]. However, neither a peak shift nor a change in shape was observed in the spectra.

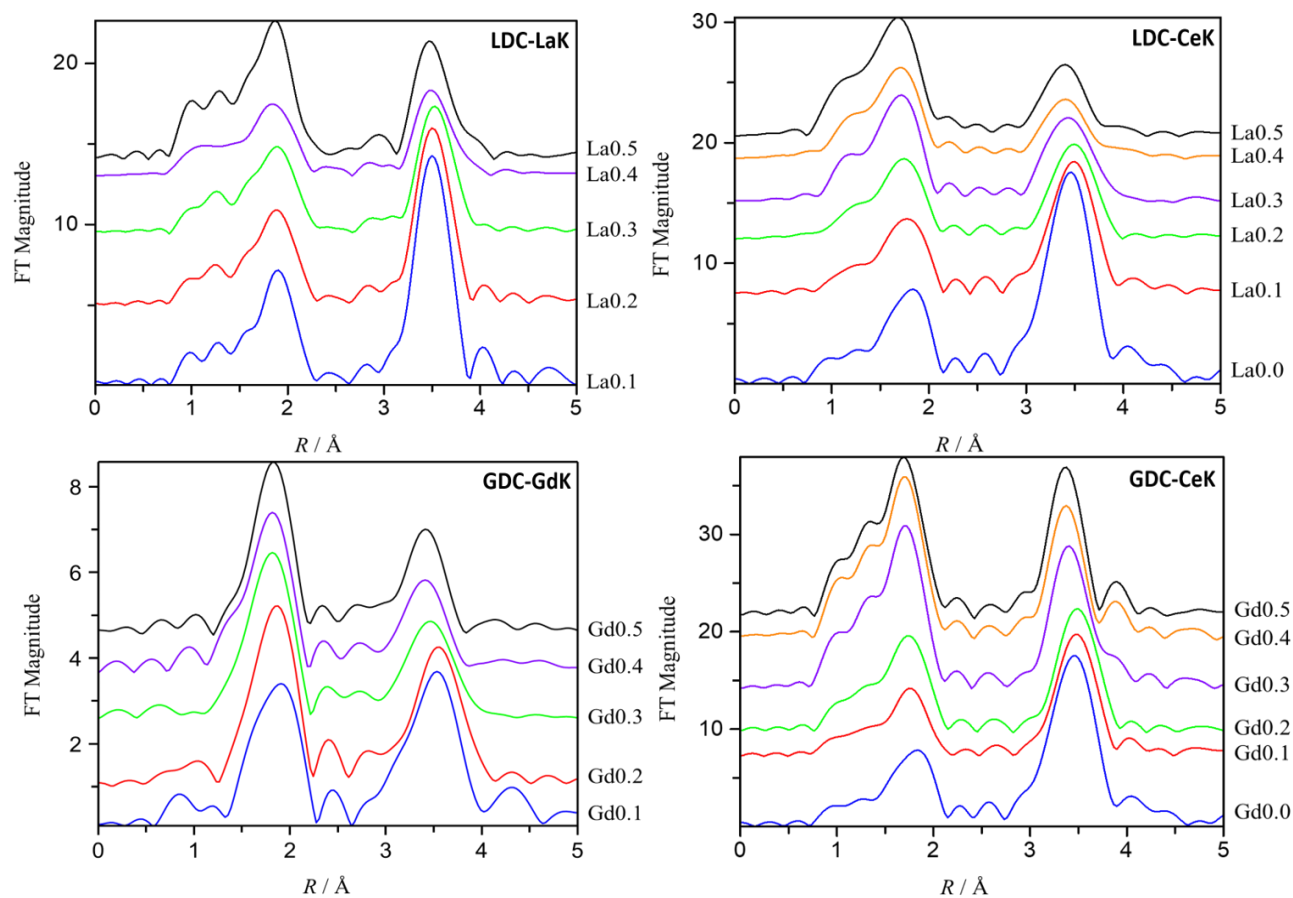


Figure 3.3 Fourier transforms (FTs) of k₃-weighted EXAFS oscillation of LDC and GDC.

Figure 3.3 showed the peaks of the radial structural functions of the Ce K absorption edge and La K absorption edge in LDC, and the Ce K absorption edge and Gd K absorption edge in GDC. In LDC, the peak representing the first close distance of the Ce K absorption edge graph shifted to the left as the La doping amount increased, and the peak of the second proximity distance also shifted slightly to the left. By contrast, the graph of the La K absorption edge showed almost no change in position even when the La doping amount increased. This suggested that the coupling length around the Ce decreased and that the coupling length around the La did not change. However, in GDC, all peaks of the Ce K absorption edge and Gd K absorption edge shifted to the left as the amount of Gd doping increased. From this result, it was conceivable that the coupling lengths around the Ce and Gd all decreased.

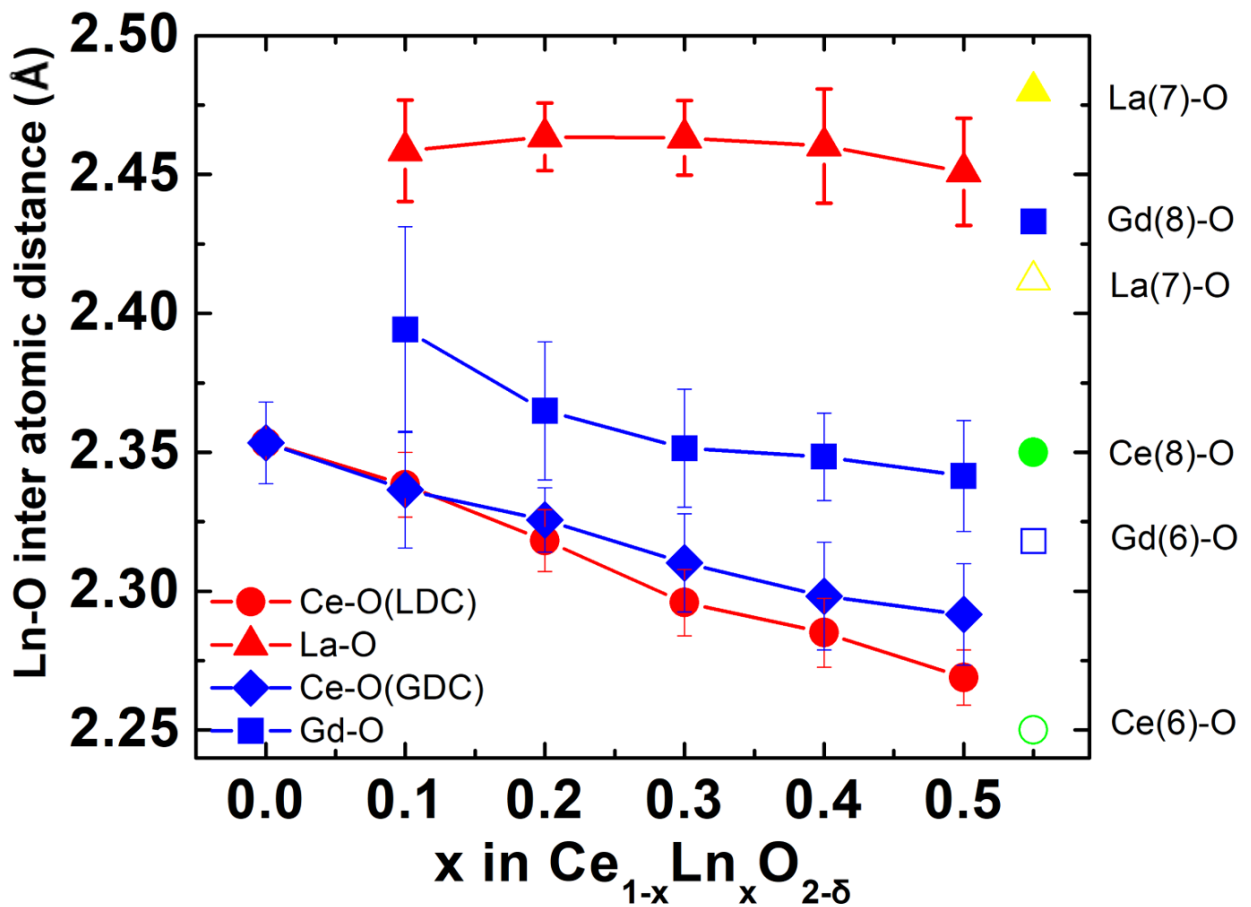


Figure 3.4 Ln-O inter atomic distance in Ce_{1-x}Ln_xO_{2-δ} (0 ≤ x ≤ 0.5) (Ln=La, Gd).

Figure 3.4 showed the curves of the Ln-O inter atomic distance in $Ce_{1-x}Ln_xO_{2-\delta}$ ($0 \leq x \leq 0.5$) (Ln = La, Gd). These curves were calculated using the first shell of the XAFS results. From these curves, we could see that the La-O distance increases slightly at approximately 2.460 Å before $x = 0.4$ and decreases slightly to 2.448 Å at $x = 0.5$. The sum of the ionic radii of 7-fold La^{3+} and 4-fold O^{2-} was 2.480 Å, and that of 6-fold La^{3+} and 4-fold O^{2-} was 2.412 Å^[23], which were depicted on the right side of Figure 5. In total, the distances remained constant with the 7-fold coordination of La, whereas the distances of Ce and O clearly changed from 2.353 Å at $x = 0$ to 2.270 Å at $x = 0.5$. The sum of the ionic radii of 8-fold Ce^{4+} and 4-fold O^{2-} was 2.350 Å and that of 6-fold Ce^{4+} and 4-fold O^{2-} was 2.250 Å. This indicated that the Ce changed from a 7-fold coordination to a 6-fold coordination on average. According to the analysis shown in Figure 3, there was no valence change in the local structure. We therefore considered that, as the factors affecting the Ce coordination change, oxygen vacancies were introduced owing to the doped La. In addition, the oxygen vacancies were completely surrounded with Ce^{4+} .

By contrast, for GDC, the distance of Ce and O changed identically as that in the LDC. This indicated that the Ce changed from an 7-fold coordination to a 6-fold coordination on average, similar to LDC. However, for the Gd and O pair, the distance decreased simultaneously with that of Ce and O, which was changed from 2.391 to 2.346 Å. These Gd-O distances were close to the sum of the ionic radii among 8-fold Gd^{3+} , 7- or 6-fold Gd^{3+} , and 4 fold O^{2-} , which are 2.433, 2.380, and 2.318 Å, respectively. This indicated that some of the coordination of Gd changed from 7- to 6-fold on average. We considered the main factor for the coordination change to be the many oxygen vacancies occurring in GDC. In addition, oxygen vacancies were statistically introduced and surround the Ce^{4+} and Gd^{3+} . It could also be observed from Figure 3.4 that, within the amount of La and Gd doping, the gap between the Ce-O distance of LDC and GDC became gradually larger. This was caused by the amount of oxygen vacancies surrounding Ce^{4+} . This was further convincing proof of our conclusion.

There are usually two factors affecting the distance between the cations and oxygen, i.e. cation's coordination number and valence (bond strength by Pauling)^[26]. For LDC, La^{3+} with a 7-fold

coordination radius is much larger than Ce^{4+} with 8- and 6-fold coordination sizes. However, the valence of La is lower than that of Ce. In the case of LDC, the coordination of La showed a constant 7-fold with increasing from $x = 0.1$ to 0.5 , whereas the coordination of Ce gradually decreased almost linearly from 8 to 6.3. This meant that the contribution of the valence to the distance of La-O was higher than that of the radius. The ability for La to catch up with O^{2-} was higher than that of Ce, and thus it could maintain the stability of the local La-O structure. Thus, the oxygen vacancies were surrounded with Ce^{4+} instead of La^{3+} . Unlike fluorite-type and the usual pyrochlore-type structure, La had a 7-fold coordination. Thus, the local cubic structure could not completely maintain the fluorite type either form a pyrochlore type structure with an increase in La. We believed that it formed a superstructure that was more like a pyrochlore type structure in LDC at $x = 0.3$. By contrast, for GDC, the size of the 6-fold coordination of Gd^{3+} was similar to the 8-fold coordination of Ce^{4+} . The Gd coordination gradually decreased at the same pace as the Ce coordination. The ability for Gd to catch up with O^{2-} was the same as that of Ce, and thus it could not maintain a stable local Gd-O structure. This was the reason why the oxygen vacancies were statistically distributed around the Ce^{4+} and Gd^{3+} . In a rare earth C-type structure, Gd^{3+} had 6-fold coordination, and in a fluorite-type structure, a 6-or 7-fold coordination was considered, and thus it was thought that the coordination number did not change significantly even if the doping amount of Gd increased. Thus, in the local area of the GDC, it finally formed a rare earth C-type structure by $x \geq 0.4$ ^[25].

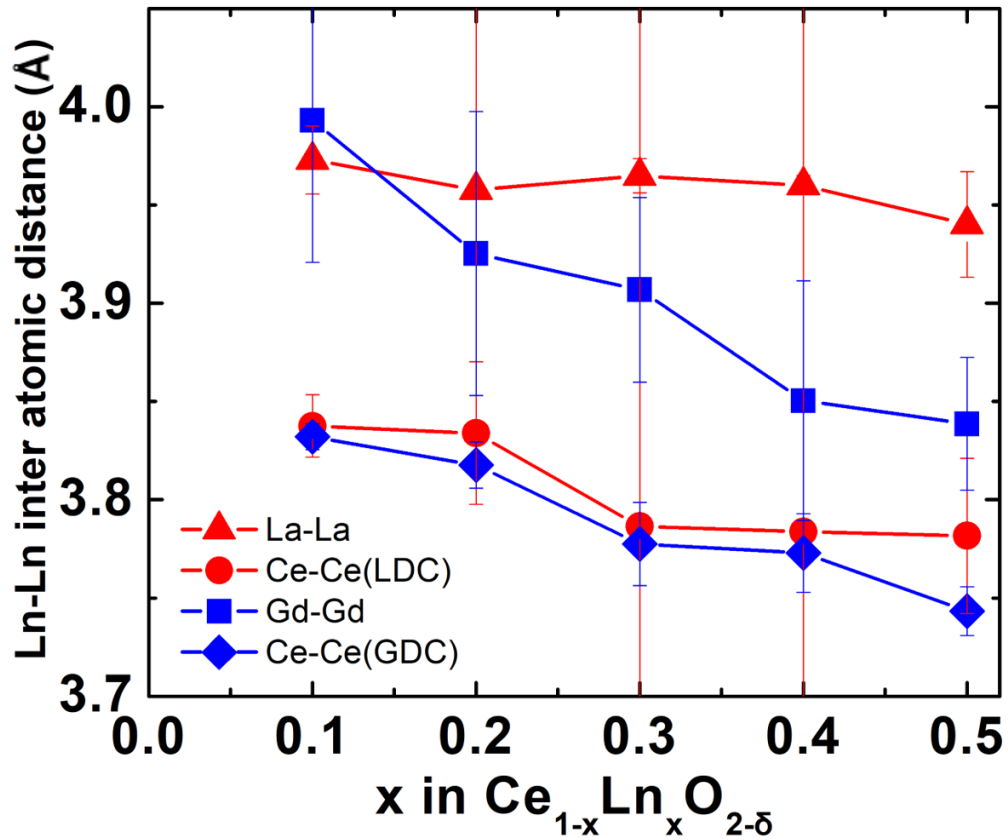
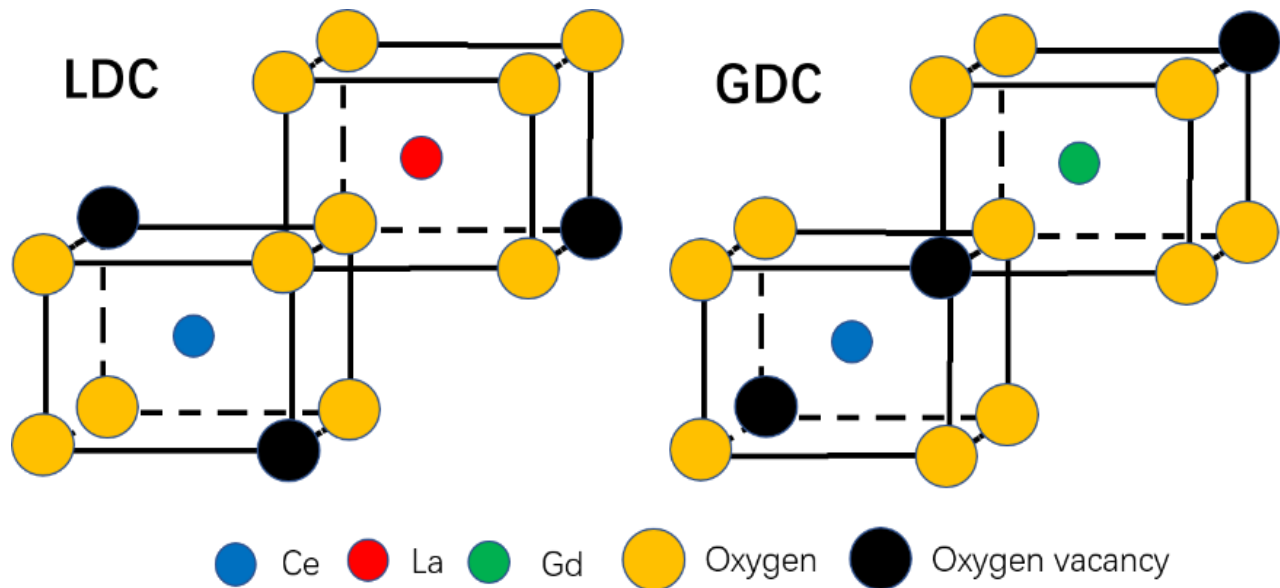


Figure 3.5 Ln-Ln inter atomic distance in $Ce_{1-x}Ln_xO_{2-\delta}$ ($0 \leq x \leq 0.5$) calculated by 2nd shell (Ln=La, Gd).

As we could see in Figure 3.5, for LDC, the curves of the second neighboring La-(La, Ce) distance and Ce-(La, Ce) distance were not synchronous with each other with an increase in x . The second neighboring contains two types of distance information: Ln-Ln and Ln-Ce^[27]. For LDC, the second neighboring La-(La, Ce) distance was first maintained ($x = 0.1-0.4$) and then slightly decreased ($x = 0.5$). This was because the La-O local structure is more stable than Ce, and thus the oxygen vacancies always surround Ce. The La-(La, Ce) distance was then stable and the Ce-(La, Ce) distance shortens with an increase in La. At the early stage of La doping, the distance contribution of the La-La pairs was extremely small. The distance of the Ce-Ce pairs made up the majority and Ce could maintain the 8-fold coordination because of the charge compensation. With an increase

in the La doping, the La-La pairs gradually played a key role in the neighboring distance. Thus, the distance became stable at approximately 3.857 Å ($x = 0.3-0.4$), whereas the distance of the Ce-Ce pairs changed significantly because the Ce changes from an 8-fold coordination to a 6-fold coordination. Thus, the second neighboring Ce-(La, Ce) distance shortened gradually with an increase in the La dopant ($x = 0.2-0.5$). By contrast, for GDC, similar to the first stage of the La- (La, Ce) second neighboring distance, the distances of Gd-(Gd, Ce) and Ce-(Gd, Ce) first increased gradually ($x = 0.1-0.2$). However, they then decreased simultaneously with the continuing of the Gd doping. This was because the local Gd-O structure is not as stable in GDC as La-O was in LDC. The oxygen vacancies occurred around both Gd and Ce. Then, the Gd-(Gd, Ce) distance and Ce-(Gd, Ce) distance were both shortened with an increase in Gd.

3.3.2 The research about XRD and XAFS results



Scheme 1 The identical model of LDC and GDC at $x=0.5$.

Scheme 1 showed an identical model of LDC and GDC at $x = 0.5$ according to the XAFS results. According to the higher ability of La^{3+} in catching up with O^{2-} , the oxygen vacancy was more like stable while the oxygen vacancies surround Ce^{4+} could move easily. So for LDC, the oxygen vacancy surrounded La was different with the one surrounded Ce. But for GDC, the oxygen

vacancies were the same as the similar ability of catching up with O^{2-} . As we could see in scheme 1, when the La concentration was low ($x = 0.1$), the La atoms were surrounded by Ce metal atoms and thus there were few chances to meet with other La atoms. Thus, with La, which had a larger ionic radius doping into the structure, the neighboring distance increases. When the La concentration was gradually introduced, the La atoms could have the chance to combine and stabilize. The curves of the second neighboring Gd-(Gd, Ce) and Ce-(Gd, Ce) distances became extremely synchronous with an increase in x .

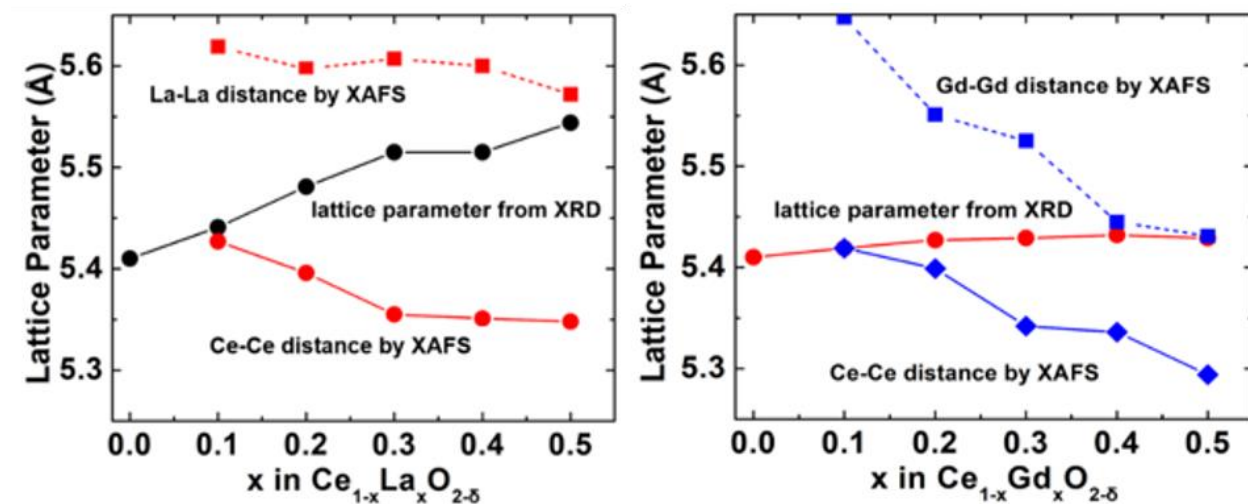


Figure 3.6 Ln-Ln inter atomic distance in $Ce_{1-x}Ln_xO_{2-\delta}$ ($0 \leq x \leq 0.5$) calculated by 2 shell (Ln=La, Gd).

Figure 3.6 showed the lattice constants of LDC and GDC and the alignment of the second proximity distance. LDC and GDC had a fluorite-type structure with a low doping amount. Because they were doped at a high amount, they were in an ideal position owing to the similar fluorite-type structure, and cations were present at the position of face-centered cubic lattice. We could then calculate the lattice parameters and the distance between the Ln-Ln.

As the Ln was doped into cerium oxide, the lattice parameter changed more gradually whereas all (Ce, Ln)-O and (Ce,Ln)-(Ce, Ln) distances decrease. At the early stage of doping, the amount of Ln was small, and the contribution of the Ln-Ln distance was not a major lattice parameter. Thus, the lattice parameter was close to the Ce-Ce distance. In other words, Ce-Ce was the framework

of the cubic structure. With gradual Ln doping, the contribution of the Ln-Ln distance increased, finally becoming the main framework in the cubic structure. This indicated that our XAFS results could fit the XRD results extremely well. In addition, it explained the relationship between the structural change and lattice parameter. It provided a new way to combine the two methods together to obtain the local structural information for the target materials.

3.3.3 The relationship between local structure change and electric conductivity

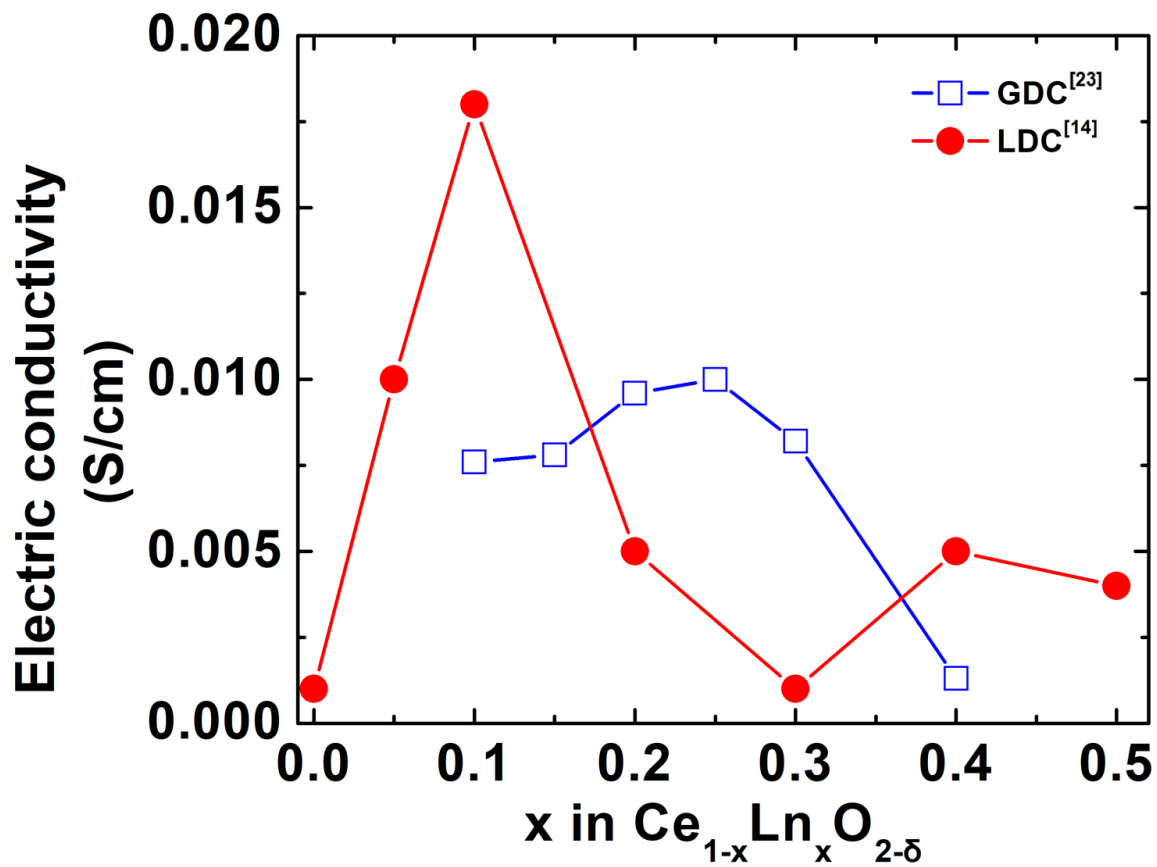


Figure 3.7 Electric conductivities of Ce_{1-x}Ln_xO_{2-δ}(Ln=La, Gd)(0 ≤ x ≤ 0.5) in the air.

Figure 3.7 showed the electrical conductivities of Ce_{1-x}Ln_xO_{2-δ}(Ln = La, Gd) (0 ≤ x ≤ 0.5) in air. The electrical conductivity of Ce_{1-x}Gd_xO_{2-δ} was referenced from Seo et al.^[24]. According to the

results above, we considered the relationship between the electric conductivities and the local structure in the following way: For LDC, at the first stage of $x = 0-0.1$, La was introduced into the CeO_2 cubic structure and replaced one Ce atom. Because La had almost no opportunity to meet with other La atoms, there was a stable oxygen vacancy caused by its local structure between La and Ce, which could form an oxygen access allowing O^{2-} to pass through. Thus, oxygen vacancies surrounded by Ce atoms occurred. Owing to the slight amount of La, the oxygen accesses were not completely formed. Thus, at the $x = 0.1$ stage, the main reason for the increase in conductivity was the increase in the amount of free oxygen vacancy. At $x = 0.1-0.3$, when the amount of La increased, the oxygen vacancies caused by the local structural change in La increase but still could not effectively form an oxygen access. By contrast, the amount of free oxygen vacancies clearly decreased. These two reasons caused the conductivity to decrease from 0.1 to 0.3. As with $x = 0.2-0.3$, the structure began to change from fluorite to a superstructure and some oxygen accesses were built up, which appeared as the rate of decrease becomes less sharp as that of $x = 0.1-0.2$. At $x = 0.3-0.4$, the amount of La continuously increased, as did the ordered degree of the superstructure. In addition, the stable oxygen vacancies increased, clearly forming an oxygen access, which was the main reason why the conductivity increased from 0.3 to 0.4. At $x = 0.4-0.5$, the ordered degree of the superstructure increased. The amount of free oxygen vacancies decreased, which was the main reason for the lower conductivity.

For GDC, the main factor affecting the conductivity was the number of oxygen vacancies. Thus, like the other materials that had a doped metal element, the number of oxygen vacancies first increased and then decreased with the continual doping of the metal element. When a large amount of Gd was doped, the order degree of the C-type structure increased, whereas the oxygen vacancies remained in a statistically distributed state. Thus, the conductivity of the GDC appeared to first increase and then decrease.

3.4 Conclusion

In this part of work, the changes in local structures of $\text{Ce}_{1-x}\text{Ln}_x\text{O}_{2-\delta}$ with Ln (La, Gd) doping were investigated. XAFS was successfully used to clarify the coordination environments around Ce and the dopant La and Gd. For LDC, La coordination was maintained at 7, and Ce coordination decreased from 8 to 6. It was speculated that because a superstructure would be formed which was more like a pyrochlore structure in LDC at $x > 0.3$, the oxygen vacancies could be attracted by the larger La^{3+} . For GDC, the coordination numbers for Gd and Ce decreased from 8 to 6. In the GDC, oxygen vacancies had no preference for Ce or Gd coordination.

We also combined XRD results and EXAFS results together. These results explained the changes in the lattice parameters for both LDC and GDC. The local structure change model was designed and the electric conductivity change at each stage of Ln (La, Gd) doping was explained. In future studies, these results can be applied to other materials.

Reference

- [1] U. Fano Sullo spettro, *Il Nuovo Cimento* (1924-1942) 12, (1935) 154-161.
- [2] U. Fano and J. Cooper, *Reviews of Modern Physics* 40, (1968) 441.
- [3] D. C. Koningsberger, R. Prins (eds) A. Bianconi, (*Chemical Analysis* 92), Wiley, New York (1988) pp 573-662.
- [4] A. Bianconi, *Applications of Surface Science* (1980) pp. 392-418.
- [5] M. Belli, A. Scafati, A. Bianconi, S. Mobilio, L. Palladino, A. Reale, and E. Burattini, *Solid State Communications* 35 (1980) pp. 355-361.
- [6] J. Dehmer and D. Dill, *Physical Review Letters* 35, (1975) 213.
- [7] J. J. Rehr and A. L. Ankudinov, *Coordination Chemistry Reviews* 249, (2005) 131.
- [8] M. Benfatto, C. R. Natoli, A. Bianconi, J. Garcia, A. Marcelli, M. Fanfoni, and I. Davoli, *Physical Review B* 34, (1986) pp. 5774-5781.
- [9] D.C. Koeningsberger, R. Prins, John Wiley & Sons 1988.
- [10] Biwer, B. M.; Soderholm, L.; Greeger, R. B.; Lytle, F. W. (1996-12-31).
- [11] Bordwehr, R. Stumm von (1989), *Annales de Physique*. 14 (4): 377–465.
- [12] Stern, Edward A. (2001-03-01), *Journal of Synchrotron Radiation*. 8 (2): 49–54.
- [13] Quantum Leap XAS, [on line].
- [14] M.Mori, H. Sumi and E. Suda, Abstract for the Ceramic Society of Japan the 29th Fall Meeting, 1PV01 (2016).
- [15] H. Yamamura, H. Nishino, K. Kakinuma and K. Nomura, *Solid State Ionics*, 158 (2003) 359–365.
- [16] L. Kalland, S. T. Norberg, J. Kyrklund, S. Hull, S. G. Eriksson, T. Norby, C. E. Mohn and C. S. Knee, *Phys. Chem. Chem. Phys.*, 18, (2016) 24070–24080.
- [17] E. Suda, B. Pacaud, Y. Montardi, M. Mori, M. Ozawa and Y. Takeda, *Electrochemistry*, 71 (2003) 866–872.
- [18] R. D. Shannon. *Acta Cryst.* (1976) A32, 751-767.
- [19] B. Ravel and M. Newville, *J. Synchrotron Rad.*, 12 (2005) 537–541.

- [20] X. Li, Z. Feng, J. Lu, F. Wang, M. Xue, G. Shao, *Ceram. Int.*, 38 (2012) 3203–3207.
- [21] J. Zhang, C. Ke, H. Wu, J. Wang and Y. Wang, *J. Alloys Comp.*, 718 (2017) 85–91.
- [22] S. Yamazaki and T. Matsui, *Netsu Sokutei*, 26(3) (1999) 82–91.
- [23] D. Seo, K. Ryu, S. Park, K. Kim, R. Song, *Mater. Res. Bull.*, 41 (2006) 359–366.
- [24] R. D. Shannon, *Acta Cryst.*, (1976), A32, 751–767.
- [25] M. Nolan, *J. Phys. Chem. C*, 115 (2011) 6671–6681.
- [26] L. Pauling, *J. Chem. Educ.* 1992, 69, 7, 519.
- [27] H. Deguchi, H. Yoshida, T. Inagaki, M. Horiuchi, *Solid State Ionics* 176, (2005) 1817–1825.

Chapter 4: Structure changes of $\text{Ba}_{1-x}\text{Zr}_{1-y}\text{Y}_y\text{O}_{3-\delta}$ electrolyte materials

4.1 Introduction

At elevated proton conductivity, some perovskite oxides also show higher temperatures, which acceptor-doped cerium-barium and zirconate^[1-3] are applied in solid oxide fuel cells (SOFC). They are also the most promising materials for other applications such as gas separators and pumps, hydrogen sensors, and electrochemical reactors for hydrogenation or dehydrogenation of hydrocarbons^[4,5]. However, the doped barium cerate shows poor ability to the thermal, mechanical, and chemical stability. It appears weak points especially under the hydrogen or hydrocarbon gases conditions contaminated by gaseous and minor components, such as CO_2 , CO , SO_2 , H_2S and water vapor^[6,7]. Therefore, their application has proven problematic in fuel cells. On the other hand, barium zirconate appears excellent mechanical and chemical stability, and also sufficient bulk proton conductivity. It is considered as the promising material for SOFC applications^[8-11]. However, two other important limitations exist in the noble metal element doped barium zirconate (such as $\text{BaZr}_{1-x}\text{Y}_x\text{O}_{3-\delta}$ (BZY)) on its usefulness^[9,12,13]. The first one is, to obtain a dense material, a high sintering temperature is required (up to $1700\text{ }^\circ\text{C}$), which is the reason of BaO pellet sublimation and surface decomposition. Another one is, the overall conductivity is poor due to the extremely high grain boundary resistance in this kind of material. In such case, there are many complex technologies researched to prepare BZY electrolyte films in order to overcome the conductivity limitation caused by high grain boundary resistance. This is the main method now in the research to reduce the total electrolyte resistance and improve the fuel cell efficiency. But it has not been achieved a suitable way so far. To solve the problem above, there is another way to modify the materials used. Dope elements into the material to enhance the required function is considered as the simplest and most effective way to control the solid electrolytes performance without degrading other wonderful properties. Until now, there are many publications on this kind

of topic. Most of the published literatures are attempted on doped barium zirconate to improve electrical properties. They have been focused on using various of doping elements (or sintering aids) to improve the sinterability. It can also be helpful on BZY physical and chemical surface appearance with reducing sintering temperature. For changing formulations, there are several effective techniques of wet chemical pathways, such as sol-gel, combustion, co-precipitation, peroxide processes^[14-19]. Several sintering aids can also have the efforts on reducing the sintering temperature of perovskite-type ceramics. However, there are only a few sintering aids which can efficiently promote the zirconia-based perovskites densification in the liquid-phase to sinter at lower temperatures such as Li₂O, LiF, and ZnO^[20-24]. Although this is the easiest way to obtain the dense films, more work are still need to be taken in the future when using these fluxes. Because their incorporation can have great affection on the mechanical and electrical properties of the electrolyte. In the previous literature, it was found that with small amount sintering aids (about 1 wt.%) of ZnO, it can improve the BZY pellet`s technical efficiency on manufacturing and reduce the sintering temperature to 1400–1450 ° C without decreasing its electrical properties^[23,24]. So in this work, we researched about the effect of composition of the Ba_{1-x}Zr_{1-y}Y_yO_{3-δ} to the conductivity. And we also researched about the effect of the powder bed method(PB) to the BZY surface composition.



Figure 4.1 Ba_{0.96}Zr_{0.9}Y_{0.1}O_{3-δ} + ZnO 1wt% of PB method before and after sintering at 1600 °C.

4.2 Experiment

$Ba_{1-x}Zr_{1-y}Y_yO_{3-\delta}$ ($x = 0.02, 0.04$) and ($y = 0.1, 0.2, 0.3$) were synthesized by solid state method. $BaCO_3$, ZrO_2 and Y_2O_3 were used as starting materials and weighed by stoichiometric ratio. The weighed samples were mixed for 45 minutes and calcined from $1200^\circ C$ to $1380^\circ C$ for 24 hours, respectively. The samples were characterized by XRD and then ball milled for 24 hours. Water or acetone was used as the solvent. After that, they were dried under low pressure. After above steps, the samples were mixed for 10 minutes, and structural analysis was performed by XRD. The pellets were molded at 30 N for 2 minutes. The pelletized samples were fired for 5 hours ($1400^\circ C$ - $1600^\circ C$).

1 wt%, 2 wt% and 3 wt% of ZnO were added to the dried sample of $Ba_{0.96}Zr_{0.9}Y_{0.1}O_{3-\delta}$, and mixed for 45 minutes, respectively. The samples molded into pellets at 30 N for 2 minutes, and the density was calculated from the diameter, thickness and mass of the green pellets which were fired. The samples were sintered from $1300^\circ C$ to $1600^\circ C$. The density of the obtained sample was calculated, and the rate of change in density was compared with the green pellets.

The sintered sample was formed using a diamond cutter, and platinum paste was applied to both surfaces of the sample, and the platinum electrode was sintered at $800^\circ C$ for 2 hours. The conductivity of this sample was measured at 700 - $500^\circ C$ under a humid atmosphere and a hydrogen reducing atmosphere using an alternating current impedance method.

4.3 Results and discussions

First we synthesized the $\text{BaZr}_{1-x}\text{Y}_x\text{O}_{3-\delta}$ ($x=0,0.1,0.2$) with solid state method. We measured the samples with XRD method. Figure 4.2 is the XRD pattern of $\text{BaZr}_{1-x}\text{Y}_x\text{O}_{3-\delta}$ at 1600°C . From the XRD pattern, we could see that the target materials which took BaZrO_3 as the mother phase were synthesized. However, it was observed that the intensity of Y_2O_3 which was the impurity phase increased according to the doping amount of Y.

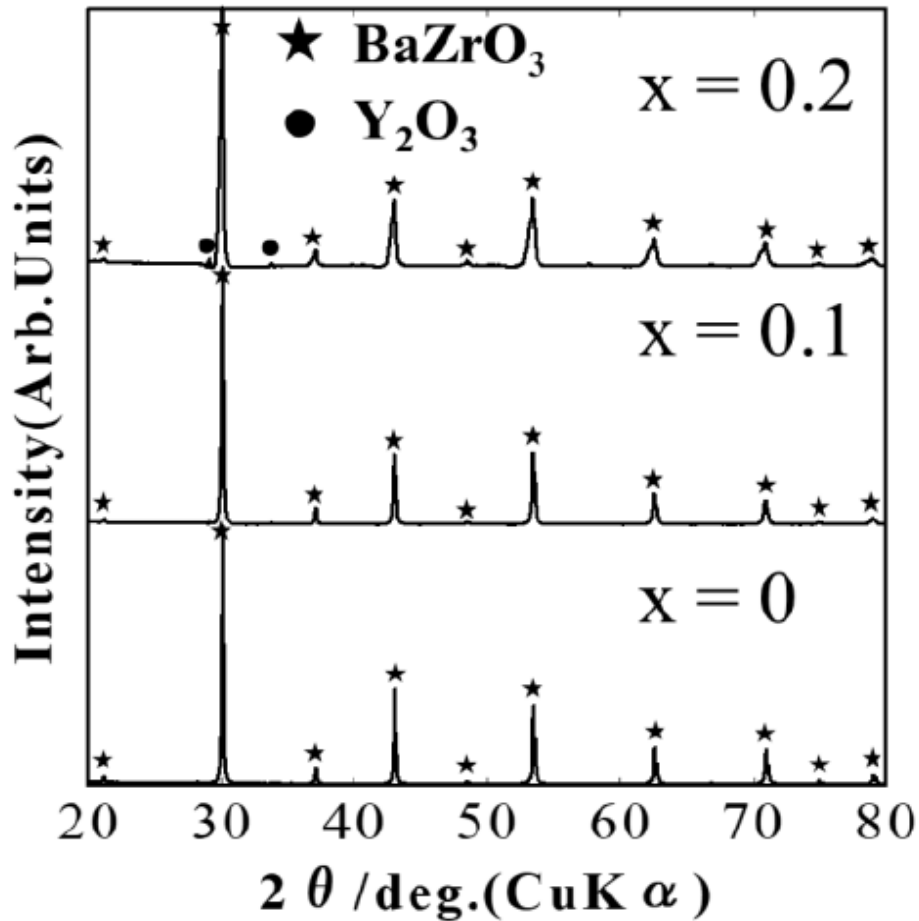


Figure 4.2 The XRD pattern of $\text{BaZr}_{1-x}\text{Y}_x\text{O}_{3-\delta}$ at 1600°C .

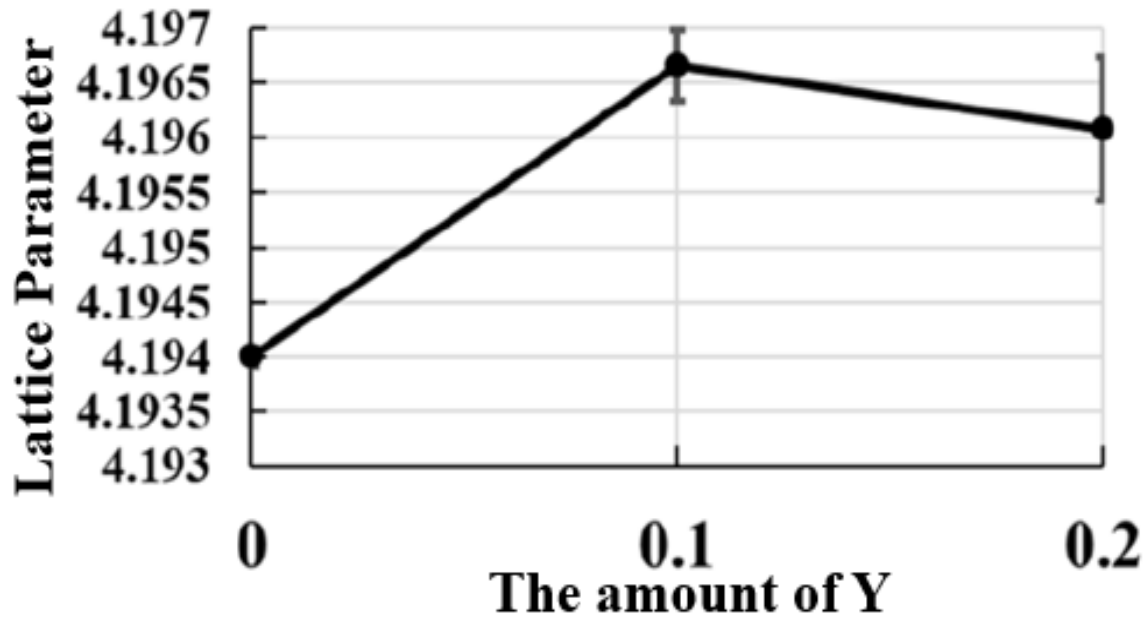


Figure 4.3 The Lattice constant of $\text{BaZr}_{1-x}\text{Y}_x\text{O}_{3-\delta}$ at 1600°C .

We calculated the lattice parameters of three samples from the XRD patterns. Figure 4.3 was the Lattice constant of $\text{BaZr}_{1-x}\text{Y}_x\text{O}_{3-\delta}$ at 1600°C . From figure 4.3, we could see that when the doping amount of Y increased are from 0 to 0.1, the lattice parameter got higher obviously. As to $y = 0.1-0.2$, the lattice constant did not change significantly considering the error bars. From this result, we could conclude that to the solid state method under our experiment condition, it was possible to synthesize when the Y doping amount was $y = 0.1$ because the lattice parameter changed obviously. But as to the amount of Y was 0.2, it was difficult to obtain the target products. So we focused on the conditions of the amount of Y was 0.1.

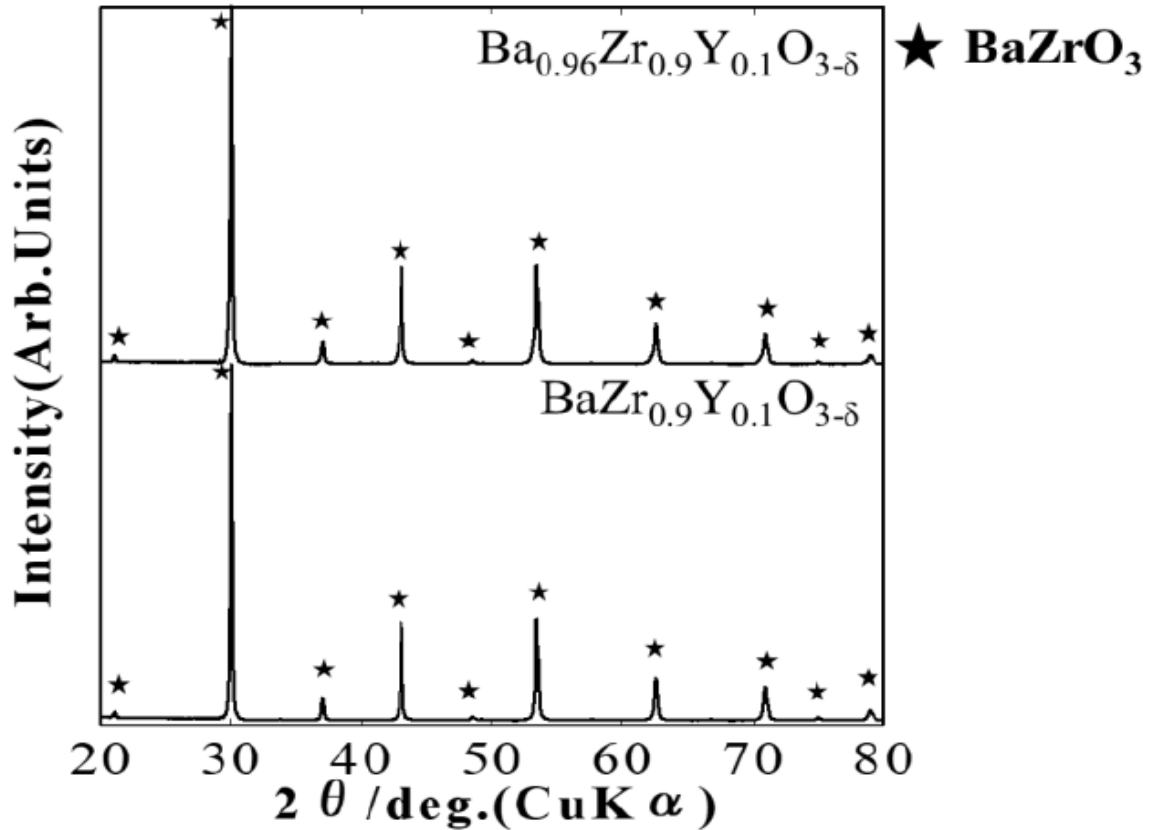


Figure 4.4 The XRD pattern of $\text{Ba}_{1-x}\text{Zr}_{0.9}\text{Y}_{0.1}\text{O}_{3-\delta}$ ($x=0, 0.04$) at 1600°C for 5h.

Then we investigated the affection about the composition of Ba. We prepared two samples of $\text{Ba}_{1-x}\text{Zr}_{0.9}\text{Y}_{0.1}\text{O}_{3-\delta}$ ($x = 0, 0.04$). Figure 4.4 shows the XRD pattern of $\text{Ba}_{1-x}\text{Zr}_{0.9}\text{Y}_{0.1}\text{O}_{3-\delta}$ ($x = 0, 0.04$) sintered at 1600°C for 5 h. From the XRD patterns, we could see that the XRD peak of two samples showed a single BaZrO_3 phase. That indicated the synthesis of $\text{Ba}_{1-x}\text{Zr}_{0.9}\text{Y}_{0.1}\text{O}_{3-\delta}$ ($x=0, 0.04$) was successful. However, the peak of (222) Y_2O_3 was appeared in both samples at around 29° , and the relative intensities were 0.19 and 0.06, respectively. From this result, it was considered that more Y^{3+} could be doped compared to Ba composition of 1 by changing the Ba composition to 0.96.

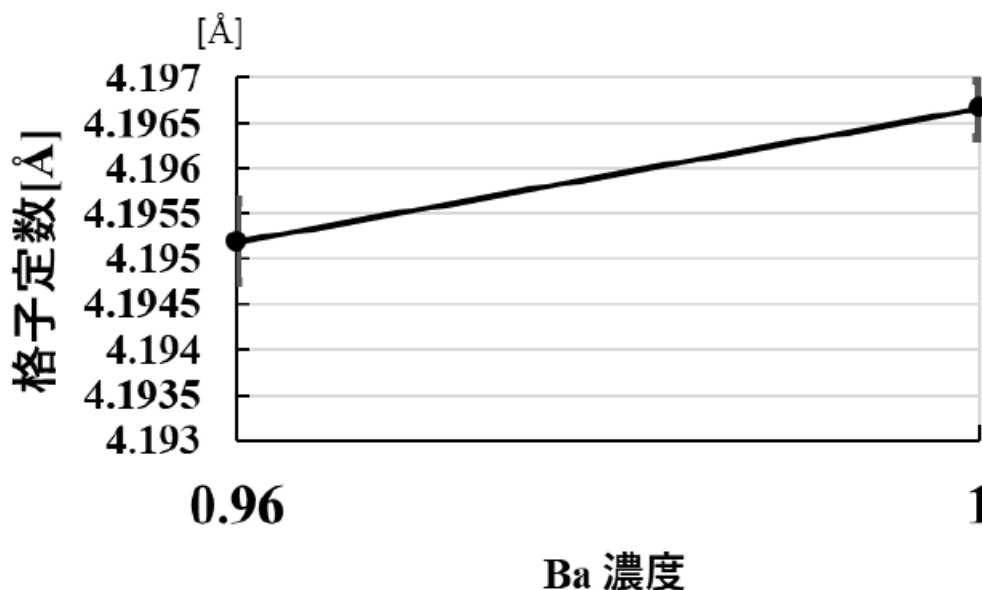


Figure 4.5 The Lattice constant of $\text{Ba}_{1-x}\text{Zr}_{0.9}\text{Y}_{0.1}\text{O}_{3-\delta}$ ($x=0, 0.04$) at 1600°C for 5h

Then we calculated the lattice constant of $\text{Ba}_{1-x}\text{Zr}_{0.9}\text{Y}_{0.1}\text{O}_{3-\delta}$ ($x = 0, 0.04$) which are sintered at 1600°C for 5 h from Fig. 4.4. The lattice constant decreased with decreasing the amount of Ba. In the reference, there are some research on $\text{BaZr}_{0.8}\text{Y}_{0.2}\text{O}_{3-\delta}$ materials in which the Ba site was similarly deleted, the lattice constant tends to decrease with decreasing the Ba composition^[25]. It could be the proof of our experimental result. This result was considered from the ion radius of each element Ba, Zr, Y, and indicates that Ba^{2+} (12 coordination) = 1.61 \AA , Zr^{4+} (6 coordination) = 0.72 \AA , Y^{3+} (6 coordination) = 0.9 \AA , respectively. It was considered that lattice contraction had occurred because Ba^{2+} , which had the largest ionic radius, was taken out from the structure. These results supported the stable existence of BaZrO_3 even if it was in the state of being deficient in Ba site, and think that it was possible to dope larger Y^{3+} to Zr^{4+} site by deficient in Ba^{2+} which was the largest ion radius.

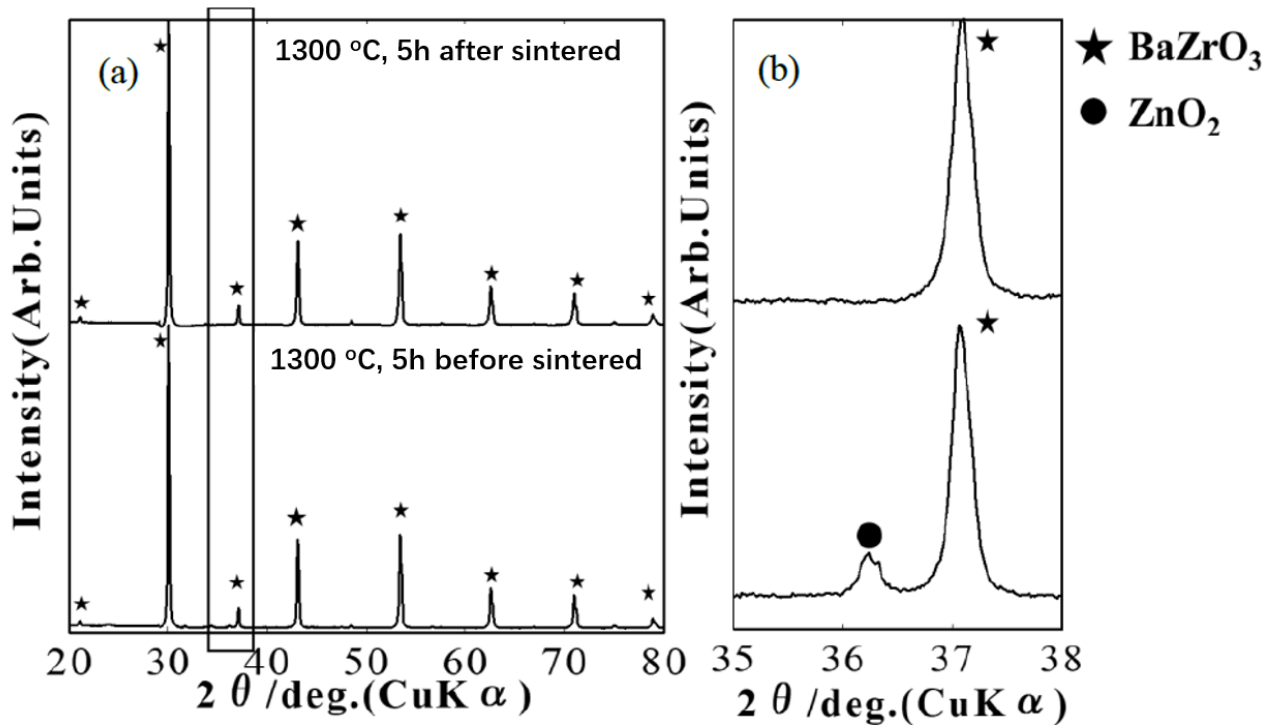


Fig. 4.5 (a) The XRD pattern of $\text{Ba}_{0.96}\text{Zr}_{0.96}\text{Y}_{0.1}\text{O}_{3-\delta} + 3\text{wt}\% \text{ZnO}$ before sintering and after sintering at 1300°C for 5h. (b) the expansion figure of $35^\circ - 38^\circ$.

Next we introduced ZnO as the sintering aid into $\text{Ba}_{0.96}\text{Zr}_{0.96}\text{Y}_{0.1}\text{O}_{3-\delta}$. We compared the samples of $\text{Ba}_{0.96}\text{Zr}_{0.96}\text{Y}_{0.1}\text{O}_{3-\delta} + 3\text{wt}\% \text{ZnO}$ before sintering and after sintering at 1300°C for 5h. We also take the XRD measurement for them. Figure 4.5 (a) is the XRD pattern of $\text{Ba}_{0.96}\text{Zr}_{0.96}\text{Y}_{0.1}\text{O}_{3-\delta} + \text{ZnO}(1-3)\text{wt}\%$ before sintered and after sintered at 1300°C for 5 h. An enlarged view is shown at $35^\circ - 38^\circ$ in Fig. 3.5 (b). In the addition range of ZnO 0-3 wt%, the relative density was improved as the amount of ZnO increased. It was considered that the sinter ability was improved because the ZnO was added as a sintering aid to become a liquid phase so that the particles were easily diffused in the sinter process.

As for ZnO, it could be seen from Fig. 4.5 (b) that ZnO doped with 3 wt% relative to $\text{Ba}_{0.96}\text{Zr}_{0.96}\text{Y}_{0.1}\text{O}_{3-\delta}$ disappears after sintering. It was considered that ZnO was evaporated. So that the ZnO peak was not detected by XRD measurement because it was evaporated or doped

with $\text{Ba}_{0.96}\text{Zr}_{0.96}\text{Y}_{0.1}\text{O}_{3-\delta}$. However, when ZnO was added, the color of the pellet changed from white to black. From the colour change, it was difficult to say that it has evaporated in general.

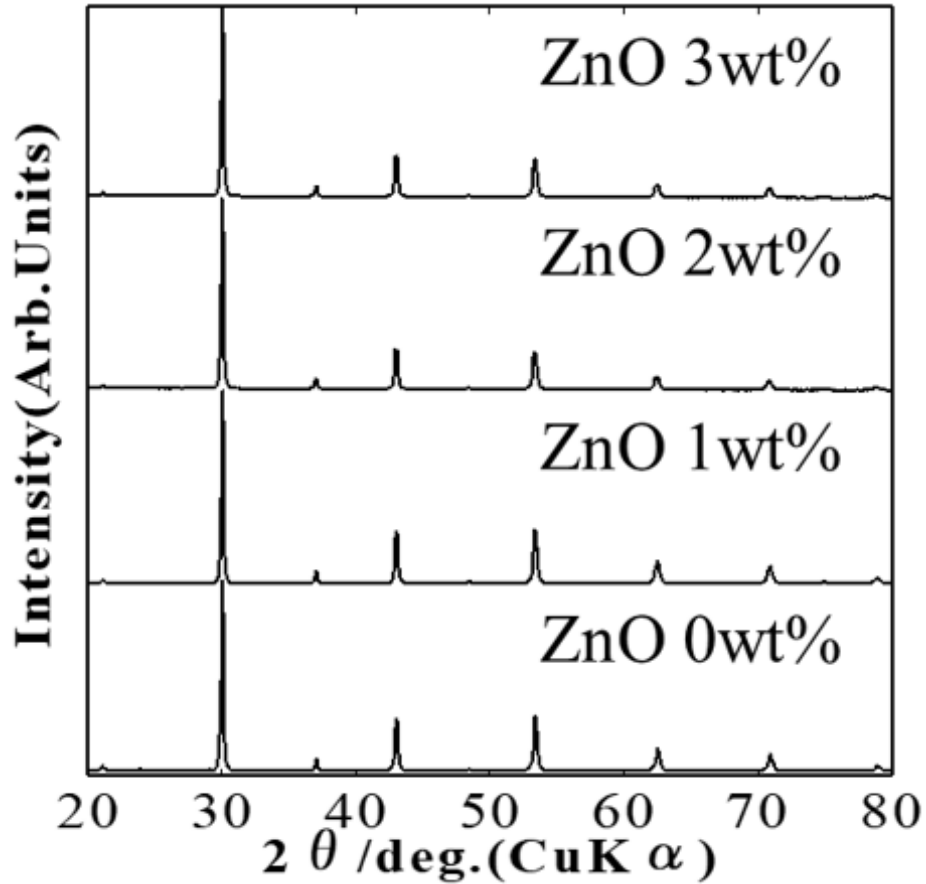


Figure 4.6 XRD pattern of $\text{Ba}_{0.96}\text{Zr}_{0.9}\text{Y}_{0.1}\text{O}_{3-\delta} + \text{ZnO}$ (0-3) wt% sintered at 1500 ° C for 5 h.

Under the above experiment conditions, we synthesis the samples of $\text{Ba}_{0.96}\text{Zr}_{0.9}\text{Y}_{0.1}\text{O}_{3-\delta} + \text{ZnO}$ (0-3) wt% sintered at 1500 ° C for 5 h. Figure 4.6 shows the XRD patterns of each sample. From these XRD pattern we could see that the ZnO peak was not detected in all samples. All the samples were single phase which suggested the target samples were successfully synthesized.

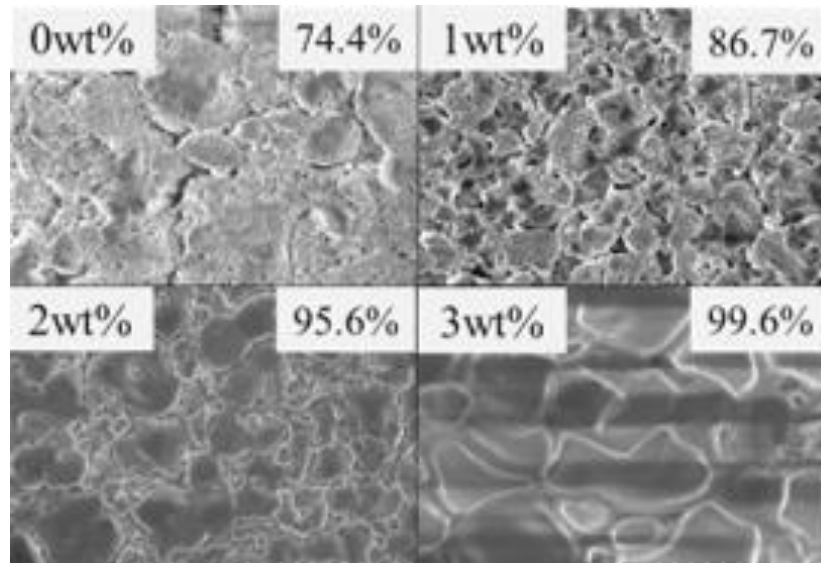


Figure 4.7 SEM image and relative density of $\text{Ba}_{0.96}\text{Zr}_{0.9}\text{Y}_{0.1}\text{O}_{3-\delta} + \text{ZnO}$ (0-3) wt% sintered at $1500\text{ }^{\circ}\text{C}$ for 5 h.

We took the SEM measurement for all the samples of $\text{Ba}_{0.96}\text{Zr}_{0.9}\text{Y}_{0.1}\text{O}_{3-\delta} + \text{ZnO}$ (0-3) wt% sintered at $1500\text{ }^{\circ}\text{C}$ for 5 h. Figure 4.7 is the SEM image and relative density of $\text{Ba}_{0.96}\text{Zr}_{0.9}\text{Y}_{0.1}\text{O}_{3-\delta} + \text{ZnO}$ (0-3) wt% sintered at $1500\text{ }^{\circ}\text{C}$ for 5 h. From the SEM images, we could obviously see that the pores were disappeared gradually with the amount of ZnO added in. It was through melting mode of the $\text{Ba}_{0.96}\text{Zr}_{0.9}\text{Y}_{0.1}\text{O}_{3-\delta} + \text{ZnO}$ 3 wt% sample. The relative density of each samples were also increasing with the ZnO doping in. The samples density of ZnO 2wt% and 3wt% were all over 95%. And the sample density of ZnO 1wt% was nearly 90%. They were all appropriate to higher electric conductivity than the ZnO 0wt% samples.

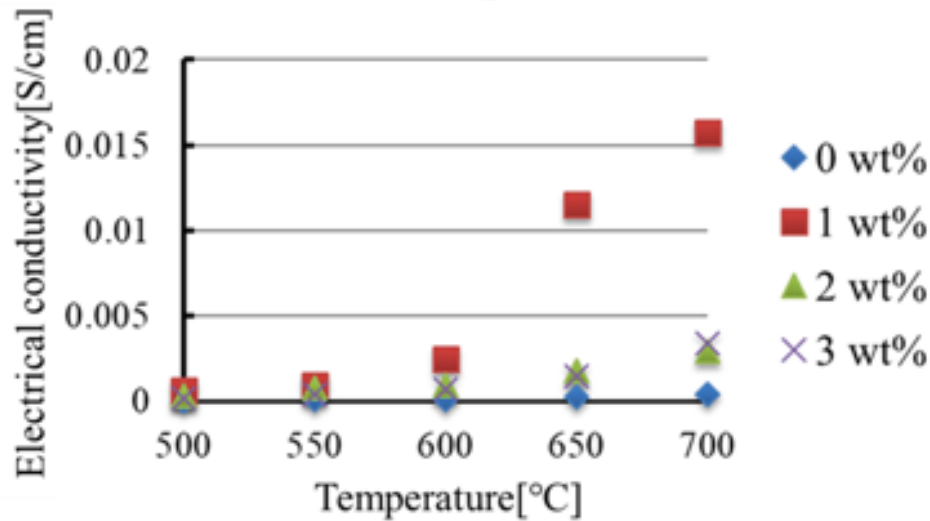


Figure 4.8 Electrical conductivities of $\text{Ba}_{0.96}\text{Zr}_{0.9}\text{Y}_{0.1}\text{O}_{3-\delta} + \text{ZnO}$ (0-3) wt% sintered at $1500\text{ }^{\circ}\text{C}$ for 5 h in humid air atmosphere.

So, we took 4 samples to AC impedance analysis measurement. Figure 4.8 shows the electrical conductivities in a humid air atmosphere. From Figure 4.8, we could see that when ZnO addition amount was 1wt%, it showed the maximum value of all the electric conductivities in the measurement temperature range (700-500 °C). However, when the added amount of ZnO exceeded 2 wt%, the electrical conductivity was significantly reduced. These results showed that the electrical conductivity could be improved by increasing the relative density up to 1 wt%. However, at 2 wt% or more, the Zn component was present in a trace amount in BZY and it was doped in BZY locally. It was thought that the perovskite structure was destroyed so that the grain boundary resistance was increased. And the ZnO formed a resistive phase.

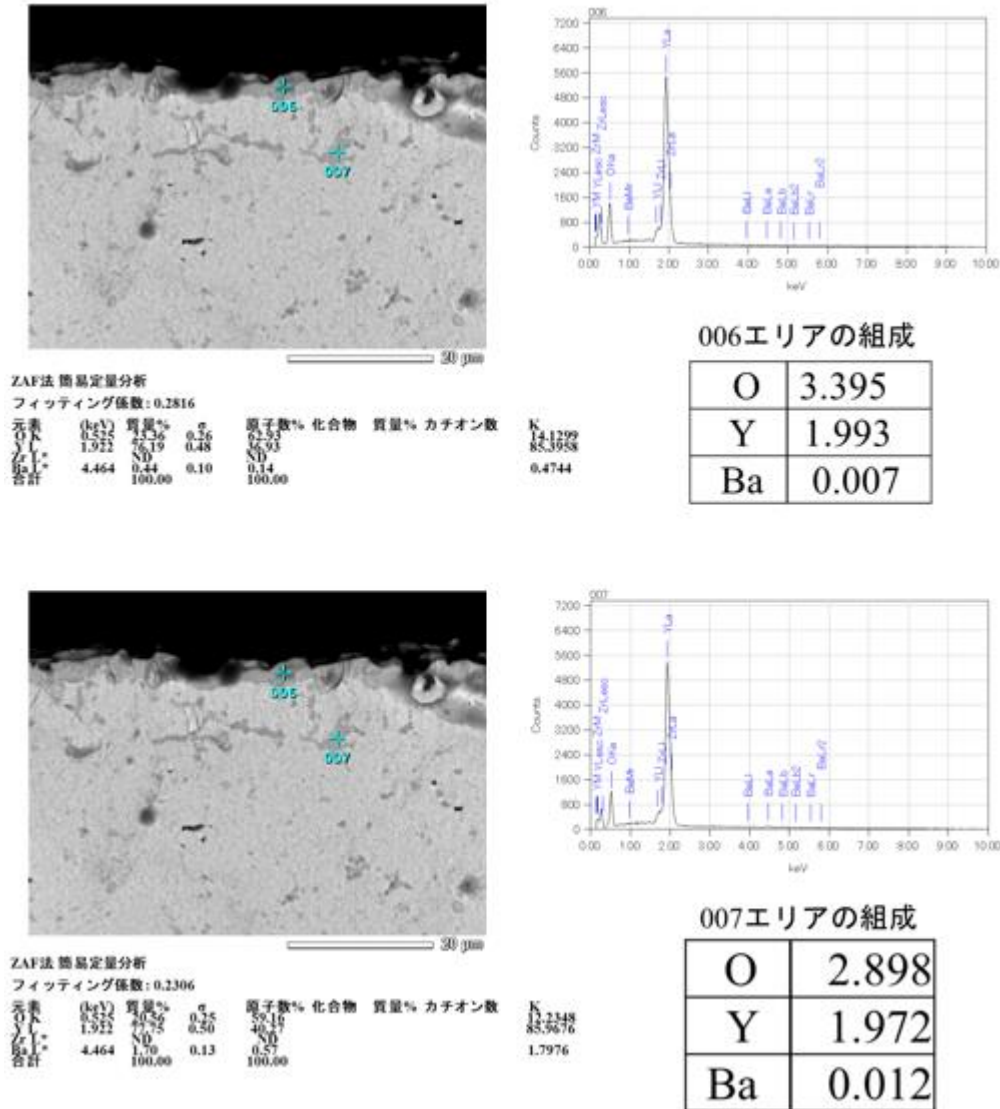


Figure 4.9 Area analysis and spectrum of $\text{Ba}_{0.96}\text{Zr}_{0.9}\text{Y}_{0.1}\text{O}_{3-\delta} + \text{ZnO}$ 3wt% sintered at 1500°C for 5 h.

Next we took the EDS measurement of $\text{Ba}_{0.96}\text{Zr}_{0.9}\text{Y}_{0.1}\text{O}_{3-\delta} + \text{ZnO}$ 3wt% sintered at 1500°C for 5 h. Figure 4.9 shows the area analysis spectrum of $\text{Ba}_{0.96}\text{Zr}_{0.9}\text{Y}_{0.1}\text{O}_{3-\delta} + \text{ZnO}$ 3wt%. From the results of the area analysis, it was confirmed that a phase derived from Y_2O_3 was deposited on the surface of the pellet of $\text{Ba}_{0.96}\text{Zr}_{0.9}\text{Y}_{0.1}\text{O}_{3-\delta} + \text{ZnO}$ 3wt%. It was thought to be the reason of the decrease in electrical conductivity in figure 4.8. The segregation of Y_2O_3 on the surface formed a resistance phase. Further, it was considered that since Y^{3+} was removed locally, it did not act as a

dopant and decreased the electrical characteristics of the material. However, in the EDS, the Y^{3+} excess phase was observed, while the Y^{3+} deficiency phase could not be identified. Thus, more detailed investigation is required.

$Ba_{0.96}Zr_{0.9}Y_{0.1}O_{2-\delta}$	Ba amount(PB)	Ba amount	Y amount(PB)	Y amount
ZnO 0wt%	0.98	0.97	0.1	0.1
ZnO 1wt%	0.97	0.84	0.1	0.11
ZnO 3wt%	0.83	0.66	0.26	0.3

Table 1 Ba composition by XRF analysis of $Ba_{0.96}Zr_{0.9}Y_{0.1}O_{3-\delta} + ZnO$ (0-3wt%) powder sintered at 1500 ° C for 5 h with and without PB method.

$Ba_{0.96}Zr_{0.9}Y_{0.1}O_{2-\delta}$	Ba amount(PB)	Ba amount
ZnO 0wt%	1.02	1.00
ZnO 1wt%	1.18	1.01
ZnO 3wt%	1.04	1.00

Table 2 Ba, Y composition by XRF analysis of $Ba_{0.96}Zr_{0.9}Y_{0.1}O_{3-\delta} + ZnO$ (0-3wt%) pellet surface sintered at 1500 ° C for 5 h with and without PB method.

Table 1 is the Ba composition by XRF analysis of $Ba_{0.96}Zr_{0.9}Y_{0.1}O_{3-\delta} + ZnO$ (0-3wt%) powder sintered at 1500 ° C for 5 h with and without PB method. From Table 1, we could see that the evaporation of Ba was not seen under the sintering conditions in both methods. Table 2 is the Ba, Y composition by XRF analysis of $Ba_{0.96}Zr_{0.9}Y_{0.1}O_{3-\delta} + ZnO$ (0-3wt%) pellet surface sintered at 1500 ° C for 5 h with and without PB method. From Table 2, it could be seen that the Ba composition ratio decreased and the Y composition ratio increased with the addition amount of ZnO in both methods. These results suggested that ZnO was related with the formation of the Y_2O_3 phase on the pellet surface. In addition, the Ba composition ratio of the pellet surface of the sample which was added with 3 wt% of ZnO sintered by the PB method and the pellet surface

sintered without PB method were 0.83 and 0.66, respectively. And the Y composition ratio was 0.26 and the other one was 0.27, respectively. From the above data, it was considered that the formation of the Y_2O_3 phase on the pellet surface could be suppressed by the PB method.

	Zn	Ba	Zr	Y
ZnO 0wt%	0	0.96	0.9	0.1
ZnO 1wt%	0.042	0.96	0.9	0.1
ZnO 3wt%	0.11	0.96	0.9	0.1

Table 3 (1) Theoretical composition of $Ba_{0.96}Zr_{0.9}Y_{0.1}O_{3-\delta} + ZnO$ (0-3wt%) sintered at 1500 ° C for 5 h.

	Zn	Ba	Zr	Y
ZnO 0wt%	0	1.00	0.9	0.1
ZnO 1wt%	0.0019	1.01	0.9	0.1
ZnO 3wt%	0.0079	1.00	0.9	0.1

Table 3 (2) XRF composition of $Ba_{0.96}Zr_{0.9}Y_{0.1}O_{3-\delta} + ZnO$ (0-3wt%) powder sintered at 1500 ° C for 5 h.

Table 3 (1) and (2) compare the theoretical and experimental of each element composition in the $Ba_{0.96}Zr_{0.9}Y_{0.1}O_{3-\delta} + ZnO$ (0-3wt%) samples with the XRF measurement. In figure 4.10, the remaining amount was shown. As shown in Figure 4.10, in all the samples which ZnO was added, a smaller amount of Zn remained than in Table 3 (2) even though the peak for Zn was not detected. Considering the above results and the fact that ZnO peak was not detected in XRD, we concluded that the ZnO was doped into BZY as amorphous. And since it had a tendency to increase the lattice constant, it was doped in the interstitial. So the peak could not be confirmed by XRD probably.

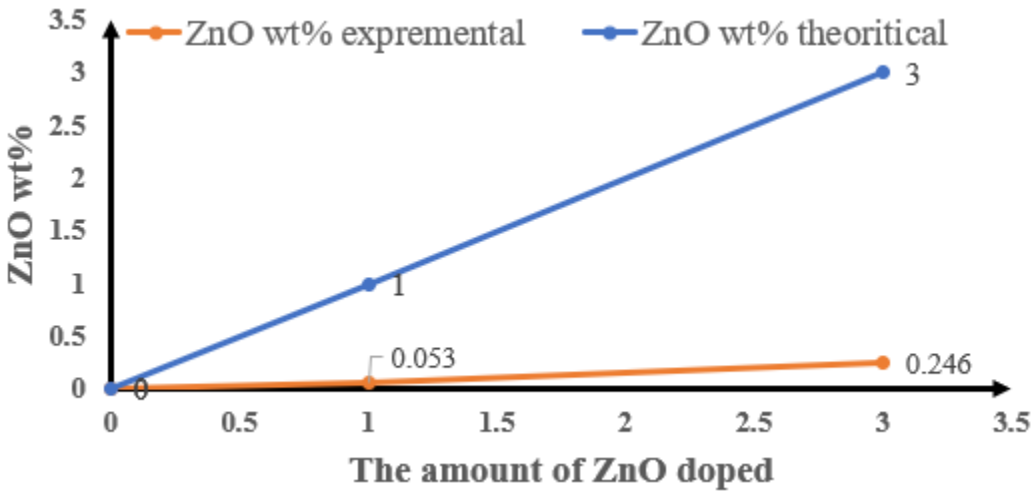


Fig.4.10 Comparison of ZnO composition in Table 3 (1), (2).

We want to research about the effect of relative density due to suppression of Y precipitation on the surface by the PB method. Table 4 is the relative density of $\text{Ba}_{0.96}\text{Zr}_{0.9}\text{Y}_{0.1}\text{O}_{3-\delta} + \text{ZnO}$ (0-3wt%) sintered at 1500 °C for 5h with and without PB method. As Table 4 result, all samples showed similar values of relative density regardless with or without the PB method. It could be concluded that the deposition of yttrium oxide on the surface did not affect the improvement of the density. Fig.4.11 is the lattice constant of $\text{Ba}_{0.96}\text{Zr}_{0.9}\text{Y}_{0.1}\text{O}_{3-\delta} + \text{ZnO}$ (0-3wt%) sintered by PB method at 1500 °C for 5h. Compared with the lattice parameters of $\text{Ba}_{0.96}\text{Zr}_{0.9}\text{Y}_{0.1}\text{O}_{3-\delta} + \text{ZnO}$ (0-3wt%) sintered at 1500 °C for 5h without PB method, there was only a little difference which was considered as the composition of Ba changed. From this result, it could be expected that the decrease in electrical conductivity caused by adding ZnO at 2 wt% or more could be avoided. And powder bed method could prevent the BaO pellet sublimation and surface decomposition.

	Relative density	Relative density (PB)
ZnO 0wt%	74.40%	72.50%
ZnO 1wt%	86.70%	86.00%
ZnO 2wt%	95.60%	96.00%
ZnO 3wt%	99.60%	99.10%

Table 4 The relative density of $Ba_{0.96}Zr_{0.9}Y_{0.1}O_{3-\delta}$ + ZnO (0-3wt%) sintered at 1500 °C for 5h with and without PB method.

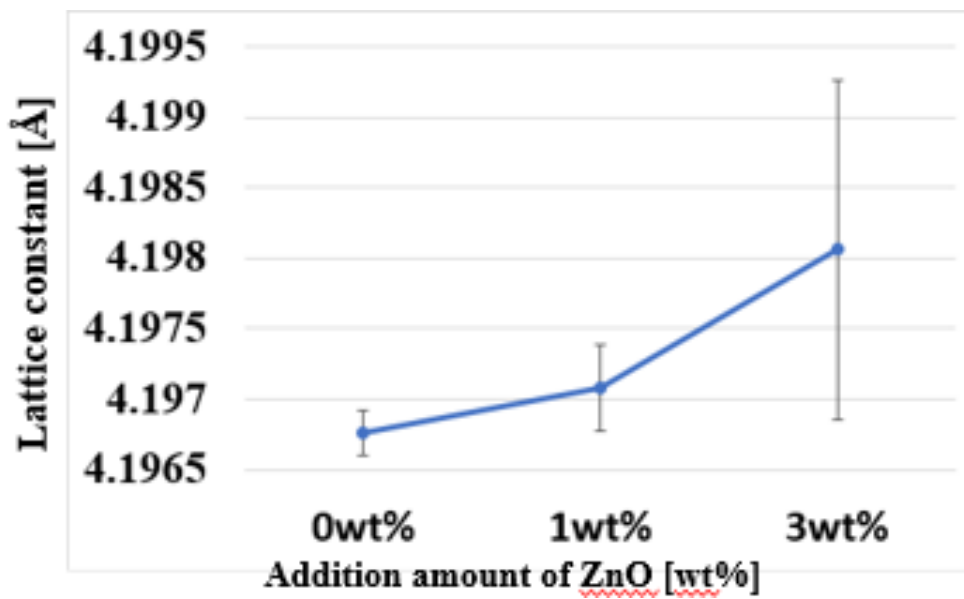


Fig.4.11 The lattice constant of $Ba_{0.96}Zr_{0.9}Y_{0.1}O_{3-\delta}$ + ZnO (0-3wt%) sintered by PB method at 1500 °C for 5h.

4.3 Conclusion

In this part of work, we synthesized the $\text{Ba}_{1-x}\text{Zr}_{1-y}\text{Y}_y\text{O}_{3-\delta}$ ($x = 0.02, 0.04$) and ($y = 0.1, 0.2, 0.3$) samples successfully and researched about the experiment conditions with XRD measurement. It was confirmed that the $\text{Ba}_{0.96}\text{Zr}_{0.9}\text{Y}_{0.1}\text{O}_{3-\delta}$ was the best condition. Then we added the ZnO as the sintering aid to obtain the $\text{Ba}_{0.96}\text{Zr}_{0.9}\text{Y}_{0.1}\text{O}_{3-\delta} + \text{ZnO}$ (0-3wt%) samples sintered at 1500 °C for 5h. We took XRD, and AC impedance analysis measurements to research about the affection of ZnO added into the samples. From the result, we could see that ZnO was effective as a sintering aid. As a result, the relative density could reach 99.6% of $\text{Ba}_{0.96}\text{Zr}_{0.9}\text{Y}_{0.1}\text{O}_{3-\delta} + \text{ZnO}$ 3wt%. And the electrical conductivity of $\text{Ba}_{0.96}\text{Zr}_{0.9}\text{Y}_{0.1}\text{O}_{3-\delta} + \text{ZnO}$ 1wt% sample was the highest. It was considered that the reason was the perovskite structure was destroyed so that the grain boundary resistance was increased.

Then we tried to prevent BaO pellet sublimation and surface decomposition with powder bed method. XRD showed that ZnO was not confirmed as a peak after sintering, but XRF showed that a small amount of Zn remained. Therefore, it was thought that ZnO was amorphous or existed between lattices. From EDS result, it was found that Y precipitation on the pellet surface could be suppressed by the PB method. It is hoped that powder bed method could prevent the BaO pellet sublimation and surface decomposition in the future work.

Reference

- [1] H. Iwahara, Y. Asakura, K. Katahira, M. Tanaka, *Solid State Ionics* 168 (2004) 299.
- [2] T. Schober, H. Ringel, *Ionics* 10 (5–6) (2004) 391.
- [3] J.L. Luo, K.T. Chuang, A.R. Sanger, *Electrochim. Acta* 53 (10) (2008) 3701.
- [4] H. Iwahara, *Solid State Ionics* 77 (1995) 289.
- [5] T. Schober, *Solid State Ionics* 162–163 (2003) 277.
- [6] K. Katahira, Y. Kohchi, T. Shimura, H. Iwahara, *Solid State Ionics* 138 (2000) 91.
- [7] S.M. Haile, G. Staneff, K.H. Ryu, *J. Mater. Sci.* 36 (2001) 1149.
- [8] H.R. Kwang, S.M. Hayle, *Solid State Ionics* 125 (1999) 335.
- [9] H.G. Bohn, T. Schober, *J. Am. Ceram. Soc.* 83 (4) (2000) 768.
- [10] F.M.M. Snijkers, A. Buekenhoudt, J. Coymans, J.J. Luyten, *Scripta. Mater.* 50(2004) 655.
- [11] K. Nomura, H. Kageyama, *Solid State Ionics* 178 (2007) 661.
- [12] F. Iguchi, T. Yamada, N. Sata, T. Tsurui, H. Yugami, *Solid State Ionics* 177 (26–32) (2006) 2381.
- [13] A. Magrez, T. Schober, *Ionics* 11 (2005) 171.
- [14] A. Magrez, T. Schober, *Solid State Ionics* 175 (2004) 585.
- [15] A.M. Azad, S. Subramaniam, T.W. Dung, *J. Alloy. Compd.* 334 (2002) 118.
- [16] R.B. Cervera, Y. Oyama, S. Yamaguchi, *Solid State Ionics* 178 (2007) 569.
- [17] U.A. Tamburini, M.T. Buscaglia, M. Viviani, M. Bassoli, C. Bottino, V. Buscaglia, P.Nanni, Z.A. Munir, *J. Eur. Ceram. Soc.* 26 (2006) 2313.
- [18] G. Pfaff, *Mater. Lett.* 24 (1995) 393.
- [19] G. Taglieri, M. Tersigni, P.L. Villa, C. Mondelli, *Inorg. Mater.* 1 (1999) 103.
- [20] A.E. Reheim, M.K. El-Nimr, A. Tawfik, D. El-Kony, *Proc. Indian Nati. Sci. Acad., PartA: Phys. Sci.* 53 (2) (1987) 217.
- [21] M. Pollet, S. Marinel, *Mater. Sci. Eng. A* 362 (2003) 167.
- [22] F. Roulland, R. Terras, G. Allainmat, M. Pollet, S. Marinel, *J. Eur. Ceram. Soc.* 24(2004) 1019.
- [23] S.W. Tao, J.T.S. Irvine, *Adv. Mater.* 18 (2006) 1581.

[24] S.W. Tao, J.T.S. Irvine, *J. Solid State Chem.* 180 (2007) 3

[25] Y. Liu, M. Tade and Z. Shao, *Royal Society of Chemistry* (2013) pp.26-55.

Chapter 5. Summary

In the first part of work, we synthesis the $Ce_{1-x}La_xO_{2-\delta}$ ($x = 0.1 \sim 0.5$) samples with the co-precipitation method. We research about the starting conditions about the ratio between metal ion and precipitating reagent are 1:20, 1:15 and 1:5, respectively. We can see with three kinds of conditions, the XRD has no difference about the final products. But the relative densities are different with the amount of the starting materials. Then we use SEM measurement to check about the surface of the powders sintered at 600 °C for 1h and pellets sintered at 1500 °C for 5 h, respectively. We can conclude that with the powders sintered at 600 °C for 1h, for the 1:15 powder sample, the particle diameter and the topographical features are both uniform than the other two. To the pellets sintered at 1500 °C for 5 h, the 1:15 pellets, the particle size is uniform and there is no obviously pores on the surface. We can conclude that the particle size of the calcined particles is related with the starting material concentration and the best conditions are 1:15 about the ratio of metal ion and precipitating reagent.

Then we synthesis the $Ce_{1-x}La_xO_{2-\delta}$ ($x = 0.1 - 0.5$) samples under this condition. We measured the XRD. We can see that all the samples appeared a single phase in the XRD patterns. But when we calculated the lattice parameters of each sample, the experimental data is not fit with the theoretical one. So we suspect that there is a structure change at $x=0.3$ of $Ce_{1-x}La_xO_{2-\delta}$ ($x = 0.1 \sim 0.5$) samples. In the second part of work, the changes in local structures of $Ce_{1-x}Ln_xO_{2-\delta}$ with Ln (La, Gd) doping were investigated. XAFS was successfully used to clarify the coordination environments around Ce and the dopant La and Gd. For LDC, La coordination was maintained at 7, and Ce coordination decreased from 8 to 6. It was speculated that because a superstructure would be formed which was more like a pyrochlore structure in LDC at $x>0.3$, the oxygen vacancies could be attracted by the larger La^{3+} . For GDC, the coordination numbers for Gd and Ce decreased from 8 to 6. In the GDC, oxygen vacancies had no preference for Ce or Gd coordination.

We also combined XRD results and EXAFS results together. These results explained the changes in the lattice parameters for both LDC and GDC. The local structure change model was designed

and the electric conductivity change at each stage of Ln (La, Gd) doping was explained. In future studies, these results can be applied to other materials.

In the third part of work, we synthesis the $Ba_{1-x}Zr_{1-y}Y_yO_{3-\delta}$ ($x = 0.02, 0.04$) and ($y = 0.1, 0.2, 0.3$) samples successfully and researched about the experiment conditions with XRD measurement. It is confirmed that the $Ba_{0.96}Zr_{0.9}Y_{0.1}O_{3-\delta}$ is the best condition. Then we add the ZnO as the sintering aid to obtain the $Ba_{0.96}Zr_{0.9}Y_{0.1}O_{3-\delta} + ZnO$ (0-3wt%) samples sintered at 1500 °C for 5h. We took XRD, and AC impedance analysis measurements to research about the affection of ZnO added into the samples. From the result, we could see that ZnO was effective as a sintering aid. As a result, the relative density could reach 99.6% of $Ba_{0.96}Zr_{0.9}Y_{0.1}O_{3-\delta} + ZnO$ 3wt%. And the electrical conductivity of $Ba_{0.96}Zr_{0.9}Y_{0.1}O_{3-\delta} + ZnO$ 1wt% sample was the highest. It was considered that the reason was the perovskite structure was destroyed so that the grain boundary resistance was increased.

Then we tried to prevent BaO pellet sublimation and surface decomposition with powder bed method. XRD showed that ZnO was not confirmed as a peak after sintering, but XRF showed that a small amount of Zn remained. Therefore, it was thought that ZnO was amorphous or existed between lattices. From EDS result, it was found that Y precipitation on the pellet surface could be suppressed by the PB method. It is hoped that powder bed method could prevent the BaO pellet sublimation and surface decomposition in the future work.

Acknowledgement

First of all, I would like to take this opportunity to express my deepest gratitude and also show my great honest to my advisor in Japan, Prof. Toshihiro Moriga., a responsible, respectable and patient professor, who has provided me with valuable guidance in every stage of writing this thesis. It's my great honor to have such a professor in my PHD process. During the three years in the Tokushima University, Prof. Moriga has given me numerous supports from financial to experiment, and encouragement both in research and daily life, making the adaptation of life and research in Japan much more quickly and the stay in Japan much more pleasant. He always takes care of his students like his own children. What I have learned from Prof. Moriga is not only much knowledge in studies but also the responsible attitude towards other people. Without his enlightening instructions, impressive kindness and patience, I could not complete my thesis. I'm sure I will take his spirit in my future work. Thank you with all my heart and in all my life.

I should also express my great thanks to Prof. Kei-ichiro Murai, he has provided me countless support in the study and daily life. Especially, I still can remember the experiments in Spring-8 photon factory. Thanks to you, my life in Japan is full of joyful and substantial.

With the same important position, I will give my deepest gratitude to my parents and my relatives. Their great supports of mental and substantial are on my back to encourage me going through the Doctor Process. I couldn't use any appropriate word to describe it but I will spend all my left time to feed them back.

Next, I want to thank to the International Center officers, Mr Kim Chenghai and the others. They have solved many problems for me including financials, dormitory and so on. With their great help, I could focus on my study without caring about the other complex problems in the life. I also want to thank to my Japanese teachers, they taught me Japanese which I could talk with the others easily with understanding their cultures. It makes my life easier in Japan. Thank you with a 90 degree bow.

My sincere thanks also go to my team members, Mr. Minakada, Mr. Ryonoske, Mr. Otani, Mr.

kengo and Mr. Kei-ichiro. They have support me to complete the whole thesis with a great effort. And I thank to all C-1 lab members of I have met in all my three years. They help me a lot in the experiment and more in life which make me not feel lonely. Thank you with all my heart.

Then, I want to thank to all of my friends I have made in my three years staying in Japan. The friendship supports me to continue the study in Doctor procedure and it will last forever even we are in everywhere of the world.

Finally, I would like to appreciate all the people who have given me support or encouragement directly or indirectly. In all my three years, I have been through a lot. But I still not lose the courage and confidence to meet any challenge in the future. That all comes from the above people`s help. Thank you with all my heart, and thank you with all my life.

Publications

Local structure changes of $Ce_{1-x}Ln_xO_{2-\delta}$ ($Ln = La, Gd$) solid electrolytes

Xue Liu¹, Runosuke Minato¹, Yasumasa Otani¹, Kengo Hadai¹, Kei-ichiro Murai¹, Masashi Mori²,
Atsushi Yoshinari³, Munehiko Miyano³, Atsushi Sakaki³ and Toshihiro Moriga^{1*}
Solid State Ionics, 347, (2020), 115213

Other papers:

1. Characterizations of $Ba_{1-x}Zr_{0.9}Y_{0.1}O_{3-\delta}$ ($x=0, 0.04$) and improvement of sinterability by addition of ZnO

Yasumasa Otani, Kengo Hatai, Hiroki Kishigami, Liu Xue, Kei-ichiro Murai, Toshihiro Moriga and Masashi Mori, PACRIM13(The 13th Pacific Rim Conference of Ceramic Societies), Okinawa, Oct, 2019.

2. Influence of molecular weight on scaling exponents and critical concentrations of one soluble 6FDA-TFDB polyimide in solution,

Ensong Zhang, Hongxiang Chen, Xuemin Dai, Xue Liu, Wenke Yang, Wei Liu, Zhixin Dong, Xuepeng Qiu, Xiangling Ji, J Polym Res (2017) 24:47.

3. Degradation Behavior of 6FDA-TFDB Poly(amic acid) Solution via Rheological Method,

En-song Zhang, Xue-min Dai, Xue Liu, Wen-ke Yang, Wei Liu, Zhi-xin Dong, Xue-peng Qiu, Xiang-ling Ji, ACTA POLYMERICA SINICA, Sep., 2017, No. 9.